論文 / 著書情報
Article / Book Information

題目(和文)	
Title(English)	Reaching for Earth ’ s core: combining the insights from single crystal paleomagnetism and high pressure experiments
著者(和文)	加藤千恵
Author(English)	Chie Kato
出典(和文)	学位:博士(理学), 学位授与機関:東京工業大学, 報告番号:甲第10730号, 授与年月日:2018年3月26日, 学位の種別:課程博士, 審査員:井田 茂,綱川 秀夫,上野 雄一郎,横山 哲也,太田 健二,廣瀬 敬,KIRSCHVINK JOSEPH LY
Citation(English)	Degree:Doctor (Science), Conferring organization: Tokyo Institute of Technology, Report number:甲第10730号, Conferred date:2018/3/26, Degree Type:Course doctor, Examiner:,,,,,,
学位種別(和文)	博士論文
Type(English)	Doctoral Thesis

Doctoral Thesis

Reaching for Earth's core: combining the insights from single crystal paleomagnetism and high pressure experiments

Chie Kato

Department of Earth and Planetary Sciences,

Tokyo Institute of Technology

February 2018

Abstract

Because the chemical composition of the Earth's core and the structure of the core-mantle boundary (CMB) have a large influence on Earth's thermal evolution, it is important to constrain the history of the core from petrographic constraints placed by the high-pressure and high-temperature properties of materials near and below the CMB, and the behavior of the geomagnetic field. In "Reaching for the Core", I have used approaches from both fields to better constrain our knowledge of the history and structure of the Deep Earth.

I made contributions for the stable structure and compression behavior of iron hydride and for understanding the melting phase relations of lowermost mantle materials. Despite its importance as a candidate of the core material, the high pressure phase relations of iron hydride is poorly understood. I investigated the phase relation of stoichiometric FeH and compression behavior of nonmagnetic face-centered cubic FeH up to 140 GPa by high -pressure and -temperature experiments combined with *ab initio* calculations. The results provide fundamental information for exploring the chemical composition of the core, which may largely affect the estimation of the thermal evolution of the core. Similarly, I studied the melting phase relations of the FeO-SiO_2 system. Based on the results, I argued that melting of the banded iron formations subducted to the lowermost mantle may have enhanced the heterogeneity of the CMB. Heterogeneous distribution of FeO at the CMB could give rise to spatial variations in the CMB heat flow, which in turn influence the stability of the geodynamo.

Constraining the long-term trend of the geomagnetic field is one key for understanding the thermal evolution of Earth's core, because convection in the liquid outer core generates the geomagnetic dynamo. I conducted paleointensity experiments using single silicate crystals separated from the middle Cretaceous Iritono granite and demonstrated that an assemblage of plagioclase crystals could reproduce paleointensity consistent with the host whole-rock sample. This new method has the potential to provide better constraints on the behavior of the geomagnetic field through geological time by averaging out the short-term fluctuations of the geomagnetic field and avoiding the influence of undesirable magnetic components in the measurements. In addition, the results suggest a high time-averaged dipole field strength during the Cretaceous normal superchron, and imply an anticorrelation between magnetic polarity reversal frequency and field intensity.

Thermal evolution models of the deep earth inferred from high pressure petrographic constrains need to be verified by constrains by geological data. Long-term trends of the geomagnetic field obtained by paleomagnetic studies need to be interpreted by an evolution model for the core/mantle system. These are connected to each other through numerical dynamo models. Finally, I reviewed the influencing factors on the long-term change of the geomagnetic field from the dynamics of the core and mantle. The contributions of the present three studies to the investigations of inner core crystallization and CMB heat flow pattern are discussed.

Contents

Chapter 1.

General introduction

§1 Overview of the present Earth's core

Earth's core is a body of iron-nickel alloy which accounts for half of the diameter and 16 % of the total volume of the Earth. Geochemical research including studies on iron meteorites suggests that the major constituent of the core is iron, and about 5-10 % nickel (Birch, 1952). The core is composed of a liquid outer core between 2890 and 5150 km in depth from the surface, and a solid inner core below 5150 km.

Density and seismic wave velocity profiles of the Earth's interior are measured through seismic observations. Dziewonski and Anderson (1981) synthesized a suite of one-dimensional averaged profiles commonly used in the community into the Preliminary Reference Earth Model (PREM), which is now used as the basic reference model in the Deep Earth community. According to this work, the density of the core is slightly lower than that of pure iron obtained by high-pressure experiments, suggesting the presence of alloying by light element(s); this is known as the core density deficit problem. Considering the cosmochemical abundance and compatibility to iron, major candidates of the alloying element(s) are hydrogen, carbon, oxygen, silicon and sulfur (Poirier, 1994). The density deficit is larger in the outer core than the inner core, which implies that the alloying light element(s) is less compatible in solid rather than liquid iron. The light element composition of the core has been investigated using geochemical constraints, seismic velocities, densities, and conditions of the core-mantle segregation (Hirose et al., 2013 for a review). However, a general consensus on the composition of the core has not yet been reached.

The temperature profile within the core is a matter of debate. At the inner core boundary (ICB), the liquid and solid alloys coexist. Thus, the pressure dependence of the melting temperature of core materials constrains the temperature (Boehler, 1993). In the outer core this is extrapolated along the adiabat from the ICB to the core-mantle boundary (CMB), with estimated temperatures at the CMB between 3,300 and 4,300 K (Lay et al., 2008).

The presence of the geomagnetic field provides another piece of evidence of the liquid metallic outer core, as well as whether or not it is actively convecting, rather than being thermally stratified. Observations of the shape, strength and time evolution of the geomagnetic field can provide strong constraints on its flow and stratification. Some important features of the geomagnetic field such as the columnar flows along the pole generating the dipolar geomagnetic field have been revealed by geodynamo simulations (Glatzmaier and Roberts, 1995; Kageyama et al., 1995). The existence of a stratified layer near the core/mantle boundary has been predicted based on both geomagnetic features (Gubbins, 2007; Buffett, 2014) and seismic observations (e. g. Helffrich and Kaneshima, 2010; 2013).

The outer core contacts the mantle at the core-mantle boundary (CMB), which is the greatest chemical and thermal boundary of the Earth. The mantle has controlled the state and evolution of the core since it formed. In terms of the geomagnetic field, the heat flow across the CMB is thought to influence the heterogeneity, strength, and reversal frequency (e.g. Larson and Olson, 1991; Glatzmaier et al., 1991; Courtillot and Olson, 2007; Takahashi et al., 2008; Olson, 2016). Therefore, the thermal boundary layer immediately

above the CMB (called D") could play a critical role on the geomagnetic field. Distinct features of this D" layer, revealed by seismic tomography are chemical/thermal heterogeneities termed 'Ultra-Low Velocity Zones'. These are patches 1 to 10 kilometers thick that are characterized by a 10 to 20 % decrease in compressional wave velocity, and a 10 to 30 % decrease in shear wave speed compared to PREM (Garnero et al., 1998). It is suspected that material which differentiated early (Boyet and Carlson, 2005) and/or that which was subducted has accumulated in the D" region, giving rise to the chemical/thermal heterogeneity that possibly affects the geomagnetic behavior.

§2 Exploring the history of Earth's core

Many paleomagnetic and heat transport calculations have focused on the thermal evolution of the core. The paleomagnetic record suggests that the geomagnetic field has existed for at least the past 3.5 Ga (Tarduno et al., 2010), as does molecular clock evidence for the antiquity of the magnetotactic bacteria (Lin et al., 2017), which are also dependent on the geomagnetic field. The existence of a dynamo means that the liquid core is convecting. To sustain thermal convection requires that the adiabatic heat flow exceeds the total heat flow. The adiabatic heat flow Qs(r) can be expressed as

$$Q_s(r) = -4\pi r^2 k \left(\frac{\partial T}{\partial r}\right)_s \quad (1)$$

where k is the thermal conductivity, r is the depth and T is temperature. This shows that the thermal conductivity is a crucial parameter for thermal evolution of the core.

Estimates of thermal conductivity have been made both by means of high-pressure experiments and ab initio calculations, but there are large discrepancies between the different methods (e.g. Ohta et al., 2016; Konôpková et al., 2016). Different values of thermal conductivity result in different past temperature estimates; i.e. high and low conductivities mean fast and slow cooling of the core, respectively, which make for large differences in the estimates for the initial core temperature. In turn, this has a profound effect on estimates for the onset of inner core crystallization. Depending on the thermal conductivity and amount of radioactive ^{40}K, estimates for the age of the inner core vary from 0.6 Ga (Labrosse, 2015) to 4.3 Ga (Stacy and Loper, 1983). Also, the light element composition of the core can affect the thermal conductivity and thus the estimated inner core age (e.g. Gomi and Hirose, 2015).

Paleointensity measurements are one of the best methods to constrain the age of the inner core from geologic evidence. Dynamo simulations and energy calculations indicate that Earth's virtual dipole moment (VDM) should have increased substantially upon inner core nucleation due to the energy released by compositional convection (e.g. Aubert et al., 2009; Labrosse 2015). Based on the compiled database of published paleointensity data, Biggin et al. (2015) argued that a substantial increase in strength and variability of the geomagnetic paleointensity occurred at ~1.3 Ga, which could mark the birth of the inner core. However, it might be premature to discuss the inner core age based on the long-term trend of the geomagnetic field intensity because reliable Precambrian paleointensity data are too sparse. Additionally, an

increase of the VDM is not uniquely associated with the inner core. For example, heterogeneity of the core-to-mantle heat flux could also enhance the field strength (Takahashi et al., 2008). Precipitation of light elements from the liquid core could cause compositional convection, promoting dynamo action prior to the inner core nucleation (O'Rourke and Stevenson, 2017; Hirose et al., 2017).

Another great open question is the start of the geodynamo itself. Some paleointensity measurements on single zircon crystals from the Jack Hills conglomerate of Western Australia exhibit field strengths that correspond to 1.0 to 0.12 times of the recent equatorial value in the Hadean to Paleoarchean era (Tarduno et al., 2015). However, a separate study argues that all of the magnetization of the Jack Hills conglomerates, including the zircons, were reset long after deposition (Weiss et al., 2015). Similarly, the isotopic composition of nitrogen in lunar soils suggest that it has a terrestrial origin, which would require a null or very weak geomagnetic field before about 3.9 Ga to allow nitrogen to escape from the Earth's atmosphere (Ozima et al., 2005).

To explore the evolution of the core, we need to combine direct information provided by paleomagnetic measurements with results from realistic geophysical models of mantle influence that are based on parameters obtained by high pressure experiments and calculations. At present, the low number of reliable paleomagnetic studies from the Precambrian era limits our understanding of the long-term behavior of the geomagnetic field. On the other hand, modeling of the evolution of the Earth's deep interior involves

large uncertainties because some fundamental parameters such as the chemical composition of the core and phase relations of the constituent materials are not determined.

In Chapters 2 and 3, I examined properties of candidate materials of the D" region and the core by means of high pressure experiments using the laser-heated diamond anvil cell technique and in-situ X-ray diffraction measurements. Chapter 2 reports the stable structure and compression behavior of iron hydride (FeH_x), predicted by computational calculations of the magnetic state under high pressure. In Chapter 3, I focus on the role of subducted banded iron formations (BIFs) and show that partial melting of the BIFs could provide FeO-rich patches in the lowermost mantle which could contribute to the genesis of the ULVZs.

Chapter 4 is aimed at investigating the long-term trend of the intensity of the geomagnetic field, as it is related to evolution of the inner core and thermal control of the core/mantle boundary. Recent studies have shown that single crystal silicate minerals often contain inclusions of nanophase ferromagnetic minerals that might be ideal archives for paleointensity study, avoiding the complications of larger magnetic grains often present in plutonic rocks. These mineral grains are easily separated from the host rock, and the extensive geological record of plutonic activity on relatively stable cratons argues that feasible samples to study for this purpose might extend back to early Archean time. However, suitable single-crystal techniques must be developed and tested first on well-known control samples, which has rarely been done to date. To evaluate the paleointensity methods on single crystals,

we choose to study the Iritono granite from northeast Japan because its rock-magnetic properties and paleointensity are already well constrained (Wakabayashi et al., 2006; Tsunakawa et al., 2009). I separated zircon, quartz and plagioclase crystals from sister samples to those used by Tsunakawa et al. (2009), and conducted the necessary rock-magnetic experiments. Paleointensity measurements were then carried out for the plagioclase grains, which the rock-magnetic results indicated were the most suitable samples. The results show that an assembly of single plagioclase crystals separated from a granitic rock have the ability to possess the same paleointensity information as the host whole-rock. Paleointensity measurements on plagioclase separated from granitic rocks could be a prospective tool to increase the number of paleointensity results from various ages.

Advanced investigation of the history of deep Earth will be facilitated by combining insights from both paleomagnetic and high-pressure experiments. In Chapter 5 we discuss the effectiveness of the paleointensity method shown in Chapter 4, and summarize the major factors influencing the long-term trend of geomagnetic field intensity which are related to the high pressure experimental studies reported in Chapters 2 and 3.

References

Aubert, J., Labrosse, S., Poitou, C. (2009). Modelling the palaeo-evolution of the geodynamo, Geophysical Journal International, 179, 1414-1428.

Biggin, A. J., Piispa, E. J., Pesonen, L. J., Holme, R., Paterson, G. A., Veikkolainen, T., Tauxe, L. (2015). Palaeomagnetic field intensity variations suggest Mesoproterozoic inner-core nucleation. Nature, 526(7572), 245-248.

Birch, F. (1952). Elasticity and constitution of the Earth's interior. J Geophys Res 57(2): 227–286.

Boehler, R. (1993). Temperatures in the Earth's core from melting-point measurements of iron at high static pressures. Nature, 363(6429), 534-536.

Boyet, M., Carlson, R. W. (2005). 142 Nd evidence for early (> 4.53 Ga) global differentiation of the silicate Earth. Science, 309(5734), 576-581.

Buffett, B. (2014). Geomagnetic fluctuations reveal stable stratification at the top of the Earth's core. Nature, 507(7493), 484-487.

Courtillot, V., Olson, P. (2007). Mantle plumes link magnetic superchrons to Phanerozoic mass depletion events. Earth and Planetary Science Letters, 260(3), 495-504.

Dziewonski, A. M., Anderson, D. L. (1981). Preliminary reference Earth model. Physics of the earth and planetary interiors, 25(4), 297-356.

Garnero, E. J., Revenaugh, J., Williams,Q., Lay, T. Kellog, L. H. in *The Core-Mantle Boundary Region* (eds Gurnis, M.,Wysession, M. E., Knittle, E. Buffet, B. A.) 319–334 (American Geophysical Union, Washington DC, 1998).

Glatzmaier, G.A., Roberts, P.H. (1995). A three-dimensional self-consistent

computer simulation of a geomagnetic field reversal. Nature, 377, 203-209.

Glatzmaier, G. A., Coe, R. S., Hongre, L., Roberts, P. H. (1999). The role of the Earth's mantle in controlling the frequency of geomagnetic reversals. Nature, 401(6756), 885-890.

Gomi, H., Hirose, K. (2015). Electrical resistivity and thermal conductivity of hcp Fe–Ni alloys under high pressure: Implications for thermal convection in the Earth's core. Physics of the Earth and Planetary Interiors, 247, 2-10.

Gubbins, D. (2007). Geomagnetic constraints on stratification at the top of Earth's core. Earth, planets and space, 59(7), 661-664.

Helffrich, G., Kaneshima, S. (2010). Outer-core compositional stratification from observed core wave speed profiles. Nature, 468(7325), 807-810.

Helffrich, G., Kaneshima, S. (2013). Causes and consequences of outer core stratification. Physics of the Earth and Planetary Interiors, 223, 2-7.

Hirose, K., Labrosse, S., Hernlund, J. (2013). Composition and state of the core. Annual Review of Earth and Planetary Sciences, 41, 657-691.

Hirose, K., Morard, G., Sinmyo, R., Umemoto, K., Hernlund, J., Helffrich, G., Labrosse, S. (2017). Crystallization of silicon dioxide and compositional evolution of the Earth's core. Nature, 543(7643), 99-102.

Kageyama, A., Sato, T. and the Complexity Simulation Group (1995). Computer simulation of a magnetohydrodynamic dynamo II. Phys. Plasmas., 2, 1421-1431.

Konôpková, Z., McWilliams, R. S., Gómez-Pérez, N., Goncharov, A. F. (2016). Direct measurement of thermal conductivity in solid iron at planetary core conditions. Nature, 534(7605), 99-101.

Labrosse, S. (2015). Thermal evolution of the core with a high 302 thermal conductivity, Phys. Earth Planet. Inter., 247, 36–55.

Larson, R. L., Olson, P. (1991). Mantle plumes control magnetic reversal frequency. Earth and Planetary Science Letters, 107(3-4), 437-447.

Lay, T., Hernlund, J., Buffett, B. A. (2008). Core–mantle boundary heat flow. Nature Geoscience, 1(1), 25-32.

Lin, W., Paterson, G. A., Zhu, Q., Wang, Y., Kopylova, E., Li, Y., Knight, R., Bazylinski, D. A., Zhu, R., Kirschvink, J. L., Pan, Y. (2017). Origin of microbial biomineralization and magnetotaxis during the Archean. Proceedings of the National Academy of Sciences, 201614654.

Ohta, K., Kuwayama, Y., Hirose, K., Shimizu, K., Ohishi, Y. (2016). Experimental determination of the electrical resistivity of iron at Earth's core conditions. Nature, 534(7605), 95-98.

Olson, P. (2016). Mantle control of the geodynamo: Consequences of top - down regulation. Geochemistry, Geophysics, Geosystems, 17(5), 1935-1956.

O'Rourke, J. G., Stevenson, D. J. (2016). Powering Earth's dynamo with magnesium precipitation from the core. Nature, 529(7586), 387-389.

Ozima, M., Seki, K., Terada, N., Miura, Y. N., Podosek, F. A., Shinagawa, H. (2005). Terrestrial nitrogen and noble gases in lunar soils. Nature, 436(7051), 655-659.

Poirier, J. P. (1994). Light elements in the Earth's outer core: a critical review. Physics of the earth and planetary interiors, 85(3-4), 319-337.

Stacey, F. D., and D. E. Loper (1983). The thermal boundary layer interpretation of D" and its role as a plume source, Phys. Earth Planet. Inter., 33(1), 45–55.

Takahashi, F., Tsunakawa, H., Matsushima, M., Mochizuki, N., Honkura, Y. (2008). Effects of thermally heterogeneous structure in the lowermost mantle on the geomagnetic field strength. Earth and Planetary Science Letters, 272(3), 738-746.

Tarduno, J. A., Cottrell, R. D., Watkeys, M. K., Hofmann, A., Doubrovine, P. V., Mamajek, E. E., Liu, D., Sibeck, D. G., Neukirch, L. P., Usui, Y. (2010). Geodynamo, solar wind, and magnetopause 3.4 to 3.45 billion years ago. Science, 327(5970), 1238-1240.

Tarduno, J. A., Cottrell, R. D., Davis, W. J., Nimmo, F., Bono, R. K. (2015). A Hadean to Paleoarchean geodynamo recorded by single zircon crystals. Science, 349(6247), 521-524.

Tsunakawa, H., Wakabayashi, K. I., Mochizuki, N., Yamamoto, Y., Ishizaka, K., Hirata, T., Takahashi, F., Seita, K. (2009). Paleointensity study of the middle Cretaceous Iritono granite in northeast Japan: Implication for high field intensity of the Cretaceous normal superchron. Physics of the Earth and Planetary Interiors 176(3), 235-242.

Wakabayashi, K. I., Tsunakawa, H., Mochizuki, N., Yamamoto, Y., Takigami, Y. (2006). Paleomagnetism of the middle Cretaceous Iritono granite in the Abukuma region, northeast Japan. Tectonophysics 421(1), 161-171.

Weiss, B. P., Maloof, A. C., Tailby, N., Ramezani, J., Fu, R. R., Hanus, V., Trail, D., Watson, E. B., Harrison, T. M., Bowring, S. A., Kirschvink, J. L., Swanson-Hysell, N. L., Coe, R. S. (2015). Pervasive remagnetization of detrital zircon host rocks in the Jack Hills, Western Australia and implications for records of the early geodynamo. Earth and Planetary Science Letters, 430, 115-128.

Chapter 2

Structural transition and compression behavior of FeH at high pressure

Abstract

Face centered cubic (fcc), double-hexagonal close packed (dhcp) and hexagonal close packed (hcp) structures have been reported for the stable crystal structure of iron hydride, FeH_x ($x \leq 1$). However, the pressure-temperature phase relations of these polymorphs are poorly understood at pressures above 20 GPa. We studied the stable crystal structure and compression of FeH_x ($x \sim 1$) up to 137 GPa by high-pressure and –temperature experiments using laser-heated diamond-anvil cell techniques and synchrotron X-ray diffraction measurements. We found that the fcc structure was the most stable phase at pressures higher than 55 GPa. We also studied the magnetic moments of FeH polymorphs and compression behavior of fcc FeH by *ab initio* calculations. The volume and compressibility was consistent between experiments and calculations, and showed a discontinuous change at ~70 GPa, which may be due to a magnetic transition of fcc FeH_x from ferromagnetic to nonmagnetic state. Based on these results, we propose a *P-T* phase diagram of stoichiometric FeH in which fcc has a wide stability range at high pressure and temperature, while the dhcp structure, which has been thought to be stable at higher pressures, is stable only at pressures below around 50 GPa.

§1. Introduction

Iron hydride, FeH_x, is formed at hydrogen pressures higher than 3.5 GPa (e. g. Badding et al., 1991). The phase relationships and compression behaviors of iron hydrides are important information for studies of the Earth's metallic core, since hydrogen is a potential candidate of the alloying light element needed to account for the density deficit of the Earth's core relative to pure iron (Murphy, 2016 for a review). In the context of hydrogen-rich metallic alloys whose properties should be analogous to metallic hydrogen and in which high *Tc* superconductivity is frequently found, predictions and syntheses of iron hydride with high H stoichiometry has been the subject of recent interest in condensed matter physics and chemistry (Bazhanova, et al., 2012; Pépin et al., 2014; Li et al., 2017; Pépin et al., 2017). They are also of great interest for planetary sciences.

The *P-T* phase diagram of FeH_x has been studied experimentally up to 20 GPa by the multi-anvil apparatus (Sakamaki et al., 2009; Saitoh et al., 2017). In analogy with pure iron, the face centered cubic (fcc) structure was found to be stable at relatively high temperature. At relatively low temperature and high pressure, double-hexagonal close packed (dhcp) structure was formed instead of hexagonal close packed (hcp) structure for pure iron. By extrapolating the melting curve and dhcp/fcc phase boundary, the stability field of fcc disappears above 60 GPa and 2000 K. Dhcp FeH_x have been reported to be formed at up to ~100 GPa in nickel bearing samples (Ni5wt% or Ni10wt%, x=0.7~0.9; Terasaki et al., 2012) and synthesized by iron-water or iron-hydrous mineral reactions at up to 84 GPa (Ohtani et al.,

2005; Saxena et al., 2004). However, the stable phase of FeH_x at Earth's core pressures have not been investigated experimentally. Narygina et al., 2011 studied the formation and magnetization of fcc FeH_x based on Mössbauer spectroscopy and X-ray diffraction. They reported that fcc FeH_x was formed by heating a mixture of Fe and C_nH_{2n+2} paraffin above 55 GPa and 1650 K. At 26 GPa, fcc and dhcp FeH_x coexisted, although the hydrogen content of the two phases might differ. Dhcp FeH_x showed ferromagnetism while fcc FeH_x was non-magnetic or anti-ferromagnetic.

On the other hand, free-energy calculations suggest that FeH undergoes a structural transition from dhcp to hcp at 37 GPa, and hcp to fcc at 83 GPa at room temperature (Isaev et al., 2007). Isaev et al., 2007 mentioned that a ferromagnetic-paramagnetic transition takes place at ~60 GPa in fcc FeH which leads to change in the compressibility and stabilization of the fcc structure. However, this phase transition has not been observed experimentally. Also, a *P-V* curve for fcc FeH has not been reported over 60 GPa.

In this study, we investigated the stable structure of FeH_x at >50 GPa by experiments and studied the compression behavior of fcc FeH by both experiments and ab initio calculations.

§2. Methods

§2-1. Experimental Method

We used the laser-heated diamond-anvil cell (LHDAC) technique to achieve high-pressure and –temperatures for this study. In-situ X-ray

diffraction measurements were performed at BL10XU, SPring-8. We adopted two different methods for hydrogen sealing in LHDAC and synthesizing iron hydride. In runs1-3, pure iron foil (99.99% purity) and paraffin (C_nH_{2n+2}, n>5) pressure medium with ruby or KCl pressure markers were loaded into LHDAC, following the method by Narygina et al. (2011). In runs 4-8, hydrogen was introduced into LHDAC by cooling and liquidation of H_2 gas at ~20 K by a helium refrigerator (Chi et al., 2011; Ohta et al., 2015; Tagawa et al., 2016). Sample pressures were determined from spectrum of ruby fluorescence (Dorogokupets and Oganov, 2007) for run 1, lattice volume of KCl (Dewaele et al., 2012) for runs 2 and 3, and from lattice volume of NaCl (Ueda et al., 2008) for runs 4-8. To correct pressures of runs using different pressure scales, simultaneous lattice volume measurements of KCl and NaCl were performed.

§2-2. Computational method

Our *ab initio* calculations used the Perdew-Burke-Ernzerhof (PBE) form (Perdew et al., 1996) of generalized-gradient approximation (GGA) for the exchange and correlation (XC) functions. Vanderbilt's type pseudopotentials were used (Vanderbilt, 1990). The fcc unit cell contained 1 FeH. The cutoff radii for Fe and H were 0.956 and 0.265 Å, respectively. The plane-wave basis set with a cutoff energy of 40 Ry was used. The **k**-point mesh was 12×12×12. The smearing technique (Methfessel and Paxton, 1989) was used for integration up to the Fermi surface with the smearing parameter of 0.01 Ry. We used the quasi-harmonic approximation to take phonon effects

into account (Wallace, 1972). Dynamical matrices were computed at the 4×4×4 **q**-point mesh using the density-functional-perturbation theory (Giannozzi et al., 1991; Baroni et al., 2001). Vibrational densities of states were obtained by interpolation of phonon frequencies on the 24×24×24 **q**-point mesh. For magnetization, we considered ferromagnetic (FM), antiferromagnetic (AFM), and nonmagnetic (NM) states. For the AFM state, we considered two spin configurations. The one was assumed to be the same as in AFM-FeO; iron atoms on one (111) plane have the same spin, and opposite spins occur on adjacent planes. In the other configuration iron atoms on one (100) plane have the same spin, and opposite spins occur on adjacent planes. The former AFM state has lower enthalpy than the latter. Hence we took only the former for the AFM state. All calculations were performed using the Quantum-ESPRESSO package (Giannozzi et al., 2009).

§3. Results

§3-1. Experimental results

We performed a total of eight runs of LHDAC experiments for fcc FeH_x formation and compression/decompression, and obtained the lattice volumes at 15 to 137 GPa. In runs 1-3, iron sample and paraffin reacted and formed iron carbide soon after the beginning of laser heating at around 1600 K and 60 GPa. After 1-hour heating, iron carbide disappeared and fcc FeH_x and diamond formed as the previous study reported (Narygina et al., 2011) (Fig. 1). In samples in which liquid hydrogen was sealed in the DAC, FeH_x was synthesized in two different processes. In runs 4 and 5, pure hcp Fe was

observed before heating. During laser heating, hcp Fe diffraction peaks were weakened and a broad halo appeared indicating the presence of an amorphous state. Further heating ended up with the sudden emergence of fcc FeH_x (Fig. 2). In runs 6 and 7, hcp or dhcp FeH_x was already formed during H_2 sealing and compression before heating. Hcp and dhcp were weakened and replaced by fcc during laser heating (Fig. 3). In run 8, which was performed at relatively low pressure, weakening of dhcp FeH_x and growth of hcp FeH_x was observed. We note that this hcp FeH_x was unsaturated in hydrogen, in contrast to fcc as discussed later. In several runs, FeH_2 and FeH_3 (Pepin et al., 2014) was observed occasionally, but disappeared when heated at higher temperature. After synthesis of fcc FeH_x, the *P-V* data was obtained by compression/decompression.

In the simultaneous lattice volume measurements of NaCl and KCl, the pressure gap between two markers was 0.3 GPa at 52 GPa and 13.4 GPa at 133 GPa. We fitted the pressure gap to the following equation: PKCl-PNaCl=a*exp(PKCl/b), where a and b are constants, and corrected pressures from KCl by subtracting the right-side value at each pressure. Fitted value of the constants was a=0.058(17) and b=26.9(15).

Hydrogen concentration of FeH_x was estimated based on volume expansion at each pressure ($x=(V(\text{fcc } FeH_x)-V(\text{fcc Fe}))/V_H$). Here we adopt the EOS of fcc Fe at 298 K by Boehler et al. (1990). Note that spin transition in fcc Fe is expected to occur within the studied pressure range but hard to detect from the *P-V-T* data (Tsujino et al., 2013). Volume expansion per H atom, V_H, was calculated using the assumption of (Fukai, 1992). We employed

2.21 Å^3 for V_{H0} based on neutron diffraction measurements of FeD0.64 at 6.3 GPa, 988 K (Machida et al., 2014). For the present experimental results, x of the fcc FeH_x was calculated to be almost unity at the whole pressure range (Fig. 4). The mean value of x was 1.01(6). On the other hand, x calculated for hcp FeH_x in run 8 was 0.3.

Fig. 5 shows the volume of fcc FeH_x per Fe atom as a function of pressure. A discontinuous change of compressibility is found at ~65 GPa. We calculated parameters of third-order Birch-Murnaghan equation of states (EOS) of the fcc phase for <60 GPa and >70 GPa (Table1). The interval pressure range was excluded because of the anomalistic behavior of the lattice volume possibly due to non-equilibrium hydrogen distribution aftermath the reaction of iron and paraffin. The low-pressure EOS parameters are consistent to those reported by Narygina et al. (2011), who studied a similar pressure range. The bulk modulus K_0 and its pressure derivative K_0' of the high-pressure EOS was larger and smaller than those of the low-pressure EOS, respectively.

§3-2. Computational results (conducted by K. Umemoto)

In our static calculations, the FM state is obtained up to ~50 GPa and is always stable with respect to the NM state. The AFM state is energetically never stable with respect to both FM and NM states at all pressures investigated. Under compression, calculated magnetic moment (M) in the FM state decreases gradually from 2.2 μ_B/FeH at 13.5 Å^3/FeH, i.e., 0 GPa to 1.8 μ_B/Fe at ~11 Å^3/FeH, corresponding to ~50 GPa (Fig. 6). By further

compression, however, M in the FM state abruptly vanishes and the system becomes NM with an abrupt decrease of volume, being qualitatively consistent with Elsässer et al. (1998) and Isaev et al., (2007). For a comparison, we also calculated M in dhcp and hcp phases under compression as shown in Fig. 6. At larger volume region (i.e., lower pressure region), M in all three phases are very similar to each other; that in the fcc phase is marginally higher than those in other two phases. In the dhcp phase, the magnetization abruptly vanishes at ~10.3 Å^3/FeH which is slightly smaller than that where the magnetization vanishes in the fcc phase. In the hcp phase, on the other hand, magnetization behavior is rather different from in the other two phases. The FM state survives down to ~8.5 Å^3/FeH (~210 GPa) with a continuous decrease of M. These magnetization behaviors are consistent with the previous calculation (Isaev et al., 2007).

Calculated parameters of static and 300-K third-order Birch-Murnaghan EOS of the fcc phase are shown in Table1. As usual, calculated 300-K volume is larger than static one. It is mainly due to the effect of the zero-point motion. The static FM and NM EOS are approximately consistent with the previous calculations (Elsässer et al., 1998; Bazhanova et al., 2012). V_0 of the FM state was larger than that of the NM state, and K_0 of the FM state was smaller than that of the NM state.

§4. Discussion

From the experimental results, we determined the stable crystal structure of FeH_x by two criteria; a phase appeared or grew during heating.

Although we could not constrain the strict transition pressure from dhcp to fcc, experimental results suggest that the stable crystal structure of FeH_x (x~1) was fcc at 55 to 137 GPa (Fig. 7). To our knowledge, this is the first report that experimentally observed the dhcp-fcc transition of FeH_x at relatively high pressure and low temperature, as predicted by theoretical calculations (Isaev et al., 2007). Formation of dhcp FeH_x has been reported at pressures above 70 GPa in the previous experimental studies (Ohtani et al., 2005; Saxena et al., 2004), which contradicts the present results. This discrepancy could be attributed to the difference in stoichiometry. The hydrogen content x of dhcp FeH_x synthesized by Saxena et al. (2004) and Ohtani et al. (2005) was 0.3 and 0.8-0.9, respectively. Additionally, dhcp FeH_x was associated with pure hcp iron in both studies, suggesting that their system was unsaturated in hydrogen. In the present study, fcc FeH_x was near stoichiometric and excess hydrogen existed in our experiments. If this is the case, the stable crystal structure of FeH_x is strongly affected by the hydrogen content; fcc is stable for stoichiometric FeH and $x<1$ stabilizes dhcp or hcp. For the investigation of hydrogen in the Earth's core which is unsaturated in hydrogen, physical properties of dhcp and hcp structure should be considered rather than fcc.

The stable phase results of FeH_x (x~1) by the present study and Sakamaki et al. (2009) suggest that dhcp structure is stable at relatively low pressure and temperature conditions, and transforms to fcc structure with increasing pressure or temperature. Therefore, the *P/T* slope of the dhcp-fcc phase boundary is positive at 10-20 GPa, and would become negative at

around 30 GPa (Fig. 8). This type of *P-T* phase relation has been reported for a group VIII 3d-transition element, cobalt, where the stability range of hcp is limited to low pressures and temperatures, and fcc is stable at high pressure and temperature (Yoo et al. 2000). Kuwayama et al. (2008) argued that all group VIII 3d-transition elements might have fcc structure at high pressures.

Experimental volumes and EOS parameters are close to calculated FM one up to ~60 GPa and become closer to calculated NM one under higher pressures (Table 1, Fig. 5). This indicates the existence of a magnetic transition from the magnetic state to the nonmagnetic state at ~60 GPa, being inconsistent with the Mössbauer spectroscopy by Narygina et al., (2011) which stated that fcc FeH is non-magnetic or anti-ferromagnetic in at 26-47 GPa. In Narygina et al. (2011), the volume at 26 GPa is ~11.8 Å^3/FeH which is too large to make magnetization vanish according to our calculation for any phase of FeH (Fig. 6). To resolve the discrepancy in magnetization between our results and Narygina et al. (2011), additional observations of magnetization at pressures under 60 GPa may be necessary. Recently, Thompson et al. (2018) performed Mössbauer spectroscopy on fcc FeH_x at 64 and 82 GPa, and found that spin transition is unlikely to occur at this pressure range.

According to our computational results, the FM to NM transition in dhcp FeH takes place at ~10.0 Å^3/FeH, which could cause discontinuity in the compression behavior and might raise the stability of dhcp. However, our experimental results show that fcc is stable at pressure higher than 100 GPa which correspond to <10.0 Å^3/FeH. Therefore, fcc is likely stable at higher

pressures even at pressures corresponding to the Earth's inner core.

§5. Conclusion

The stable crystal structure of nearly stoichiometric FeH_x up to ~140 GPa, as well as the compression curve of fcc FeH_x, was experimentally studied for the first time. In-situ high-pressure X-ray diffraction measurements revealed that the stable structure of FeH_x (x~1) was fcc above 55 GPa. Combined with the low-pressure results by Sakamaki et al. (2009), it is suggested that the stability range of dhcp is limited to low pressure and temperature, and fcc becomes stable at high pressure and temperature. The experimental pressure-volume curve of fcc FeH_x has a discontinuity of compressibility at ~60 GPa. EOS parameters are close to the calculated FM at <60 GPa and get closer to the calculated NM one at >60 GPa. This indicates that a magnetic transition take place at ~60 GPa, which is consistent with the magnetic moment calculation. Dhcp FeH_x also undergoes a FM to NM transition at ~10.0 $Å^3$/FeH, but fcc remains stable at <10.0 $Å^3$/FeH. Therefore, it is likely that fcc remains stable at higher pressures.

References

Badding, J. V., Hemley, R. J., Mao, H. K. (1991). High-pressure chemistry of hydrogen in metals: In situ study of iron hydride. Science, 253(5018), 421.

Baroni, S., De Gironcoli, S., Dal Corso, A., Giannozzi, P. (2001). Phonons and related crystal properties from density-functional perturbation theory. Reviews of Modern Physics, 73(2), 515.

Bazhanova, Z. G., Oganov, A. R., Gianola, O. (2012). Fe–C and Fe–H systems at pressures of the Earth's inner core. Physics-Uspekhi, 55, 489-497.

Boehler, R., Bargen, N. V., Chopelas, A. (1990). Melting, thermal expansion, and phase transitions of iron at high pressures. Journal of Geophysical Research: Solid Earth, 95(B13), 21731-21736.

Chi, Z., Nguyen, H., Matsuoka, T., Kagayama, T., Hirao, N., Ohishi, Y., Shimizu, K. (2011). Cryogenic implementation of charging diamond anvil cells with H_2 and D_2. Review of Scientific Instruments, 82(10), 105109.

Dewaele, A., Belonoshko, A. B., Garbarino, G., Occelli, F., Bouvier, P., Hanfland, M., Mezouar, M. (2012). High-pressure–high-temperature equation of state of KCl and KBr. Physical Review B, 85(21), 214105.

Dorogokupets, P. I., Oganov, A. R. (2007). Ruby, metals, and MgO as alternative pressure scales: A semiempirical description of shock-wave, ultrasonic, x-ray, and thermochemical data at high temperatures and pressures. Physical Review B, 75(2), 024115.

Elsässer, C., Zhu, J., Louie, S. G., Meyer, B., Fähnle, M., Chan, C. T. (1998). Ab initio study of iron and iron hydride: II. Structural and magnetic properties of close-packed Fe and FeH. Journal of Physics: Condensed Matter, 10(23), 5113.

Fukai, Y. (1992). Some properties of the Fe-H system at high pressures and temperatures, and their implications for the Earth's core, in High-Pressure Res: Appl. to Earth Planet. Sci., vol. 67, 373–385, TERRAPUB, Washington D. C., doi: 10.1029/GM067p0373.

Giannozzi, P., Baroni, S., Bonini, N., Calandra, M., Car, R., Cavazzoni, C., Ceresoli, D., Chiarotti, G. L., Cococcioni, M., Dabo, I., Dal Corso, A., Fabris, S., Fratesi, G., de Gironcoli, S., Gebauer, R., Gerstmann, U., Gougoussis, C., Kokalj, A., Lazzeri, M., Martin-Samos, L., Marzari, N., Mauri, F., Mazzarello, R., Paolini, S., Pasquarello, A., Paulatto, L., Sbraccia, C., Scandolo, S., Sclauzero, G., Seitsonen, A. P., Smogunov, A., Umari, P., Wentzcovitch, R. M. (2009). QUANTUM ESPRESSO: a modular and open-source software project for quantum simulations of materials. Journal of physics: Condensed matter, 21(39), 395502.

Giannozzi, P., De Gironcoli, S., Pavone, P., Baroni, S. (1991). Ab initio calculation of phonon dispersions in semiconductors. Physical Review B, 43(9), 7231.

Isaev, E. I., Skorodumova, N. V., Ahuja, R., Vekilov, Y. K., Johansson, B. (2007). Dynamical stability of Fe-H in the Earth's mantle and core regions. Proceedings of the National Academy of Sciences, 104(22), 9168-9171.

Kuwayama, Y., Hirose, K., Sata, N., Ohishi, Y. (2008). Phase relations of iron and iron–nickel alloys up to 300 GPa: Implications for composition and structure of the Earth's inner core. Earth and Planetary Science Letters, 273(3-4), 379-385.

Li, F., Wang, D., Du, H., Zhou, D., Ma, Y., Liu, Y. (2017). Structural evolution of FeH4 under high pressure. RSC Advances, 7(21), 12570-12575.

Machida, A., Saitoh, H., Sugimoto, H., Hattori, T., Sano-Furukawa, A., Endo, N., Katayama, Y., Iizuka, R., Sato, T., Matsuo, M., Orimo, S., Aoki, K. (2014). Site occupancy of interstitial deuterium atoms in face-centred cubic iron. Nature communications, 5, 5063.

Methfessel, M. P. A. T., Paxton, A. T. (1989). High-precision sampling for Brillouin-zone integration in metals. Physical Review B, 40(6), 3616.

Murphy, C. A. (2016). Hydrogen in the Earth’s Core: Review of the Structural, Elastic, and Thermodynamic Properties of Iron - Hydrogen Alloys. Deep Earth: Physics and Chemistry of the Lower Mantle and Core, 217, 255.

Narygina, O., Dubrovinsky, L. S., McCammon, C. A., Kurnosov, A., Kantor, I. Y., Prakapenka, V. B., Dubrovinskaia, N. A. (2011). X-ray diffraction and Mössbauer spectroscopy study of fcc iron hydride FeH at high pressures and implications for the composition of the Earth's core. Earth and Planetary Science Letters, 307(3), 409-414.

Ohta, K., Ichimaru, K., Einaga, M., Kawaguchi, S., Shimizu, K., Matsuoka, T., Hirao, N., Ohishi, Y. (2015). Phase boundary of hot dense fluid hydrogen. Scientific reports, 5, 16560.

Ohtani, E., Hirao, N., Kondo, T., Ito, M., Kikegawa, T. (2005). Iron-water reaction at high pressure and temperature, and hydrogen transport into the core. Physics and chemistry of minerals, 32(1), 77-82.

Perdew, J. P., Burke, K., Ernzerhof, M. (1996). Generalized gradient approximation made simple. Physical review letters, 77, 3865; Erratum: Physical review letters, 78, 1396 (1997).

Pépin, C. M., Dewaele, A., Geneste, G., Loubeyre, P., Mezouar, M. (2014). New iron hydrides under high pressure. Physical review letters, 113(26), 265504.

Pépin, C. M., Geneste, G., Dewaele, A., Mezouar, M., Loubeyre, P. (2017). Synthesis of FeH5: A layered structure with atomic hydrogen slabs. Science, 357(6349), 382-385.

Poirier, J. P. (1994). Light elements in the Earth's outer core: a critical review. Physics of the earth and planetary interiors, 85(3-4), 319-337.

Saitoh, H., Machida, A., Sugimoto, H., Yagi, T., Aoki, K. (2017). *P–V–T* relation of the Fe–H system under hydrogen pressure of several gigapascals. Journal of Alloys and Compounds, 706, 520-525.

Sakamaki, K., Takahashi, E., Nakajima, Y., Nishihara, Y., Funakoshi, K., Suzuki, T., Fukai, Y. (2009). Melting phase relation of FeH_x up to 20GPa: Implication for the temperature of the Earth's core. Physics of the Earth and Planetary Interiors, 174(1), 192-201.

Saxena, S. K., Liermann, H. P., Shen, G. (2004). Formation of iron hydride and high-magnetite at high pressure and temperature. Physics of the Earth and Planetary Interiors, 146(1), 313-317.

Tagawa, S., Ohta, K., Hirose, K., Kato, C., Ohishi, Y. (2016). Compression of Fe–Si–H alloys to core pressures. Geophysical Research Letters, 43(8), 3686-3692.

Terasaki, H., Ohtani, E., Sakai, T., Kamada, S., Asanuma, H., Shibazaki, Y, Hirao, H., Sata, N., Ohishi, Y., Sakamaki, T., Suzuki, A., Funakoshi, K. (2012). Stability of Fe–Ni hydride after the reaction between Fe–Ni alloy and hydrous phase (δ-AlOOH) up to 1.2 Mbar: Possibility of H contribution to the core density deficit. Physics of the Earth and Planetary Interiors, 194, 18-24.

Thompson, E. C., Davis, A. H., Bi, W., Zhao, J., Alp, E. E., Zhang, D., Greenberg, E., Prakapenka, V. B., Campbell, A. J. (2018). High-pressure geophysical properties of Fcc phase FeH_x. Geochemistry, Geophysics, Geosystems, 19. https://doi.org/10.1002/2017GC007168

Tsujino, N., Nishihara, Y., Nakajima, Y., Takahashi, E., Funakoshi, K. I., Higo, Y. (2013). Equation of state of γ-Fe: Reference density for planetary cores. Earth and Planetary Science Letters, 375, 244-253.

Ueda, Y., Matsui, M., Yokoyama, A., Tange, Y., Funakoshi, K. I. (2008). Temperature-pressure-volume equation of state of the B2 phase of

sodium chloride. Journal of Applied Physics, 103(11), 113513.

Vanderbilt, D. (1990). Soft self-consistent pseudopotentials in a generalized eigenvalue formalism. Physical Review B, 41(11), 7892.

Wallace, D. (1972). Thermodynamics of Crystals. John Wiley, Hoboken, N. J.

Yoo, C. S., Cynn, H., Söderlind, P., Iota, V. (2000). New β (fcc)-cobalt to 210 GPa. Physical review letters, 84(18), 4132.

Figures and Tables

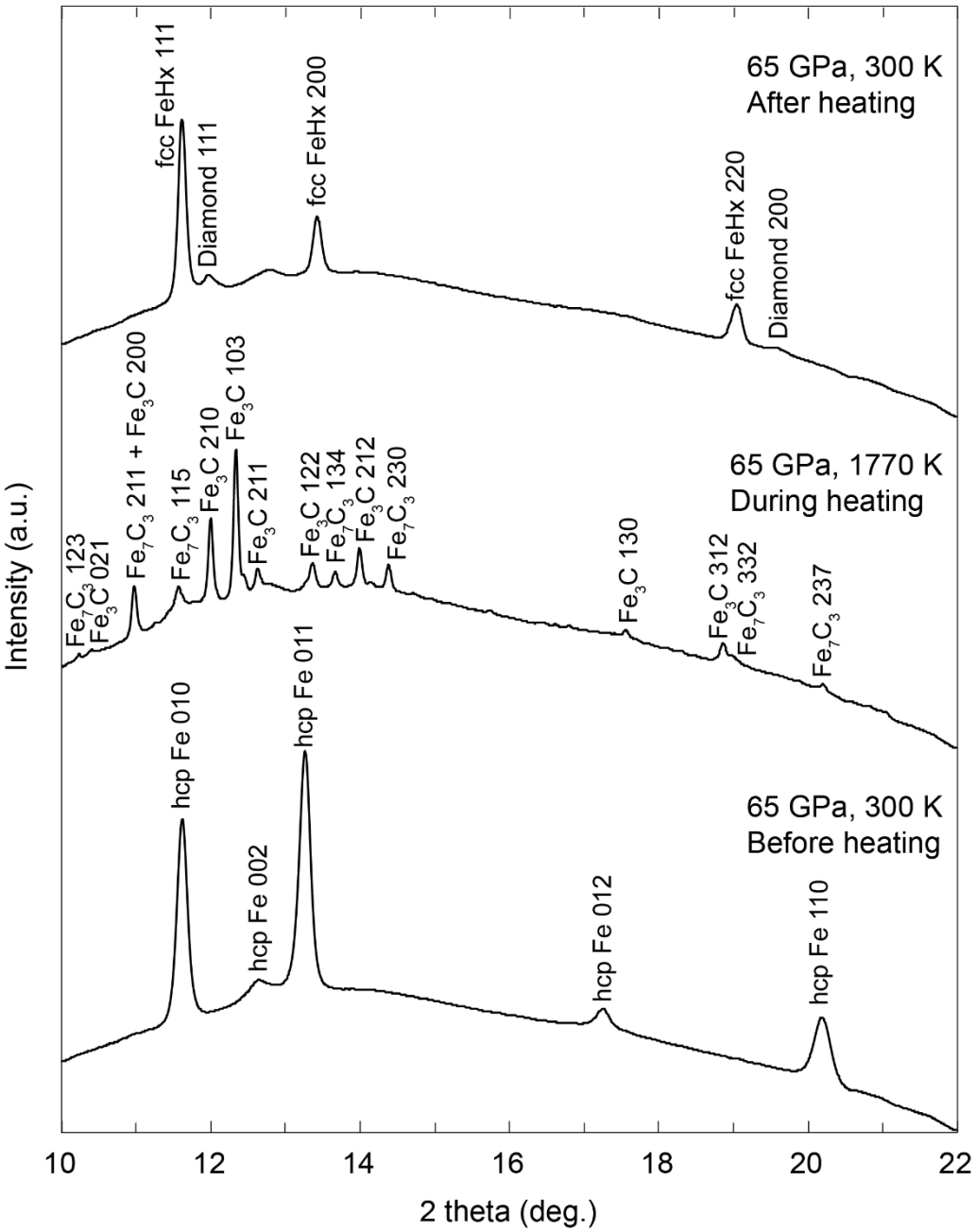

Fig. 1 Representative XRD patterns obtained in a series of laser heating for an iron sample and paraffin pressure medium. (Lower pattern) The diffraction lines from hcp iron obtained at 65 GPa before laser heating. (Middle) XRD peaks from Fe3C and Fe7C3 taken at 65 GPa and 1770 K during laser heating. (Upper) Room temperature XRD peaks from fcc FeHx and diamond that are reaction products of iron and paraffin after laser heating.

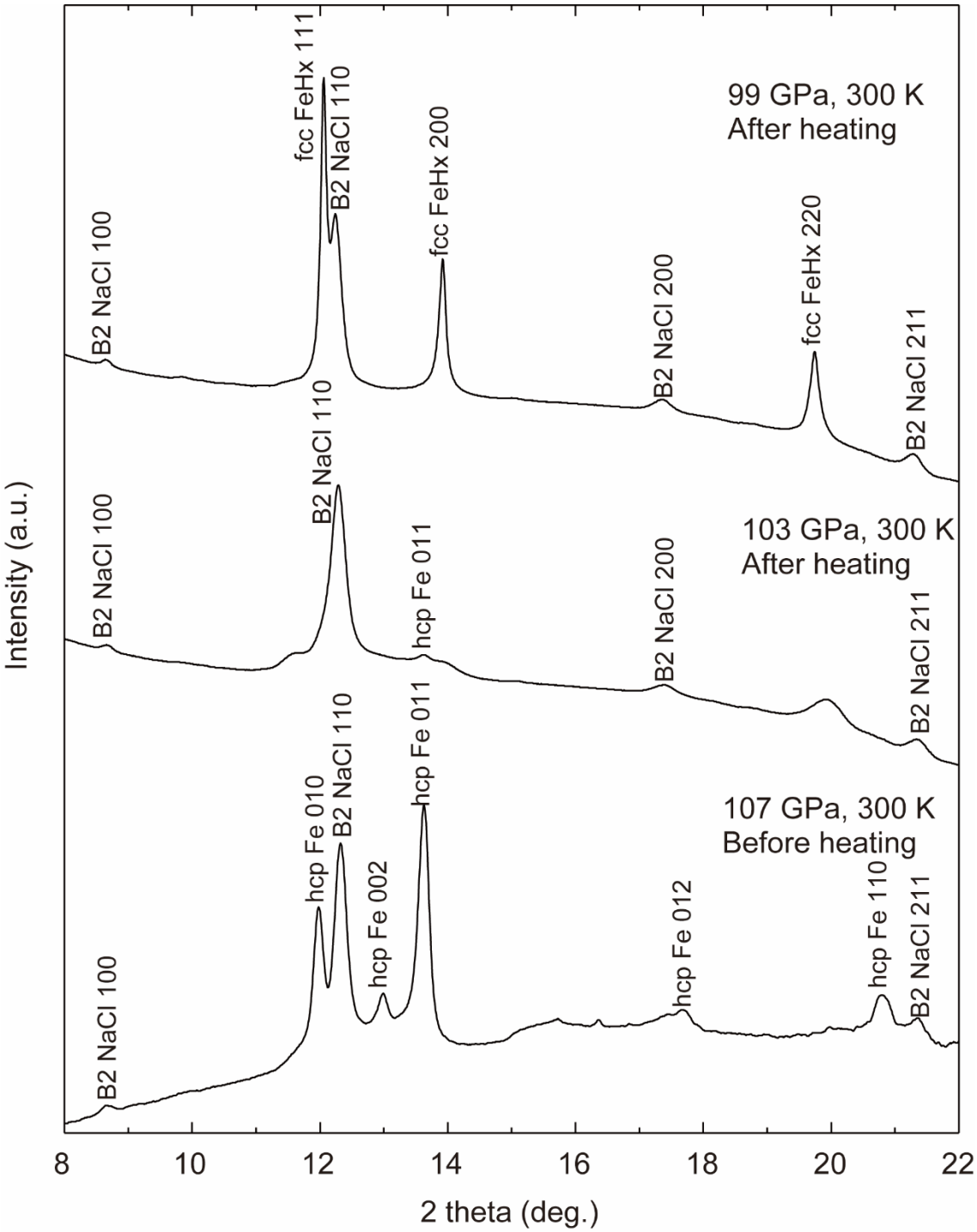

Fig. 2 Representative XRD patterns obtained in a series of laser heating for an iron sample and H2 with NaCl pressure medium. (Lower pattern) The diffraction lines from hcp iron obtained at 107 GPa before laser heating. (Middle) XRD peaks from hcp Fe and halo taken at 103 GPa and 300 K after laser heating. (Upper) XRD peaks from fcc FeHx after laser heating.

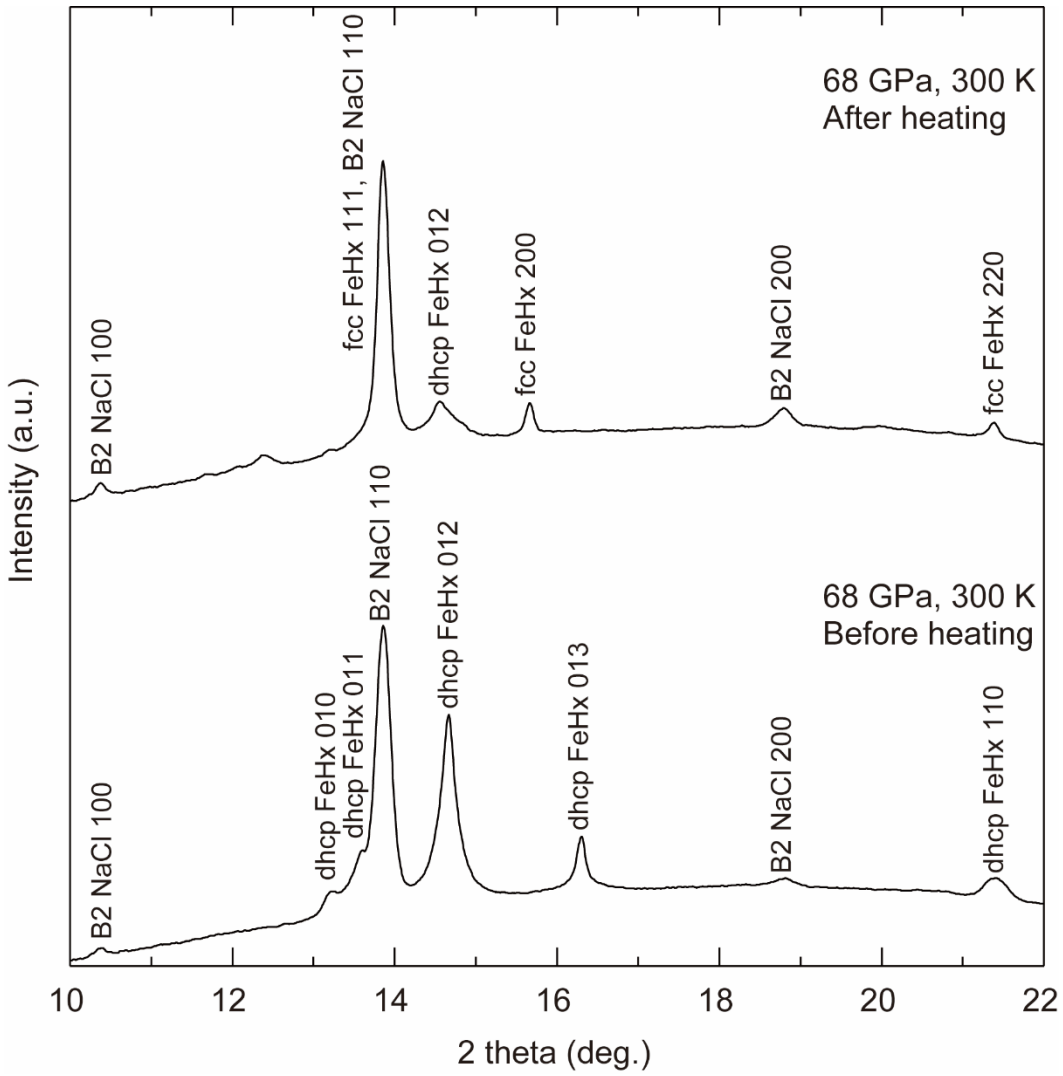

Fig. 3 Representative XRD patterns obtained in a series of laser heatings for an iron sample and H2 with NaCl pressure medium. (Lower pattern) The diffraction lines from dhcp FeHx that are products of reaction of pure iron and H2 at relatively low pressure and temperature during liquid H2 sealing and compression. (Upper) XRD peaks from fcc FeHx after laser heating.

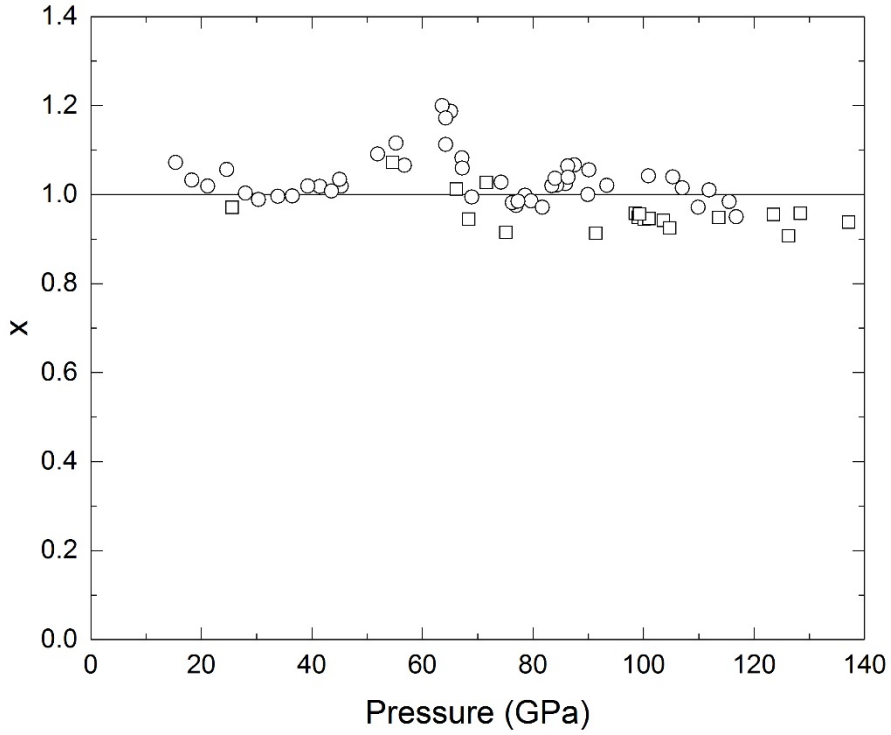

Fig. 4 Hydrogen content x as a function of pressure for fcc FeHx. Circles: synthesized from iron and paraffin (run1-3), rectangles: synthesized from iron and H2 (run4-7).

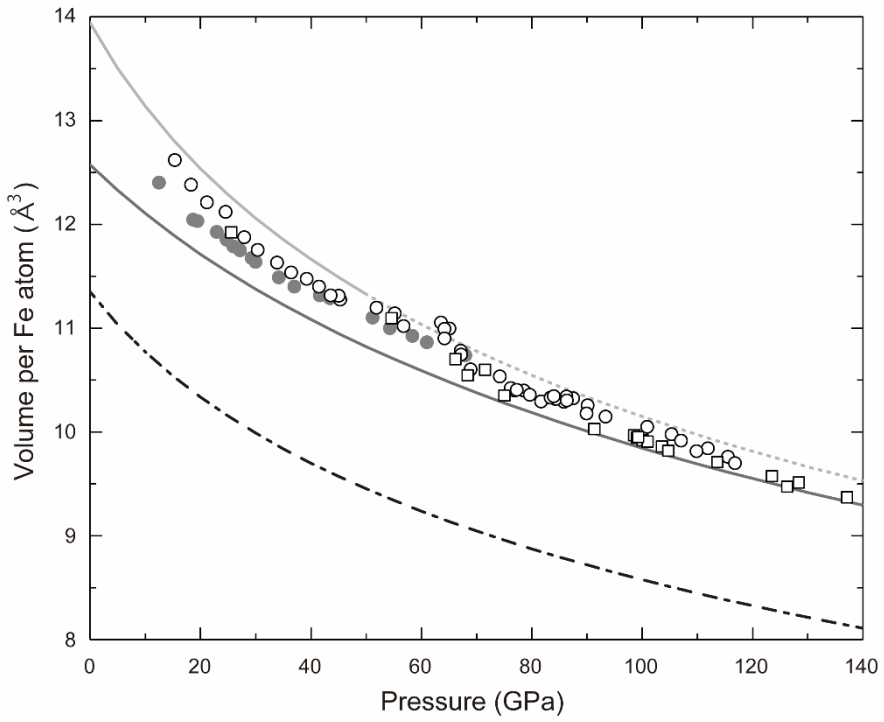

Fig. 5 Volume per iron atom as a function of pressure for fcc FeHx and Fe. Symbols show experimental data for fcc FeHx. Open circles: synthesized from iron and paraffin (run1-3, this study), open rectangles: synthesized from iron and H2 (run4-7, this study), gray circles: synthesized from iron and paraffin (Narygina et al., 2011). Light and dark gray lines are results of the ab initio calculations for FM and NM fcc FeH. Dotted light gray line is for extrapolation. Black dashed line represent the compression curve of iron by Boehler et al., 1990.

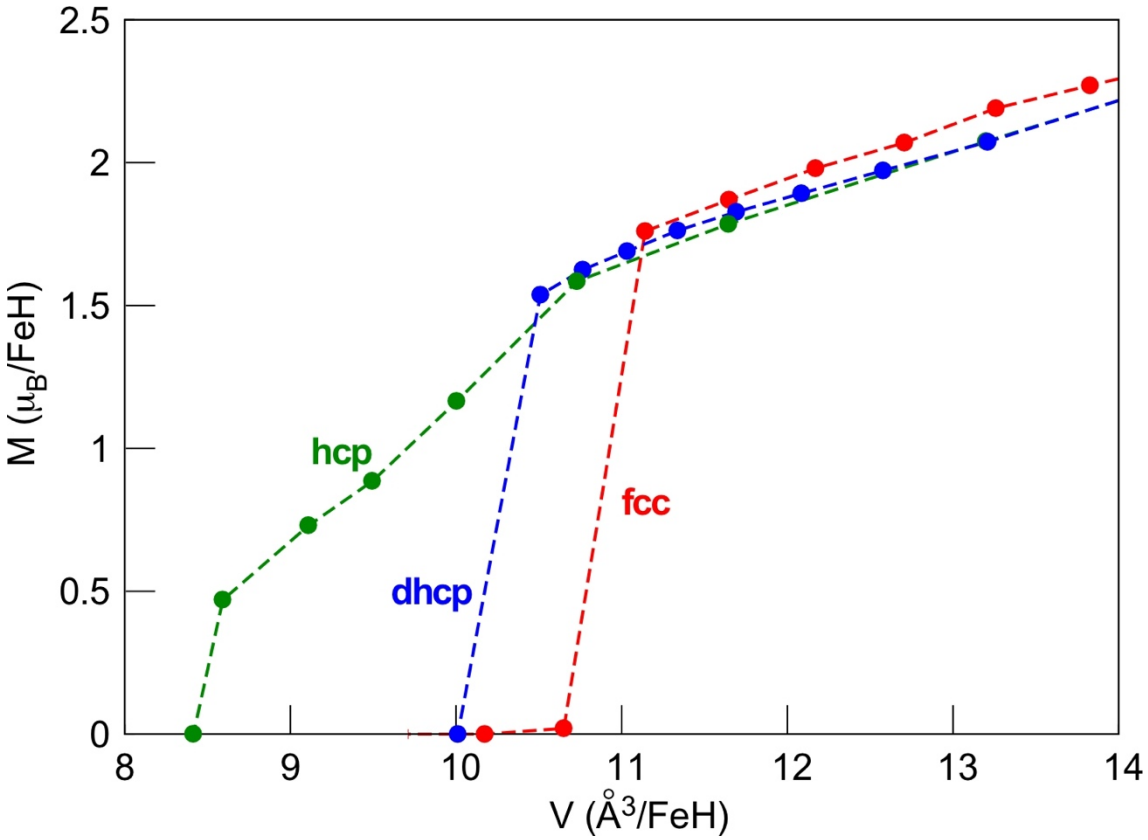

Fig. 6 Magnetic moments calculated for fcc, dhcp, and hcp phases of FeH. Dashed lines are guides for eyes.

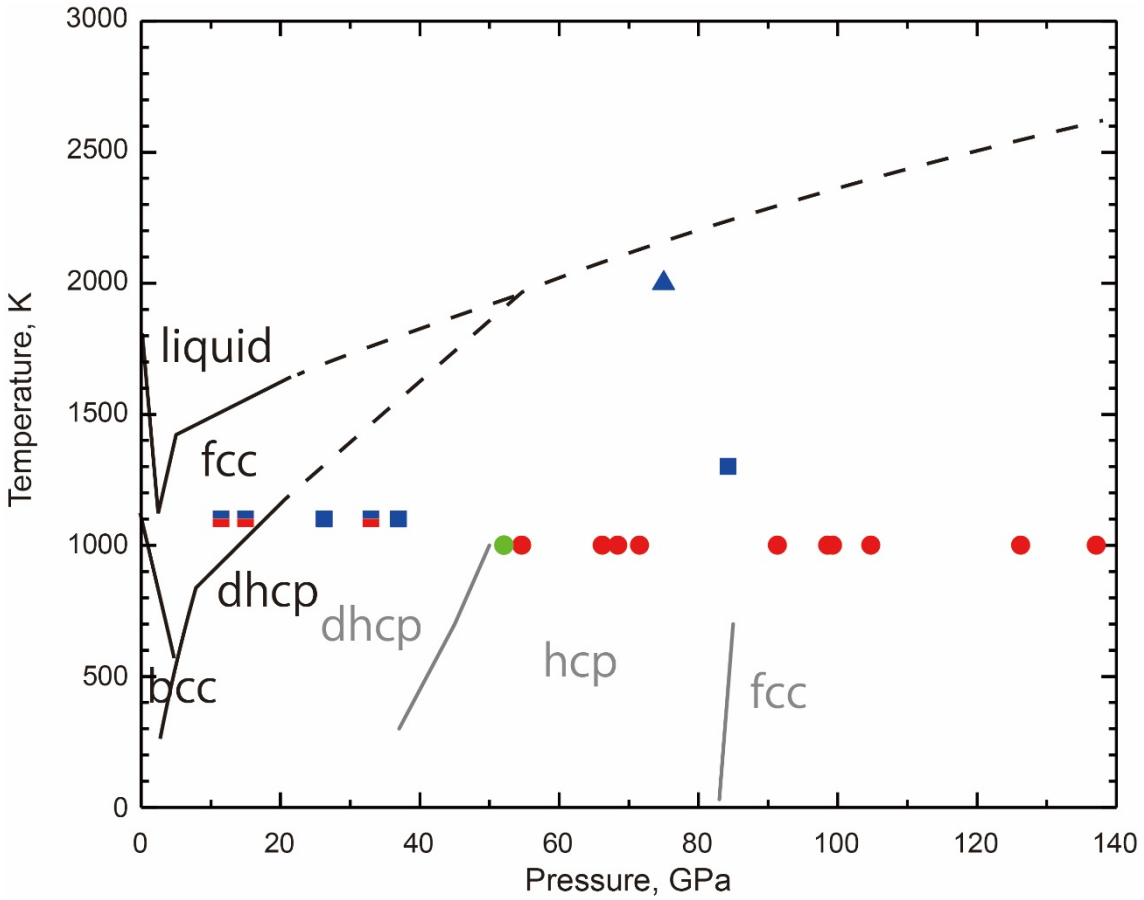

Fig. 7 Pressure-temperature phase diagram of FeHx. Red, blue and green symbols represent experimental results for fcc, dhcp and hcp structures, respectively. Circles, squares and triangle for this study, Ohtani et al. (2005) and Saxena et al. (2004). Black and gray lines indicate the phase boundaries proposed by Sakamaki et al. (2009) and Isaev et al. (2007), respectively. Dashed lines are for extrapolation. Note that hydrogen content x differs between studies.

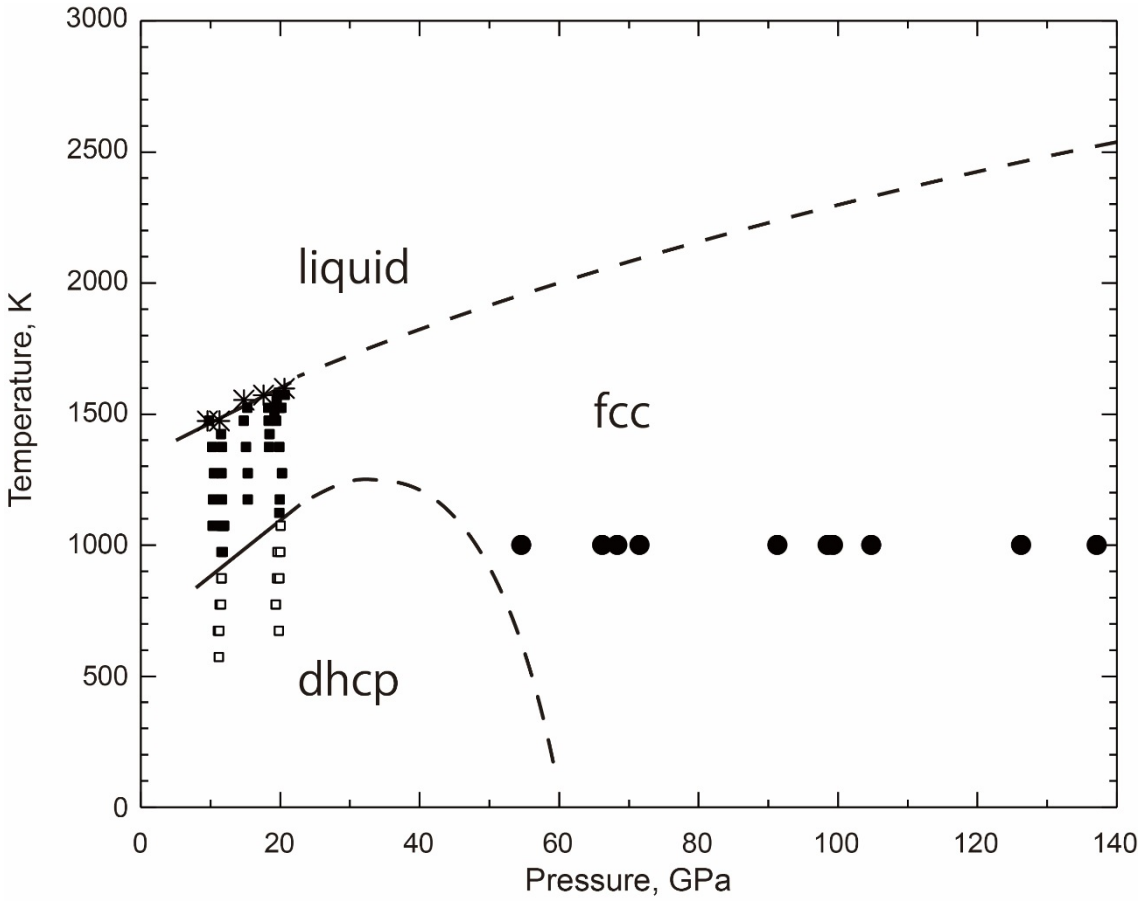

Fig. 8 Pressure-temperature phase diagram of stoichiometric FeH. Closed and open symbols are for fcc and dhcp, respectively. Circles and rectangles represent the results of the present study and Sakamaki et al. (2009). Results of the 'melt' reported by Sakamaki et al. (2009) are shown by the asterisks.

Table 1 Parameters for fcc FeH third-order Birch-Murnaghan equation of states from experimental and ab initio calculations compared with previous studies.

	V_0 (Å^3/Fe)	K_0 (GPa)	K_0'	Pressure range (GPa)	Temperature (K)	
experimental						
fcc $FeH_{x\sim1}$	13.8(7)	100(11)	9.3(16)	15-57	300	This study
	13.1(11)	227(8)	3.4(2)	72-137	300	This study
	13.5(1)	99(5)	11.7(5)	12-68	300	Narygina et al. (2011)
ab initio						
fcc FeH FM	13.5	168	4.5	<50 GPa	0	This study
	13.9	146	4.8	<50 GPa	300	This study
	13.9	155	3.7		0	Elsässer et al. (1998)
fcc FeH NM	12.3	262	4.2		0	This study
	12.6	242	4.3		300	This study
	12.2	271	4.3		0	Bazhanova et al. (2012)
	12.7	248	4.3		0	Elsässer et al. (1998)
Reference						
fcc Fe	11.3	165	5.5	0-16.8	300-1969	Boehler et al. (1990)

Chapter 3

Melting in the FeO–SiO_2 system to deep lower-mantle pressures: Implications for subducted Banded Iron Formations

Chie Kato, Kei Hirose, Ryuichi Nomura, Maxim D. Ballmer, Akira Miyake, and Yasuo Ohishi (2016). Melting in the FeO–SiO_2 system to deep lower-mantle pressures: Implications for subducted Banded Iron Formations, Earth and Planetary Science Letters, 440, 56–61, doi: 10.1016/j.epsl.2016.02.011

Abstract

Banded iron formations (BIFs), consisting of layers of iron oxide and silica, are far denser than normal mantle material and should have been subducted and sunk into the deep lower mantle. We performed melting experiments on Fe_2SiO_4 from 26 to 131 GPa in a laser-heated diamond-anvil cell (DAC). The textural and chemical characterization of a sample recovered from the DAC revealed that SiO_2 is the liquidus phase for the whole pressure range examined in this study. The chemical compositions of partial melts are very rich in FeO, indicating that the eutectic melt compositions in the FeO–SiO_2 binary system are very close to the FeO end-member. The eutectic temperature is estimated to be 3540 ± 150 K at the core–mantle boundary (CMB), which is likely to be lower than the temperature at the top of the core at least in the Archean and Paleoproterozoic eons, suggesting that subducted BIFs underwent partial melting in a thermal boundary layer above the CMB. The FeO-rich melts formed by partial melting of the BIFs were exceedingly dense and therefore migrated downward. We infer that such partial melts have caused iron enrichment in the bottom part of the mantle, which may have contributed to the formation of ultralow velocity zones (ULVZs) observed today. On the other hand, solid residues left after the segregation of the FeO-rich partial melts have been almost pure SiO_2, and therefore buoyant in the deep lower mantle to be entrained in mantle upwellings. They have likely been stretched and folded repeatedly by mantle flow, forming SiO_2 streaks within the mantle "marble cake". Mantle packages enhanced by SiO_2 streaks may be the origin of seismic scatterers in the mid-lower mantle.

§1. Introduction

BIFs are distinctive sedimentary rocks characterized by alternating layers of iron oxides and silica. They occur widely in Archean to Paleoproterozoic terrains all over the world with exposures reaching 1200 m in thickness and several hundred kilometers in extent (see Klein, 2005 for a review). The oldest BIF is found in the 3.8 Ga Isua supracrustal belt, West Greenland. According to Klein (2005), BIFs have been one of the major crustal components of Archean to Paleoproterozoic cratons formed at ~3.5 to ~1.8 Ga. BIF deposition rates have peaked at ~2.5 Ga when the Hamersley Group in Western Australia was formed. Although the detailed mechanism of BIF formation remains unclear, it is robust that they have been formed as a consequence of oxidation of ferrous iron dissolved in seawater. The formation of BIFs stopped at 1.8 Ga, and afterwards has been limited to occasional appearances between 0.8 and 0.6 Ga. The amount of preserved BIFs on the present-day Earth is estimated to be about 1014 - 15tons (Isley, 1995). However, these preservations on cratons are very likely only a small part of the total BIFs ever generated, because at least any BIF generated on oceanic crust should have been conveyed into the deep interior of the Earth through at subduction (Hopkins et al., 2008) or non-plate-tectonic delamination processes (Harris and Bédard, 2014).

Dobson and Brodholt (2005) argued that these subducted BIFs accumulate above the CMB and form the ULVZs. The BIFs are likely to be a mixture of FeO and SiO_2 near the base of the mantle where the oxidation state is near the iron-wüstite buffer. Dobson and Brodholt (2005)

approximated the BIFs to be pure FeO, whose melting temperature was originally reported to be >5000 K at the CMB (Knittle and Jeanloz, 1991), and discussed the possibility that the subducted BIFs remain in a solid state in the mantle. However, the more recent work by Fischer and Campbell (2010), based on measurements up to 77 GPa and the Lindemann's prediction, found that FeO undergoes melting at temperatures above 3690 K at the CMB. This estimate is much lower than the estimates by Knittle and Jeanloz (1991) and Seagle et al. (2008) but consistent with Shen et al. (1993). More importantly, the subducted BIFs are indeed a mixture of FeO and SiO_2, and thus melting occurs at the eutectic temperature in the FeO–SiO_2 binary system, which must be lower than the melting temperature of the FeO end-member.

A melting phase diagram in the FeO–SiO_2 binary system so far has only been investigated at pressures below 17 GPa, using a multi-anvil apparatus (Ohtani, 1979; Kato et al., 1984). These previous studies show that FeO wüstite and SiO_2 stishovite form a eutectic system above 17 GPa.

In this study, we performed melting experiments on Fe_2SiO_4 between 26 and 131 GPa in a laser-heated DAC. The solidus temperature of Fe_2SiO_4, corresponding to the eutectic temperature in the FeO–SiO_2 binary system, was determined from the textural and compositional analyses of DAC samples recovered after pressure release. Our results suggest that the subducted BIFs underwent partial melting near the base of the mantle, which is likely to have contributed to the enrichment in iron above the CMB.

§2. Experimental procedures

Melting experiments were carried out at high pressure by using laser-heated DAC techniques. Synthetic Fe_2SiO_4 (fayalite) was used as a starting material. This composition was chosen because the eutectic melt composition is expected to be FeO-rich rather than SiO_2-rich from the melting temperatures of FeO and SiO_2 end-members. The chemical composition and the homogeneity of the starting material were confirmed by electron microprobe analysis. Either Ar or SiO2 glass was used both as a thermal insulator and as a pressure medium. They were loaded into a sample chamber, a hole drilled on a pre-indented Re gasket. The culet size of diamond anvils was 120 to 300μm depending on a target pressure. After loading, the whole DAC was dried in a vacuum oven at 423 K for >12 h. We then introduced Ar gas and quickly started compression.

After compression to a pressure of interest, the sample was heated from both sides with a couple of single-mode Yb fiber lasers. Temperature was obtained by a spectroradiometric method (Ohishi et al., 2008; Nomura et al., 2014). The highest temperature measured during heating represents an experimental temperature in each run. Temperature within a melt pocket was relatively homogeneous, but the temperature at melt/solid interface was <150 K lower than the maximum temperature of a sample. It means that temperatures only of 'melted' samples are overestimated by that degree. Pressure in the sample chamber was determined from the Raman spectrum of a diamond anvil at room temperature after heating (Akahama and Kawamura, 2006). We consider a contribution of thermal pressure of +11.6 % per 1000 K for a sample with no pressure medium and samples using SiO_2 as

pressure medium on the basis of in-situ X-ray diffraction measurements on a mixture of Fe_2SiO_4 and gold (Fei et al., 2007) at BL10XU, SPring-8. For a couple of runs with Ar pressure medium, we added thermal pressure of 1 GPa per 1000 K according to Dewaele et al. (2007).

After heating at high pressure, samples were recovered from the DAC and processed for textural and chemical characterizations. Cross sections of the sample were obtained with an Ion Slicer (JEOL EM-09100IS) (Tateno et al., 2009) or Focused Ion Beam (FIB, FEI Versa 3D at Tokyo Tech or FEI Quanta 200 3DS at Kyoto University) and subsequently examined by field-emission-type electron microprobe (FE-EPMA, JEOL JXA-8530F).

§3. Results

We carried out a total of eleven separate runs in a pressure range from 26 to 131 GPa (Table 1). In experiments performed at relatively high temperatures (runs #1, 2, 5, 11), an FeO-rich homogeneous area was observed at the center of a heated spot (Fig. 1a, b). Such an FeO-rich part was round and exhibited a non-stoichiometric chemical composition. We therefore interpreted it to be a quenched partial melt. Note that the enrichment in FeO in a hot area is not produced by the Soret effect (Sinmyo and Hirose, 2010), which induces the migration of FeO toward a low-temperature region. In addition, coarse SiO_2 crystals were found coexisting with the FeO-rich quenched partial melt (Fig. 1a, b). Such an SiO_2 phase should be the liquidus (the first crystallizing) phase of coexisting partial melts.

On the other hand, the FeO-dominant region was not observed when

the sample was heated to relatively low temperatures. As an alternative, a heated portion occurred as a mixture of fine-grain FeO and SiO_2 (Fig. 1c), demonstrating a decomposition of Fe_2SiO_4 fayalite starting material into mixed oxides at subsolidus conditions. We did not find $FeSiO_3$ phase in recovered samples.

With the existence/non-existence of an FeO-rich non-stoichiometric round portion (a melt pocket) and coexisting coarse SiO_2 grains as melting criteria, the solidus curve of Fe_2SiO_4 composition was obtained (Fig. 2). Since the solidus temperature of Fe_2SiO_4 is equivalent to a eutectic temperature in the FeO–SiO_2 binary sys-tem, the upper bound for the solidus curve of Fe_2SiO_4 is given by the melting curve of FeO end-member, determined by Fischer and Campbell (2010) and extrapolated to high pressures on the basis of Simon's equation. The lower bound corresponds to our 'not melted' data. These results show that the eutectic temperature is 3540 ± 150 K at the CMB. In runs using silica as an insulator, the bulk composition may have been slightly SiO_2-rich compared to fayalite. However, as far as the system is eutectic, it does not change the solidus temperature.

The chemical compositions of partial melts were determined by microprobe analyses from four runs (Table 2). It was often difficult to obtain a melt composition without contamination from surrounding SiO_2 solid phase when a quenched melt pocket was small. Therefore, SiO_2 concentrations in these partial melts may be overestimated. It is also noted that these partial melts must be richer in SiO_2 than the eutectic melts, because melting experiments were carried out at temperatures higher than the eutectic

temperature. Even so, our results indicate that the eutectic melts are very close to FeO end-member. The silicon concentration in the eutectic melt is less than 0.7wt.% at 123 GPa (Table 2).

§4. Discussion

§4-1. Comparison with melting curves of FeO and SiO_2

The melting curve of FeO has been repeatedly examined at high pressures (Knittle and Jeanloz, 1991; Shen et al., 1993; Seagle et al., 2008; Fischer and Campbell, 2010). The most recent work by Fischer and Campbell (2010) determined the melting temperature of FeO up to 77 GPa in a laser-heated DAC, employing the discontinuity in the temperature vs. emissivity relationship as a melting criterion, which likely reflects an abrupt change in the sample's optical property associated with melting. The Lindemann's law, a model based on thermal vibrations theory that predicts melting temperature from the thermal equation of state, gives a melting curve of FeO consistent with the experiments by Fischer and Campbell (2010), showing its melting temperature to be 3690 K at the CMB.

The present experiments demonstrate that the eutectic melt compositions in the FeO–SiO_2 binary system are strongly enriched in FeO, suggesting that the solidus temperature of Fe_2SiO_4 fayalite should be lower than but close to the melting temperature of FeO end-member. Indeed, our data is in very good agreement with the melting curve of FeO obtained both from experiments (Fischer and Campbell, 2010) and theory (i.e., the Lindemann law; Fig. 2). It is noted that the melting criterion in this study is

different from that used by Fischer and Campbell (2010), but the results are consistent with each other.

While a static experimental study on the melting temperature of SiO_2 was limited to 40 GPa (Shen and Lazor, 1995), the previous shock-wave measurements by Luo and Ahrens (2004) and Lyzenga et al. (1983) reported that SiO_2 melts above ~5000 K at the CMB pressure. Usui and Tsuchiya (2010) performed ab initio two-phase molecular dynamics simulations on SiO_2 and estimated its melting temperature to be about 5900 K at 136 GPa. More recently Millot et al. (2015) found the melting temperature of silica to be 5290 K at the CMB based on laser-driven shock experiments. These works consistently indicate that the melting of SiO_2 occurs at 5000–6000 K at the CMB pressure, much higher than that for FeO (~3690 K), supporting our finding that the eutectic melt composition in the FeO–SiO_2 binary system is very close to the FeO end-member.

§4-2. Melting of subducted BIFs in the lowermost mantle

The present-day temperature at the CMB remains controversial, and previous estimates range from 3300 to 4300 K (see Lay et al., 2008 for a review). Our study suggests that subducted BIFs undergo partial melting above 3540 ± 150 Kat the bottom of the mantle. It is very likely that the CMB temperature was higher than this value, when the subduction of BIFs occurred (i.e., mainly at 3.5 to 1.8 Ga, Klein, 2005). Therefore, any BIFs that have sunk to the deep mantle should have undergone melting. One complexity involves that any partial melting of BIFs may need to be evaluated

in the $FeO–Fe_2O_3–SiO_2$ ternary system, because most but not all of the ferric iron originally included in the BIFs has likely been reduced to ferrous iron in the lowermost mantle, where the oxidation state is close to the iron-wüstite buffer (e.g., McCammon, 2005). In any case, eutectic temperatures should be even lower in the $FeO– Fe_2O_3–SiO_2$ ternary system than in the $FeO–SiO_2$ binary system. Along these lines, BIF melting near the CMB appears unavoidable during the Archean and early Proterozoic eras. It is therefore unlikely that the origin of present-day ULVZs is related to BIFs that never melted, as suggested by Dobson and Brodholt (2005).

§4-3. Formation of ULVZs

Dobson and Brodholt (2005) inferred that the BIF once covered the whole seafloor with a thickness of 500 m, which corresponds to 2×10^8 km^3 in volume, while large uncertainties remain in deposition rate and environment of deposition of the BIFs. However, this could be an under estimation considering the recycling of the oceanic lithosphere during the large time span over which BIFs have been (intermittently) deposited (Isley, 1995; Klein, 2005; Bekker et al., 2010). The volume of the FeO component is about half of the total subducted BIF volume. As discussed below, FeO-rich melts formed by partial melting of subducted BIFs may have contributed to the formation of ULVZs. As Dobson and Brodholt (2005) mentioned, the total volume of the ULVZs have been estimated at ~10^8 km^3 (Persh and Vidale, 2004) which is comparable to the total volume of subducted BIFs.

It is likely that BIF melting occurred over a range of depths, because

of thermal equilibration during BIF sinking. These depths depend not only on the thermal structure in the lowermost mantle, which has likely been laterally heterogeneous, but also on BIF sinking speeds, which have likely been different for each BIF. First, let's consider the case that the melting of the BIFs started in a thermal boundary layer near the CMB (but before BIFs reached the very bottom of the mantle). Any partial melts would have been strongly enriched in FeO, depending on the degree of partial melting, and thus migrated downward, causing metasomatism (or assimilation) of ambient-mantle materials that may have produced a range of FeO-rich materials in the lowermost mantle. Since the presence of FeO generally acts to decrease melting temperatures, such metasomatism has likely induced partial melting of lowermost-mantle materials at 3.5 to 1.8 Ga (depending on mantle thermal structure at that time). The recent thermodynamical modeling by Boukaré et al. (2015) establishes the ternary phase diagram in the MgO–FeO–SiO_2 system at 130 GPa, an analogue model for FeO-rich mantle melts, and demonstrates that the eutectic point is on the FeO–SiO_2 join. This finding indicates that the metasomatized (FeO-enriched) lowermost mantle could still be partially molten even today, as long as CMB temperature is higher than 3540 ± 150 K determined above. Such partially molten FeO-rich patches may represent the ULVZs (e.g., Williams and Garnero, 1996).

On the other hand, if the present-day CMB temperature is lower than that value, the metasomatized lowermost mantle is now solid, but may nevertheless provide an explanation for ULVZs. The low compressional and shear wave velocities and the high Poisson's ratio of the ULVZs have indeed

been attributed to solid iron-rich post-perovskite (Mao et al., 2006) or magnesiowüstite (Wicks et al., 2010).

For the alternative case of limited metasomatism, it is also possible that dense, strongly FeO-enriched partial melts reached the CMB to form a thin layer of melt on top of the liquid outer core. Limited metasomatism may result for a subset of subducted BIFs, depending on the depth range of BIF melting as well as the dynamics of downward melt migration. In this case, chemical re-action between FeO-rich melts and the outer core should have followed, enriching the topmost core in oxygen. Due to the diffusion of oxygen, such an O-rich layer may extend up to ~100 km at the present day (Buffett and Seagle, 2010). However, the addition of oxygen from the FeO component of all BIFs ever subducted could cause increase in oxygen-content of the top 100 km layer of the outer core by up to ~0.08 wt. % on average, which has negligible effect on the core's seismic properties.

§4-4. Implications for mid-lower mantle scatterers

The partial melting of the BIFs left a single-phase SiO_2 solid residue, which is quite buoyant in the deep lower mantle (Hirose et al., 2005; Andrault et al., 2014). Such SiO_2 blocks could have eventually been entrained by mantle upwellings. They may have been folded repeatedly in the mantle, forming streaks of SiO_2 layers within the mantle "marble cake". The high-temperature equation of state of SiO_2 stishovite obtained by Wang et al. (2012) demonstrates, however, that SiO_2 is neutrally buoyant in the mid-lower mantle at ~65 GPa along a typical lower-mantle temperature profile.

Therefore, streaks of SiO_2 may preferentially have been accumulated at about 1500–1600 km depth, even in the presence of whole-mantle convection and stirring (e.g., Ballmer et al., 2015). Such an accumulation requires decoupling of SiO_2 streaks from ambient-mantle flow. Decoupling of intrinsically stiff SiO_2 streaks (or packages thereof) is favored for low viscosities in the ambient mantle (e.g., in the early Earth), and/or strain localization due to e.g. an inter-connected matrix of the weak (Mg, Fe)O phase (Takeda, 1998; Yamazaki and Karato, 2001; Marquardt and Miyagi, 2015).

The possibility of SiO_2 accumulation in the mid-lower mantle can be tested with seismic observations. A number of seismic reflectors and scatterers have been reported between ~1100 km and ~1800 km depth underneath the circum-Pacific regions, in particular near 1500 km depth (e.g., Kaneshima and Helffrich, 1999, 2010; Niu et al., 2003). Such anomalies require a layer with >4 % slow S-wave velocity, which may be explained by the phase transition in SiO_2 between stishovite and $CaCl_2$-type phase that occurs at 60–70 GPa for high temperatures (Nomura et al., 2010). It has been found that this transition causes a considerable reduction in shear modulus and thus can lead to a large decrease in shear velocity of ~25 % at the depths of the phase transition (and of 12–15 % at depths 100 km above or below) (Carpenter et al., 2000). Kaneshima and Helffrich argued that such seismic scatterers represent former MORB crusts (e.g., Hirose et al., 2005; Ricolleau et al., 2010). It is, however, difficult to explain the >4 % S-wave velocity reduction by the presence of MORB alone (albeit not impossible), because MORB contains only up to 20 % SiO_2 phase in the lower mantle. Alternatively

the accumulation of SiO_2 streaks at mid-mantle depths may account for these seismic scatterers. Packages of SiO_2 streaks may match the typical size of the mid-lower mantle scatterers, less than ten kilometers in thickness and several tens of kilometers in width. Depending on the content of SiO_2 within these packages, they may also match the observed seismic characteristics of scatterers. While subducted MORB materials are dense in the lower mantle (Hirose et al., 1999) and should be gravitationally unstable, a "marble-cake" mantle that is strongly enhanced by SiO_2 streaks is neutrally buoyant at 1500–1600 km depth, which coincides with the depth range at which the SiO_2 phase exhibits a low S-wave anomaly.

§5. Conclusion

We have conducted melting experiments on Fe_2SiO_4 between 26 and 131 GPa, in order to examine the fate of subducted BIFs at the base of the mantle. The results demonstrate that the solidus (eutectic) temperature in the FeO–SiO_2 binary system is 3540 ± 150 K at CMB pressures, which is likely lower than the CMB temperature during the Archean and Paleoproterozoic periods, when the subduction of BIFs occurred. The BIFs, therefore, should have undergone partial melting near the CMB. Present experiments also indicate that the chemical composition of the eutectic melt in this FeO–SiO_2 binary system is strongly enriched in FeO, which is also supported by our finding that the eutectic temperature is very similar to that of FeO end-member reported by an earlier experimental study.

We infer that the FeO-rich melts, formed by partial melting of the BIFs,

caused iron enrichment in the lowermost mantle. On one hand, such enrichment may have contributed to the formation of ULVZs observed today at the very base of the mantle. On the other hand, the solid residue consists of single-phase SiO_2, which are buoyant in the deep mantle and thus have been entrained by mantle upwellings. They have likely been deformed by mantle flow, forming a "marble cake" with SiO_2 streaks, potentially with SiO_2 enhancement in the mid mantle, where SiO_2 is neutrally buoyant. We suggest that mantle packages enhanced by SiO_2 streaks are the source of seismic scattering in the mid-lower mantle.

References

Akahama, Y., Kawamura, H. (2006). Pressure calibration of diamond anvil Raman gauge to 310 GPa. J. Appl. Phys.100, 043516.

Andrault, D., Trønnes, R. G., Konôpková, Z., Morgenroth, W., Liermann, H. P., Morard, G., Mezouar, M. (2014). Phase diagram and *P–V–T* equation of state of Al-bearing seifertite at lowermost mantle conditions. Am. Mineral., 99, 2035–2042.

Ballmer, M. D., Schmerr, N. C., Nakagawa, T., Ritsema, J. (2015). Compositional mantle layering revealed by slab stagnation at ~1000-km depth. Sci. Adv., 1, e1500815. http://dx.doi.org/10.1126/sciadv.1500815.

Bekker, A., Slack, J. F., Planavsky, N., Krapež, B., Hofmann, A., Konhauser, K. O., Rouxel, O.J. (2010). Iron formation: the sedimentary product of a complex interplay among mantle, tectonic, oceanic, and biospheric processes. Econ. Geol., 105, 467–508.

Boukaré, C. E., Ricard, Y., Fiquet, G. (2015). Thermodynamics of the MgO–FeO–SiO_2 system up to 140 GPa: application to the crystallization of Earth's magma ocean. J. Geophys. Res., Solid Earth, 120, 6085–6101.

Buffett, B. A., Seagle, C.T. (2010). Stratification of the top of the core due to chemical interactions with the mantle. J. Geophys. Res., Solid Earth, 115, B04407.

Carpenter, M. A., Hemley, R. J., Mao, H. (2000). High-pressure elasticity of stishovite and the $P4_2/mnm \Leftrightarrow Pnnm$ phase transition. J. Geophys. Res., 105, 10807-10816.

Darken, L. S., Gurry, R. W. (1946). The system iron-oxygen. II. Equilibrium and thermo-dynamics of liquid oxide and other phases. J. Am. Chem. Soc., 68, 798–816.

Dewaele, A., Mezouar, M., Guignot, N., Loubeyre, P. (2007). Melting of lead under high pressure studied using second-scale time-resolved X-ray diffraction. Phys. Rev. B, 76, 144106.

Dobson, D. P., Brodholt, J. P. (2005). Subducted banded iron formations as a source of ultralow-velocity zones at the core–mantle boundary. Nature 434, 371–374.

Fei, Y., Ricolleau, A., Frank, M., Mibe, K., Shen, G., Prakapenka, V. (2007). Toward an internally consistent pressure scale. Proc. Natl. Acad. Sci. USA, 104, 9182–9186.

Fischer, R. A., Campbell, A. J. (2010). High-pressure melting of wüstite. Am. Mineral., 95, 1473–1477.

Harris, L. B., Bédard, J. H. (2014). Crustal evolution and deformation in a non-platetectonic Archaean Earth: comparisons with Venus. In: Dilek, Y., Furnes, H. (Eds.), Evolution of Archean Crust and Early Life, Modern Approaches in Solid Earth Sciences, vol.7. Springer, Netherlands, pp.215–291.

Hirose, K., Fei, Y., Ma, Y., Mao, H. (1999). The fate of subducted basaltic crust in the Earth's lower mantle. Nature, 397, 53–56.

Hirose, K., Takafuji, N., Sata, N., Ohishi, Y. (2005). Phase transition and density of subducted MORB crust in the lower mantle. Earth Planet. Sci. Lett., 237, 239–251.

Hopkins, M., Harrison, T. M., Manning, C. E. (2008). Low heat flow inferred from >4 Gyr zircons suggests Hadean plate boundary interactions. Nature, 456, 493–496.

Isley, A. E. (1995). Hydrothermal plumes and the delivery of iron to banded iron for-mation. J. Geol., 103, 169–185.

Kaneshima, S., Helffrich, G. (1999). Dipping low-velocity layer in the mid-

lower mantle: evidence for geochemical heterogeneity. Science, 283, 1888–1891.

Kaneshima, S., Helffrich, G. (2010). Small scale heterogeneity in the mid-lower mantle beneath the circum-Pacific area. Phys. Earth Planet. Inter., 183, 91–103.

Kato, T., Ohtani, E., Kumazawa, M. (1984). Effect of high pressure on the melting relation of the Fe_2SiO_4 – $FeSiO_3$ system. J. Phys. Earth, 32, 97–111.

Klein, C. (2005). Some Precambrian banded iron-formations (BIFs) from around the world: their age, geologic setting, mineralogy, metamorphism, geochemistry, and origins. Am. Mineral., 90, 1473–1499.

Knittle, E., Jeanloz, R. (1991). The high pressure phase diagram of $Fe_{0.94}O$: apossible constituent of the Earth's core. J. Geophys. Res., 96, 16169–16180.

Lay, T., Hernlund, J., Buffett, B. A. (2008). Core–mantle boundary heat flow. Nat. Geosci., 1, 25–32.

Luo, S. N., Ahrens, T. J. (2004). Shock-induced superheating and melting curves of geo-physically important minerals. Phys. Earth Planet. Inter., 143–144, 369–386.

Lyzenga, G. A., Ahrens, T. J., Mitchell, A. C. (1983). Shock temperatures of SiO_2 and their geophysical implications. J. Geophys. Res., 88, 2431–2444.

Mao, W. L., Mao, H. K., Sturhahn, W., Zhao, J., Prakapenka, V. B., Meng, Y., Shu, J., Fei, Y., Hemley, R. J. (2006). Iron-rich post-perovskite and the origin of ultralow-velocity zones. Science, 312, 564–565.

Marquardt, H., Miyagi, L. (2015). Slab stagnation in the shallow lower mantle

linked to an increase in mantle viscosity. Nat. Geosci., 8, 311–314.

McCammon, C. A. (2005). Mantle oxidation state and oxygen fugacity: constraints on mantle chemistry, structure, and dynamics. In: van Der Hilst, R. D., Bass, J. D., Matas, J., Trampert, J. (Eds.), Earth's Deep Mantle: Structure, Composition, and Evolution. In: Geophys. Monogr., vol. 160, pp.219–240.

Millot, M., Dubrovinskaia, N., ˇCernok, A., Blaha, S., Dubrovinsky, L., Braun, D. G., Cel-liers, P. M., Collins, G. W., Eggert, J. H., Jeanloz, R. (2015). Shock compression of stishovite and melting of silica at planetary interior conditions. Science, 347, 418–420.

Niu, F., Kawakatsu, H., Fukao, Y. (2003). Seismic evidence for chemical heterogene-ity in the midmantle: astrong and slightly dipping seismic reflector beneath the Mariana subduction zone. J. Geophys. Res., 108. http://dx.doi.org/10.1029/2002JB002384.

Nomura, R., Hirose, K., Sata, N., Ohishi, Y. (2010). Precise determination of post-stishovite phase transition boundary and implications for seismic heterogeneities in the mid-lower mantle. Phys. Earth Planet. Inter., 183, 104–109.

Nomura, R., Hirose, K., Uesugi, K., Ohishi, Y., Tsuchiyama, A., Miyake, A., Ueno, Y. (2014). Low core–mantle boundary temperature inferred from the solidus of pyrolite. Science, 343, 522–525.

Ohishi, Y., Hirao, N., Sata, N., Hirose, K., Takata, M. (2008). Highly intense monochro-matic X-ray diffraction facility for high-pressure research at SPring-8. High Press. Res., 28, 163–173.

Ohtani, E. (1979). Melting relation of Fe_2SiO_4 up to about 200 kilobars. J. Phys. Earth, 27, 189–208.

Persh, S. E., Vidale, J. E. (2004). Reflection properties of the core–mantle boundary from global stacks of PcP and ScP. J. Geophys. Res., 109,

B04309.

Ricolleau, A., Perrillat, J.-P., Fiquet, G., Daniel, I., Matas, J., Addad, A., Menguy, N., Cardon, H., Mezouar, M., Guignot, N. (2010). Phase relations and equation of state of a natural MORB: implications for the density profile of subducted oceanic crust in the Earth's lower mantle. J. Geophys. Res., 115, B08202.

Seagle, C. T., Heinz, D. L., Campbell, A. J., Prakapenka, V. B., Wanless, S. T. (2008). Melting and thermal expansion in the Fe–FeO system at high pressure. Earth Planet. Sci. Lett., 265, 655–665.

Shen, G., Lazor, P., Saxena, S. K. (1993). Melting of wüstite and iron up to pressures of 600 kbar. Phys. Chem. Miner., 20, 91–96.

Shen, G., Lazor, P. (1995). Measurement of melting temperatures of some minerals under lower mantle pressures. J. Geophys. Res., 100, 17699–17713.

Sinmyo, R., Hirose, K. (2010). The Soret diffusion in laser-heated diamond-anvil cell. Phys. Earth Planet. Inter., 180, 172–178.

Takeda, Y. (1998). Flow in rocks modelled as multiphase continua: application to polymineralic rocks. J. Struct. Geol., 20, 1569–1578.

Tateno, S., Sinmyo, R., Hirose, K., Nishioka, H. (2009). The advanced ion-milling method for preparation of thin film using ion slicer: application to a sample recovered from diamond-anvil cell. Rev. Sci. Instrum., 80, 013901.

Usui, Y., Tsuchiya, T. (2010). Ab initio two-phase molecular dynamics on the melting curve of SiO_2. J. Earth Sci., 21, 801–810.

Wang, F., Tange, Y., Irifune, T., Funakoshi, K. (2012). *P*–*V*–*T* equation of state of stishovite up to mid-lower mantle conditions. J. Geophys. Res., 117, B06209.

Wicks, J. K., Jackson, J. M., Sturhahn, W. (2010). Very low sound velocities in iron-rich (Mg, Fe)O: implications for the core–mantle boundary region. Geophys. Res. Lett., 37, L15304.

Williams, Q., Garnero, E. J. (1996). Seismic evidence for partial melt at the base of Earth's mantle. Science, 273, 1528–1530.

Yamazaki, D., Karato, S. (2001). Some mineral physics constraints on the rheology and geothermal structure of Earth's lower mantle. Am. Mineral., 86, 385–391.

Figures and Tables

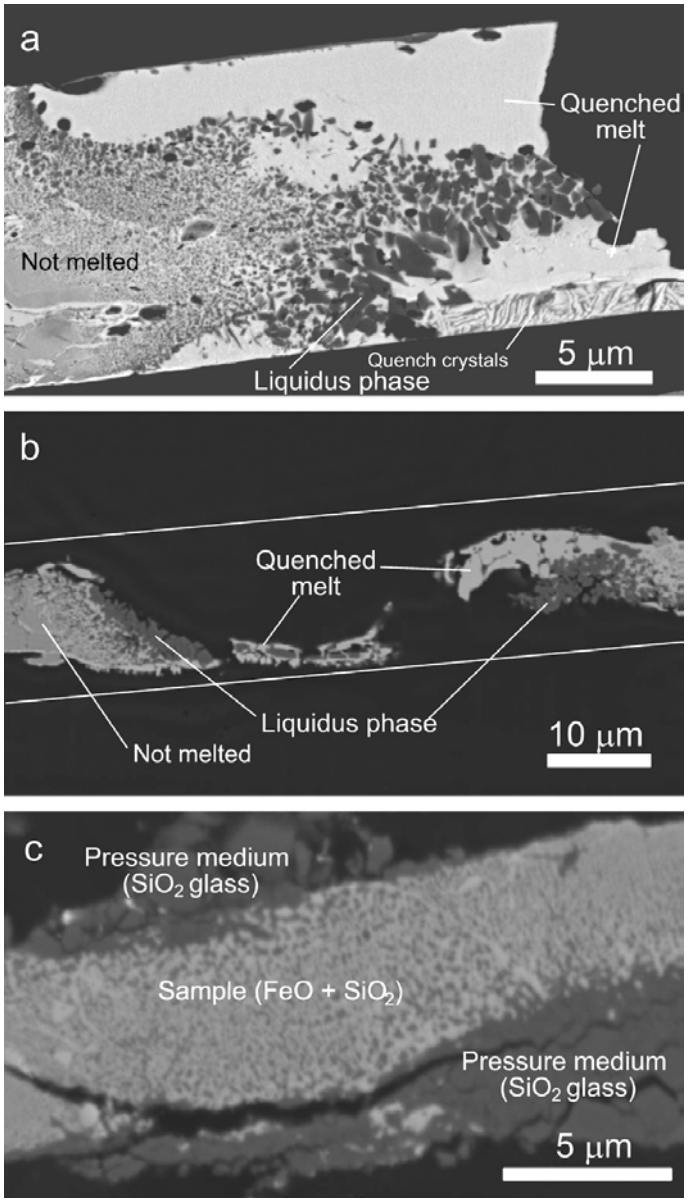

Fig. 1 Backscattered electron images of the cross-sections of melted (a, run #1; b, run #5) and not-melted samples (c, run #3). (a) Two bright regions at the top and the bottom represent a quenched partial melt, surrounded by large dark grains of SiO_2 (a liquidus phase). Quench crystals were found in the bottom melt pool. Subsolidus phase assemblage of fine-grained FeO and SiO_2 mixture was present at a low temperature portion. (b) Quenched partial melt was observed at the center surrounded by solid SiO_2. The sample was deformed during decompression. Dashed lines indicate the location of diamond anvils. (c) Mixture of fine grains FeO and SiO_2 at the hot spot, formed by a decomposition of fayalite.

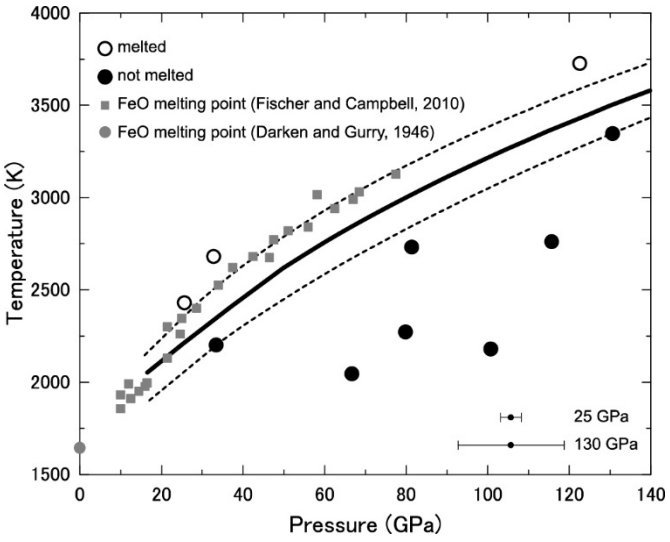

Fig.2. The solidus curve of Fe_2SiO_4, corresponding to the eutectic melting curve in the FeO–SiO_2 binary system to the deep lower mantle. Melted and not-melted samples obtained in this study are shown by open and closed circles, respectively. Gray circle and squares indicate the previously determined melting temperatures of FeO at 1 bar (Darken and Gurry, 1946) and at high pressures (Fischer and Campbell, 2010). The upper and lower bounds of the melting curve are given by the melting temperature of FeO end-member and by not-melted experiments, respectively.

Table1. Experimental conditions of melted/not melted samples.

Melted				Not melted			
Run #	P (GPa)	T (K)	Insulator	Run #	P (GPa)	T (K)	Insulator
1	49	not measured	Ar	3	80	2270	SiO_2
2	26	2430	none	4	67	2050	SiO_2
5	33	2680	Ar	6	81	2730	SiO_2
11	123	3730	SiO_2	7	33	2200	SiO_2
				8	116	2760	SiO_2
				9	131	3350	SiO_2
				10	101	2180	SiO_2

Table 2. SiO_2 concentrations of the quenched melts.

Run #	P (GPa)	T (K)	Insulator	SiO_2 content (wt.%)
1[a]	49	not measured	Ar	6.20 ± 0.44
1[a]	49	not measured	Ar	2.9 ± 1.0
2	26	2430	none	4 .7 ± 1.1
5	33	2680	Ar	0 .70 ± 0.08
11	123	3730	SiO_2	0.63 ± 0.05

a Two separate quenched melt pools were present in run #1.

Chapter 4

Paleomagnetic studies on single crystals

Abstract

To investigate geomagnetic field behavior through geological time, granitic rocks could be good samples to study because of their nearly continuous record and long cooling times that can average out relatively short-term fluctuations of the geomagnetic field. However, paleomagnetic measurements on whole-rock granitic samples are often disturbed by alterations like weathering and lightning, and the presence of magnetically-viscous multi-domain magnetite.

One of the approaches to avoid weathering disturbances (but not lightning) is to separate single silicate crystals from granitic rocks and conduct paleomagnetic and rock magnetic measurements on them. To provide solid ground for single silicate crystal paleomagnetism, paleointensity and rock-magnetic properties of single crystals should be systematically studied and compared to those of the host granitic rock.

We studied zircons, quartzes and plagioclases separated from a Cretaceous granite sample whose whole-rock paleointensity and rock-magnetic properties were studied previously, and found to be particularly stable and reproducible. We first measured the intensity of natural remanent magnetization of several hundred samples for each mineral. Rock-magnetic property measurements such as low-temperature magnetometry, stepwise thermal demagnetization and hysteresis loop measurements were then performed on samples that had significant NRM. The occurrence of magnetite-bearing samples was very low in zircon and quartz. We focused our paleointensity studies on plagioclase, which was the most suitable mineral in

case of the studied rock. Measurements were carried out using the superconducting quantum interference device (SQUID) magnetometer, magnetic property measurement system (MPMS) and Alternating Gradient Magnetometer (AGM) at Center for Advanced Marine Core Research, Kochi University.

We performed paleointensity experiments by the Tsunakawa-Shaw method on 17 plagioclase crystals. Nine samples passed the standard selection criteria for reliable paleointensity determinations. The obtained mean value was consistent with the reported whole-rock paleointensity. We conclude that paleointensity measurements were applicable to plagioclase, but to produce results comparable to conventional whole-rock methods large numbers of crystals that cooled together would need to be studied.

To search for a suitable plagioclase sample, Magnetic hysteresis and low-temperature magnetometry measurements were carried out on plagioclases separated from 22 granitic rocks. We found that granites in the magnetite series with relatively low susceptibility should be focused in the searching for suitable samples for paleointensity experiments.

§1. Introduction

Understanding the long-term evolution of the geomagnetic field is a key for constraining the thermal evolution of the deep Earth, mantle convection, and the preservation of a surface environment conducive to life. Previous studies are pointing out correlations between the behavior of geomagnetic field and some important geologic events such as the beginning of core convection, nucleation of the solid inner core (e.g. Aubert et al., 2010; Biggin et al., 2015), and onset of large mantle plumes (e.g. Courtillot and Olson, 2007).

Paleointensity is the strength of the geomagnetic field in the past which characterizes the dynamo activity. Understanding the variation of the paleointensity is crucial because it is possibly related to the amount and heterogeneity of the core-to-mantle heat flux, as well as the reversal frequency (e.g. Larson and Olson, 1991; Glatzmaier et al., 1991; Courtillot and Olson, 2007; Takahashi et al., 2008).

In the laboratory, paleointensity is measured by giving a Thermoremanent magnetization (TRM) in a known field based on assumptions that (1) the primary portion of the natural remanent magnetization (NRM) is TRM acquired when the rock was cooled from temperature above the Curie temperature (580° C for magnetite), and (2) the amplitude of the TRM is proportional to the field intensity. Therefore, the paleointensity is expressed as

$$H_{paleo} = H_{lab} \times \frac{NRM}{TRM_{lab}} \quad (1)$$

where H_{paleo} is the paleointensity, H_{lab} is the field strength in the lab heating,

TRM_{lab} is the acquired TRM in lab heating (e.g. Dunlop and Öunlop , 1997). However, some portion of the NRM in natural samples is often overprinted by thermal events after the acquisition of initial TRM, or by chemical alternation. In paleointensity methods, NRM is resolved in means of blocking temperature by means of stepwise thermal demagnetization (ThD, series of the Thellier methods, Thellier and Thellier, 1959) or coercivity by means of alternating field demagnetization (AFD, series of the Shaw methods, Shaw, 1974).

To get reliable paleointensity data, it is important to select samples with minimal alternation and which can possess a stable remanence for a long period. The stability of remanence depends on both composition and grain size of the magnetic minerals present. Magnetite (titanomagnetite) with low titanium content is the best-studied magnetic mineral, and on which most techniques are focused. Similarly, the grain size of the magnetic mineral has a critical influence on the remanence stability due to the magnetic domain state (Dunlop and Özdemir, 1997). In large grains in the multi domain (MD) state, the magnetic structure within the grain is broken into several domains to minimize the exchange interaction and magnetostatic energies. Since the domain wall, the boundary between magnetic domains, can move easily by the application of an external field, MD grains cannot possess a stable remanence. Small grains in the single domain (SD) state which do not have domain walls inside is good media for recording the magnetic information. Grains with medium size are in the pseudo-single domain (PSD) state which exhibit intermediate features of SD and MD states, presumably bound by magnetic vortex states that behave like single-domains on geological time

scales. The upper bound of the grain size of SD domain for magnetite is ~0.1 μm for isotropic shaped grains but extends of several micro meters in elongated grains.

Published paleomagnetic results have been compiled in databases such as PINT (Biggin et al., 2009) and MagIC (EarthRef.org). Paleointensity results compiled in the PINT database are shown in Fig. 1. However, it is challenging to get a solid curve of paleointensity as a function of time covering the whole history of the Earth because of (1) difficulties in judging the qualities of each datum and selecting appropriate data, (2) too sparse data in the Precambrian era, and (3) the short timescale geomagnetic variations which hide long-term trends. For the purpose of achieving a reliable paleointensity curve of long-term variation, a brand new dataset using appropriate samples and measurement methods is required.

Single silicate crystals with magnetic inclusions have the potential to yield reliable paleointensity data since they are more resistant to alternation such as weathering and thermochemical alteration during laboratory heating. The host silicate protects the magnetic minerals, and fresh samples can be collected in quarries or from drill core using non-magnetic coring tools. Using single crystals, it could be possible to obtain results from samples which could not otherwise pass the conventional whole-rock measurements.

Zircon crystals have been used for paleointensity studies of the oldest ages owing to its permanence against chemical alternation and ability to obtain direct radiometric ages on them (Tarduno et al., 2014; 2015), although these claims are without controversy (Weiss et al., 2015). Tarduno et al. (2015)

claimed to determine a paleointensity recorded in a detrital zircon from the Jack Hills, Australia, which was as old as ~4.2 Ga, a claim that is also disputed. Nevertheless, detailed rock-magnetic properties of zircons collected from river sand in the Tanzawa pluton, Japan, showed its adequacy for paleointensity measurements (Sato et al., 2015). Recently, Fu et al. (2017) demonstrated that the absolute value of zircon paleointensity was consistent with the bulk rock using the Bishop Tuff of Northeastern California. Quartz phenocrysts are also a target studied for Archean rocks (Tarduno et al., 2007; 2010; 2014). Paleointensity and rock-magnetic properties of single plagioclase crystals have also been intensively studied. For lava samples, both paleointensity and paleodirection have been compared with the whole-rock, with good agreement (Cottrell and Tarduno, 1999; 2000). Plagioclase crystals separated from lava have been used for studies on paleointensity variation related to the reversal frequency of the dipole field (Tarduno et al., 2001; 2006; Tarduno and Cottrell, 2005; Cottrell et al., 2008). Rock-magnetic properties of plagioclase separated from plutonic rocks such as granitoids (Usui et al., 2015) and gabbros (Feinberg et al., 2005; Muxworthy and Evans, 2012) have also been reported. Some of them are characterized by needle-shaped tiny magnetite inclusions possibly formed by exsolution from the host plagioclase (Feinberg et al., 2005; Usui et al., 2015; Wenk et al., 2011). Plagioclase with exsolved magnetite is potentially an excellent recording medium of the ancient field, but should be treated carefully because anisotropy caused by needle-shaped magnetite can affect the results (Paterson, 2013; Usui et al., 2015). Paleomagnetic studies on pyroxene (Feinberg et al., 2005), microcline

(Tarduno et al., 2007) and olivine (Tarduno et al., 2012; Fu et al., 2014) have also been reported. Previous studies on single crystal paleomagnetism are summarized in Table 1. All of the paleointensity measurements introduced here was using the Thellier method.

To focus on the long-term variations of the geomagnetic field, plutonic rocks could be appropriate samples since they are likely to record the time-averaged field accurately during their long cooling history. Especially, granitic rocks, which have continuous record of preserved bodies over geological time, could be good targets to reveal the evolution of the geomagnetic. However, the paleomagnetic study of granitic rocks is often difficult due to weathering of the sample and the effects of coarse grain multi-domain (MD) magnetite. Also, many granitic rocks include biotite and pyrrhotite which easily decompose under heating and generate magnetite. To avoid these difficulties, it would be effective to separate single silicate crystals which contain magnetic minerals as inclusions from the rock samples, and use them for paleomagnetic measurements.

Despite its potential for establishing the long-term paleointensity, systematic rock-magnetic studies and paleointensity results on single crystal samples compared with the host granitic rock have not been reported. To qualify paleomagnetic measurements of single silicate crystals separated from granitic rocks relative to the conventional whole-rock methods, paleointensity and rock-magnetic properties of single crystals should be systematically studied and compared to those of the host granitic rock. Here we report the rock magnetic properties of zircon, quartz and plagioclase

separated from a well-studied granite sample which is the Cretaceous Iritono granite from northeast Japan. As a result, we found that plagioclase was the most appropriate for paleointensity measurements in the studied rock. Therefore, paleointensity experiments on plagioclase were conducted and the results were compared with prior results from the host granitic rock.

Iritono granite was chosen because its age corresponds to the middle stage of the Cretaceous Normal Superchron (CNS) in which the polarity reversal had been stopped for a period as long as 40 Myr. The occurrence of long superchrons are the most distinctive feature of the ~10 Myr scale trend of the geomagnetic field and are very possibly related to the activity of mantle plumes (e.g. Larson and Olson, 1991; Glatzmaier et al., 1999; Courtillot and Olson, 2007). Understanding the geomagnetic field intensity during superchrons are crucial to reveal the nature of the long-term change of the geodynamo and mantle controlling role on it.

We reconfirmed that the time-averaged geomagnetic paleointensity the middle stage of CNS was stronger than that of ages when frequent reversals occur (Tsunakawa et al. 2009), supporting the anticorrelation of reversal frequency and the field intensity, suggested from numerical dynamo simulations (e.g. Courtillot and Olson, 2007). Finally, we studied the rock-magnetic properties of plagioclase crystals separated from 22 granite samples, and proposed a possible guideline for sample selection in the future.

§2. Paleomagnetic studies on single crystals separated from the middle Cretaceous Iritono granite

§2-1. Sample description

We studied zircon, quartz and plagioclase separated from the middle Cretaceous Iritono granite in the Abukuma massif, northeast Japan (Fig. 2). Rock- and paleomagnetic studies and paleointensity measurements on the whole-rock samples are already reported by Wakabayashi et al. (2006) and Tsunakawa et al. (2009). Cooling history of the Iritono granite is also constrained by the previous studies using thermal diffusion model of the granite body and two radiometric age determination with different closure temperatures. The U-Pb zircon age is 115.7±1.9 Ma and ^{40}Ar-^{39}Ar biotite age is 101.9±0.2 Ma. The estimated cooling time is $4*10^4$ to $1.4*10^7$. The magnetic minerals in the Iritono granite are single-domain (SD) magnetite and pyrrhotite, and their fraction varied by sampling locations. Samples from site ITG09 showed the least contribution of pyrrhotite, and the primary magnetization was clearly distinguished from the secondary magnetization carried by low Bc-Tb components in terms of NRM direction. Hence, these sample were used for paleointensity experiments. We used the sister samples from site ITG09 (here referred as TN09) for the present studies. Tsunakawa et al. (2009) studied the paleointensity by both the Coe's version of Thellier method and the Tsunakawa-Shaw method. Results obtained by two methods were indistinguishable at the 2σ level. The reported paleointensity was 58.4±7.3 μT before applying the cooling rate correction, and 39.0±4.9 μT after correction. This corresponds to a virtual dipole moment (VDM) of $9.1±1.1*10^{22}$ Am^2. They concluded that the averaged geomagnetic field intensity during middle CNS was relatively strong compared to that of mixed polarity

intervals.

§2-2. Experimental methods

§2-2-1. Sample preparation

An 1-inch core granite sample was crushed with a non-magnetic mortar and pestle, and sorted by 850 μm and 350 μm mesh screens. Heavy fractions of the sample smaller than 350 μm were concentrated by an aqueous panning technique. Zircons with no visible cracks or opaque particles on the surface were hand-picked under a binocular stereoscopic microscope. Quartz and plagioclase were hand-picked from samples larger than 350 μm and smaller than 850 μm.

The selected crystals were leached by hydrochloric acid (HCl) to remove any tiny magnetic particles on the sample surface. HCl concentration and leaching duration was 12N and 4 days for zircon and quartz, and 6N and 8 hours for plagioclase, respectively. Samples were then sandwiched individually between layers of magnetically clean Scotch Magic Transparent Tape for measurement of their natural remanent magnetization (NRM) (Sato et al., 2015). This sandwiched-by-tape configuration was also useful for isothermal remanent magnetization (IRM) measurements, low temperature magnetometric experiments and hysteresis measurements. All magnetic experiments were conducted at the Center for Advanced Marine Core Research, Kochi University (CMCR).

§2-2-2. Remanence measurements by SQUID magnetometer

A SQUID moment magnetometer (2G Enterprises, model 755) was used for remanence measurements. We used the sample holder made of acrylonitrile butadiene styrene (ABS) that was designed and used for single crystal measurements by Sato et al. (2015). Single crystal samples sandwiched by tape or held by a glass holder (described below) were fixed on the edge of the ABS holder by double stick tape. The magnetic moments of the ABS holder and double stick tape were measured before and after sample measurement and subtracted from the sample moment. First, we measured the NRM intensity of several hundred grains for each mineral to obtain the NRM intensity distribution, and to select samples with significant magnetization to do further measurements. The detection limit of the SQUID magnetometer was $2*10^{-12}$ Am^2, so we employed $4*10^{-12}$ Am^2 as a threshold to distinguish significant NRM intensity from noise.

§2-2-3. Low-temperature magnetometric experiments, hysteresis loop and IRM measurements

For selected samples that showed significant NRM intensity, we conducted low-temperature remanence measurements using the MPMS-XL5 Magnetic property Measurement System (MPMS, Quantum Design) to understand the magnetic carrier of each mineral, following the technique of Moskowitz et al. (1993). IRM was imparted at 2.5 T and 10 K after zero-field cooling from 300 K. Remanence was measured during warming in zero-field (ZFC remanence). Subsequently, sample was cooled to 10 K in 2.5 T field and then remanence was measured during warming in zero-field (FC remanence).

Day plots (Day et al., 1977) are a simple method to investigate the domain state (nearly equal to the grain size) of magnetic minerals based on hysteresis parameters such as the saturation magnetization (Ms), remanent saturation magnetization (Mr), coercivity (Bc) and remanent coercivity (Brc). Hysteresis loop measurements were therefore carried out for plagioclase grains and a quartz grain which contained magnetite as the magnetic carrier using the MicroMag 2900 Alternating Gradient Magnetometer (Lake Shore). Samples sandwiched by tape were mounted on a P1 AGM transducer probe with a silica sample stage (Princeton Measurements Corporation). The blank saturation magnetization of the probe was $5.8*10^{-10}$ Am^2. Maximum field during hysteresis loop measurement was 0.5 T and the field increment was 4 mT. Diamagnetic/paramagnetic corrections were applied to the obtained hysteresis loop by subtracting the average slopes at applied field of $|B| > 300$ mT.

An IRM was imparted to 75 plagioclase samples at 2 T by the pulse magnetizer (MMPM10, MagneticMeas.) along the Z axis of the samples.

§2-2-4. Stepwise thermal demagnetization and paleointensity experiments

For stepwise thermal demagnetization (ThD) and paleointensity experiments, we made new thermally-resistant holders for single crystal samples like that which was originally designed for SQUID microscope measurements by Fu et al. (2017). Non- alkali high-temperature glass plates (Eagle XG, Corning, 1.1 mm thick) were cut into squares of 7 mm on a side. A 1 mm diameter pit was drilled in the center of the glass plate, followed by

intense cleaning in concentrated HCl. A single crystal sample was put into the pit and fixed by stuffing hyperfine-grained SiO_2 powder (~0.8 μm) (Fig. 3). This technique enabled us to conduct oriented heating experiments on single crystals. The blank magnetic moment of the glass holder after subtracting the moment of ABS holder and double stick tape was well below the practical detection limit of the SQUID magnetometer (Fig. 4).

We performed paleointensity measurements with the Tsunakawa-Shaw method (Tsunakawa and Shaw, 1994; Yamamoto et al., 2003; Mochizuki et al., 2004; Yamamoto and Tsunakawa, 2005; Yamamoto et al., 2015) on 17 plagioclase grains. In this method, samples are subjected to low-temperature demagnetization (LTD) and heated twice. Stepwise alternating field demagnetization (AFD) of anhysteretic remanent magnetization (ARM) was performed before and after heating to make correction for sample alternation due to heating. Validity of the ARM corrections were checked by the second heating (see Yamamoto and Tsunakawa (2005) for detailed theory and measurement protocol). LTD treatment was conducted by cooling a sample in a Dewar bottle inside a triple magnetically-shielded case filled with liquid nitrogen for 5 minutes. Thermoremanent magnetization (TRM) was given by cooling from 610° C and in a 50 μT field in a vacuum. The heating duration was 10 minutes for the first heating and 20 minutes for the second, with a cooling rate of approximately 10° C per minute for both. AFD and ARM impartment was carried out using a DEM-95C alternating field demagnetizer (Natsuhara Giken). ARM was imparted at DC field 50 μT, with a peak AC field of 180 mT. For samples 9004, 9009, 9013 and 9016, TRM was imparted

in the likely direction of the characteristic remanent magnetization (ChRM), estimated from the orthogonal plot of AFD of the NRM. For other samples, TRM was imparted along the Y axis. In this study, AFD steps for ARM without LTD treatment (ARM00, ARM10, and ARM20) were omitted.

§2-2-5. ARM anisotropy

Magnetic remanence anisotropy of single plagioclase crystals could be surprisingly large due to the presence of elongated magnetite grains aligned with the crystallographic planes of the host mineral (Usui and Nakamura, 2009; Usui et al. 2015). A large magnetic remanence anisotropy can adversely affect the paleointensity results (Veitch et al., 1984; Selkin et al., 2000; Paterson, 2013). To assess the anisotropy effect, we measured the ARM anisotropy of 19 plagioclase samples (13 samples during paleointensity measurements and 6 additional samples). ARM was imparted along three orthogonal axes (ARM_x, ARM_y, and ARM_z) to obtain the remanence anisotropy tensor. Each ARM was measured after LTD treatment. ARM anisotropy of whole-rock samples were measured using a Natsuhara Giken™ spinner magnetometer.

§2-3. Results

§2-3-1. NRM intensity distribution of zircon, quartz and plagioclase

We first measured the NRM intensity of several hundred grains of each mineral. NRM intensity histograms that were obtained are shown in Fig. 5. Very few samples of zircon and quartz had NRM intensities larger than the

threshold. The distribution of NRM intensities below the threshold are similar in zircon and quartz, which we interpret as the noise of the instrument. It also indicates that the NRM of the Scotch Magic Transparent Tape was also well below the detection threshold. In contrast, more than 70 % of plagioclase samples exceeded the threshold. The discrepancy in NRM intensity distribution of plagioclase and other minerals implies a difference in the mechanism by which the magnetic inclusions were incorporated.

§2-3-2. Zircon

Low-temperature magnetometry and stepwise ThD measurements of NRM were performed on selected samples that had significant NRM intensity. Representative results are summarized in Fig. 6. Low-T experiments were performed on five samples. One sample showed a significant decrease of remanence at ~30 K which could be interpreted as the magnetic phase transition of pyrrhotite (Fig. 6a), while the other four samples did not show any obvious transition (Fig. 6b). Then, stepwise ThD were performed on four different samples. Two samples showed a characteristic magnetization component and pyrrhotite-like blocking temperature (Fig. 6c), but the other two did not show any stable magnetic component (Fig. 6d). We concluded that the dominant magnetic inclusion in zircon is pyrrhotite and therefore zircon in the studied granite sample is not appropriate for paleointensity measurements.

§2-3-3. Quartz

We performed stepwise ThD measurements of NRM for two quartz grains. In both samples, magnetization decreased toward the origin in the orthogonal plot. From the blocking temperature, one sample contained magnetite (Fig. 7c) and the other contained pyrrhotite (Fig. 7d). For the sample that contained magnetite, we performed low-temperature magnetometry measurements (Fig. 7a) and hysteresis loop measurements (Fig. 7b and Fig. 8d for the Day plot) to constrain the composition and grain size of magnetite inclusions. Results indicate that the magnetite inclusion is in SD-PSD state and nearly pure (low titanium). We concluded that quartz is a potential sample for paleointensity measurements but not practical because of the rarity of magnetite bearing samples.

§2-3-4. Plagioclase

§2-3-4-1. Rock-magnetic properties

Fig. 8a shows the NRM intensity plotted as a function of IRM intensity for the 75 plagioclase grains we measured. The NRM/IRM ratio for most of the samples was close to 0.1 (Fig. 8b). This indicates that the magnetic carrier and the origin of NRM are identical among plagioclase grains, and it most likely is a TRM (Fuller et al. 2002). Sato et al. (2015) reported that the distribution on the NRM/IRM plot could be useful to predict the species and grain size of the magnetic carrier of a specimen based on Yu (2010), who reported that TRM/SIRM ratios depend on the grain size of the magnetic mineral. NRM/IRM=0.1 could be interpreted as TRM imparted at ~50 μT to magnetite grain size ~0.1 μm (note that the whole-rock paleointensity was

58.4 μT).

We performed magnetic hysteresis (Fig.8c, d) and low-temperature magnetometry (Fig. 8e) measurements on four selected grains with different NRM/IRM ratio. All of the four samples exhibited similar features in both hysteresis and low-temperature magnetization. Results on the hysteresis measurements fall in the PSD region of the Day plot (Fig. 8d). The Verwey transition of magnetite was clearly observed at 120 K, indicating a very low titanium content of magnetite, and the larger remanence in FC relative to ZFC suggests a dominance of SD material (Fig. 8e). We conclude that the magnetic carrier in the plagioclase was nearly pure magnetite in the SD-PSD state. After paleointensity measurements, hysteresis measurements on four samples and low-temperature measurements on one sample were conducted. The results were similar to those showed in Figs. 8c and e, which implies that heating during paleointensity measurements did not severely affect the magnetic characteristics of plagioclase grains. The blocking temperature distribution was investigated on four samples after paleointensity measurements by stepwise ThD of a TRM given at 50 μT. Results were compared to the whole-rock stepwise ThD of NRM reported by Wakabayashi et al. (2006) (Fig. 8f). The blocking temperature distribution of all four plagioclase samples and the whole-rock were similar to each other except for a slight decrease of remanence between 300 and 550° C in the whole-rock which could be related to trace pyrrhotite.

To assess the anisotropy effect on paleointensity and examine the variation in anisotropy degree and shape, ARM anisotropy was studied for 19

plagioclase samples including 13 of the samples used in paleointensity measurements. The ARM anisotropy tensor was estimated from the measured ARM_x, ARM_y, and ARM_z. Eigenvalues and anisotropy parameters, anisotropy degree P (Nagata, 1961), corrected anisotropy degree P_j, and shape factor T_j (Jelinek, 1981) were calculated (Table 2). Positive and negative values of T_j indicate that the shape of the anisotropy ellipsoids are oblate and prolate, respectively. Fig. 8g is the Jelinek diagram which shows the variation of P_j and T_j. In contrast to Usui et al. (2015) who measured the ARM anisotropy of single plagioclase crystal samples separated from a Paleoarchean granitoid, the degree of anisotropy was relatively small and the shape of anisotropy varied from oblate to prolate.

§2-3-4-2. Paleointensity experiments by the Tsunakawa-Shaw method

We conducted Tsunakawa-Shaw paleointensity experiments on 17 plagioclase grains. In consideration of the sensitivity of the instrument, samples with NRM intensities larger than $5*10^{-11}$ Am^2 were chosen for paleointensity measurements. Taking the weak remanence of single crystal samples into account, we employed a different selection criteria to the original Tsunakawa-Shaw method applied for volcanic rocks. The new criteria are:

1. A primary component found in the orthogonal plot of NRM demagnetization

2. f>0.3 in the NRM/TRM1* plot

3. R>0.90 in the NRM/TRM1* plot

4. Slope of the TRM1/TRM2* plot within 1+-0.1.

5. R>0.95 in the TRM1/ TRM2* plot

where f is the NRM fraction of the primary component and R is the correlation coefficients. Primary components were identified by eye on the orthogonal plot, and corresponded to MAD values < 10˚. By low-temperature treatment, 5-15 % of the NRM was demagnetized. This rate corresponds to the fraction of unstable MD components in the samples. According to the new criteria, 9 out of 17 samples were selected. Two samples were rejected by criteria 1 or 3. Six samples were rejected due to discrepancy of the slope in TRM1/RM2* plot from 1 (criteria 4). Typical examples of successful and failed samples are presented in Figs 9 and 10. Results of all 17 samples are summarized in Table 3. The obtained plagioclase paleointensity was 57.4±11.8 μT. Fig. 11 shows the summary of plagioclase paleointensity compared with the whole-rock paleointensity. The mean value of paleointensity was in good agreement to the previously reported whole-rock measurement (58.4±7.3 μT). Therefore, we concluded that an assembly of single plagioclase crystals can possess paleointensity information similar to the host-rock. We note that the deviation of plagioclase paleointensity was considerably larger than the whole-rock paleointensity.

§2-4. Features and origin of magnetic inclusion in plagioclase

Fig. 12 is a microscopic image of a polished plagioclase sample (sample no. 68 in Table 2). Magnetite crystals are the tiny black dots with rounded to needle-like shapes that are uniformly distributed in the host plagioclase, and show no association with cracks. This implies that the magnetites were not

generated by secondary alternation but rather have a primary origin such as incorporation during plagioclase crystallization or exsolution at subsolidus conditions. Furthermore, the needle-like shape of magnetite and their preferred alignment relative to the feldspar suggests an origin via exsolution; magnetite, a cubic inverse spinel, typically forms equant octahedral crystals when crystallizing from a magma.

The needle-like magnetite grains found in Fig. 12 could be categorized to SD state due to particle length (few micron) and width/length ratio (<0.1) (Dunlop and Özdemir, 1997). Also, they can cause strong shape magnetic anisotropy. These configurations are qualitatively consistent with the magnetic properties. On the other hand, rounded shaped magnetite grains are possibly in the MD state. Further investigations such as SEM analysis are required for detailed comparison with rock-magnetic features and understanding of the origin of the magnetite inclusions.

§2-5. Discussion

§2-5-1. Comparison with the whole-rock

In the whole-rock measurements, NRM was carried by two components: an 'H' component characterized by high coercivity (>50-90 mT) or high blocking temperature (>350-560 ˚C), and an 'L' component characterized by low coercivity or low blocking temperatures (Wakabayashi et al., 2006). Wakabayashi et al. (2006) argued that the H component was carried by magnetite and the L component was mainly carried by pyrrhotite. Two components were separated by a 13˚ difference in the inclination,

implying that a geothermal event at low temperatures occurred after the primary magnetization was achieved. In plagioclase samples, the L component was not always found. This could be explained by the difference in magnetic mineral components such as lack of secondary pyrrhotite in plagioclase.

Fig. 13 shows NRM directions of plagioclase samples are plotted in equal-area projection where the x, y, and z axis are transformed to the directions of the maximum, medium and minimum eigenvectors of the anisotropy tensors. Although the concentration in the center indicates gravitation toward the easy axis, the NRM direction is random. That is to say that the plagioclase grains were randomly oriented in the host rock. The randomness of plagioclase orientation is also supported by the isotropy of whole-rock samples (Table 4).

We made a rough estimate of the NRM fraction of the whole-rock carried by magnetite inclusions in plagioclase. We found that most of the stable remanence of the whole-rock sample was carried by plagioclase, as predicted by Wakabayashi et al. (2006) and Tsunakawa et al. (2009). Since the whole-rock sample was isotropic, whole-rock measurements could be interpreted as averaging tens of thousands of plagioclase crystals with random crystallographic directions which give smaller deviation in paleointensity results compared to the single crystal technique.

§2-5-2. Cooling time effect on paleointensity

The extremely slow cooling of granitic rocks compared to laboratory

timescales could cause overestimation of paleointensity due to the time dependence of the acquisition of TRM (Halgedahl et al., 1980; Selkin et al., 2000; Yu, 2011). Based on the estimated cooling time of the Iritono granite body, Tsunakawa et al. (2009) argued that the ratio of TRM in nature to TRM in laboratory would be 1.5 assuming the primary component was carried by SD magnetite.

Results on magnetic hysteresis measurements of plagioclase grains are plotted in the PSD region on the Day plot on the trend of SD-MD mixture suggested by Channell and McCabe (1994) and Parry (1982) (Fig. 8d). Considering the 5-15 % reduction of NRM by LTD, the Day plot can be interpreted as a mixture of SD and MD. Therefore, it is reasonable to assume that the stable remanence that is involved in paleointensity measurements was mainly carried by SD state magnetite, similar to the assumption of Tsunakawa et al. (2009). As a conclusion, the corrected plagioclase paleointensity is 38.2±7.9 μT.

§2-5-3. Possible effects of magnetic anisotropy

We found that the dispersion of the paleointensity value of single plagioclase grains was relatively larger than that of the whole-rock samples. In general, variability of the paleointensity estimates could be caused by experimental noise and non-ideal behavior of the magnetic carrier such NRM with non-thermal origin, presence of large magnetic grains, chemical alternation in nature or due to laboratory heating, magnetic anisotropy, and possibly non-linear remanence acquisition (Paterson et al., 2012).

Additionally, the possibility of recording the secular variation of the field intensity by different blocking timings for each grain cannot be excluded when studying single crystals separated from a slow-cooled sample, even in a time with no reversals. For the case of single plagioclase grains that are characterized by elongated magnetite inclusions, magnetic anisotropy could be especially important. In samples with large anisotropy, the measured paleointensity values could be either larger or smaller than the true value depending on angles between the major or minor anisotropy axes and the ancient or laboratory field (Paterson, 2013). This anisotropy effect could be corrected by applying the inverted anisotropy tensor to the magnetic remanence vectors during paleointensity measurement (Veitch et al., 1984; Selkin et al., 2000; Paterson, 2013). Hence, we used the ARM anisotropy tensor as a proxy for TRM anisotropy tensor. TRM anisotropy tensor was checked after paleointensity experiments for some samples and the consistency with the ARM anisotropy tensor was confirmed. Also, the ARM anisotropy after AFD at 50 mT was checked. Typical results of analysis on anisotropy directions and anisotropy parameters are shown in Fig. 15. The directions of the anisotropy axes are identical for ARM and TRM, and do not change by AFD. However, the anisotropy degree P and corrected anisotropy P_j increased after AFD.

Anisotropy correction was performed on 13 samples (Fig. 16). The results show that both the errors and dispersion of the sample directions got larger after anisotropy correction. We concluded that anisotropy correction was not effective for the studied sample. Paterson (2013) argued that this

correction would not be effective when the anisotropy degree P exceed ~ 3. In this study, P of several samples could be too large for the inverted tensor correction to be effective.

Instead of correcting the anisotropy effect with the inverse matrix, we followed the recommendation of Usui et al. (2015) to average over a number of samples to get rid of anisotropy effect. The validity of averaging can be checked by considering a virtual paleointensity:

$$r=ARM_0/ARM_y \qquad (2),$$

by regarding ARM_0 and ARM_y as proxies of NRM and laboratory TRM, respectively. In our paleointensity experiments, ARM_0 and ARM_y was imparted by DC files $\mathbf{H_{NRM}}$ and $\mathbf{H_y}$, whose directions were approximately parallel to the direction of ChRM and parallel to the y axis of the sample frame, respectively, which are both randomly distributed with respect to the anisotropy axes. Since the strength of $\mathbf{H_{NRM}}$ and $\mathbf{H_y}$ was the same (50 μT), the r value is 1 when the sample is isotropic. If the anisotropy bias on paleointensity is cancelled out by averaging samples, the average of r is one. Our results exhibit average r as 1.11 with 95 % confidence of ±0.15 (Table 3). Therefore, we conclude that cancelling of the anisotropy effect is moderately effective. Usui et al. (2015) argued that simple arithmetic average could overestimate the true paleointensity, and a geometric average should be used instead. However, the geometric average of our results was 1.10 so that the difference between two averages are insignificant, possibly because of relatively small degree of anisotropy.

Based on simulated paleointensity experiments, Usui et al. (2015)

demonstrated that averaging few tens of plagioclase crystals is required to reduce the paleointensity bias below 30 % when considering the case of eigenvalues (w_1, w_2, w_3)=(2.22, 1.23, 0.37), which corresponds to P_j=6.21. Since the mean P_j for the studied samples was smaller (P_j=3.25), nine samples could be sufficient to obtain a reliable value.

§2-5-4. Application of Tsunakawa-Shaw paleointensity experiments of single plagioclase crystals to the long-term behavior of the geomagnetic field

Our calculated Virtual Dipole Moment (VDM) from single-crystal plagioclase paleointensity measurements is $8.9\pm1.8*10^{22}$ Am^2, which is comparable to the whole-rock data but significantly higher than the average VDM for 0-5 Ma ($3.6\pm2.1*10^{22}$ Am^2; Yamamoto and Tsunakawa, 2005). In other words, the ±20 % error of the present study is small enough to distinguish the strong field intensity during the Cretaceous superchron compared to that of typical era of mixed polarity. The significance of strong geomagnetic field intensity at the time of superchrons are discussed in Chapter 5.

Fig. 14 compares our result with previous reports on gabbro (Granot et al., 2007) and plagioclase separated from lava (Tarduno et al., 2001; 2002; Tarduno and Cottrell, 2005). Our new result shows an intermediate value between the previous studies. This could be a result of the slower the cooling of the Iritono granite (104 to 107 years) compared to lavas (perhaps < a day) and gabbros (105 years), providing a longer-term estimate of average paleointensity.

Paleointensity measurements on single silicate crystals have been only carried out by the Thellier method thus far. To our knowledge, the present study is the first report that has applied the Shaw-type paleointensity measurements to single crystal samples. Since the blocking temperature of the plagioclase samples was concentrated in a narrow range near the Curie temperature of magnetite (Fig. 8f), Shaw-type measurements which resolve the remanence by coercivity could be more sensitive than the Thellier method that uses the blocking temperature spectrum. This difference might be important in single crystal paleointensity studies because of their weak remanence close to the sensitivity limit of the magnetometer.

§3. Sample selection guidelines for plagioclase paleointensity

For further investigation of the CNS, it is essential to get paleointensity data from granites formed in various ages covering before, during and after the CNS. To find granite samples that have plagioclase suitable for paleointensity measurements, we conducted magnetic hysteresis measurements and low-temperature magnetometry measurements on total 29 plagioclase samples from 22 granitic rocks. Samples are mainly selected from granitic bodies whose ages are 100 to 5 Ma in Japan. Additionally, some samples from older terranes overseas (Ireland, 0.4 Ga; India, 2.6 Ga; Australia, 3.3 Ga) were also studied. Samples are listed in Table 5, and the Day plot are shown in Fig. 17. Based on the B_{rc}/B_c ratio, two, eleven and sixteen samples were in SD, PSD and MD states, respectively. An aggregate of about 20 plagioclase grains from the Iritono granite (TN09-44) studied in

section 2-2 is plotted as a reference. The Day plots indicate a wide distribution on the magnetic domain state. Low-temperature magnetometry experiments were carried out on nine selected samples (Fig. 18). Evidence of SD to PSD magnetite inclusions were found in samples 05042803, ECHIZEN02_02, 07042804_red and IR374_red. Nearly pure magnetite was only found in TN09-44.

From the present results, we found that magnetite is not the dominant magnetic carrier in samples in the ilmenite series. Additionally, there seems to be a tendency that samples of high susceptibility are categorized in the MD state, which is consistent with the higher susceptibility produced by the motion of domain walls. Therefore, to find plagioclase with fine-grained magnetite inclusions, the best target would be granitic samples in the magnetite series but with relatively low susceptibility.

Ilmenite series granites are characterized by low $\delta^{34}S$ which suggests that magma mixed with sediments containing biogenic sulfur (e.g. Sasaki and Ishihara, 1979), whereas magnetite series granites probably originate in the upper mantle or the lowest crust, and have not mixed with surface materials (Ishihara, 1977). These genesis processes are consistent with the distribution of ilmenite and magnetite series granites, with the former generally being emplaced along the ocean side and the later along the marginal sea. In Japan, magnetite series granites are mainly distributed in the San-in belt and northeast Honshu (Ishihara, 1977). To get desirable samples for paleointensity experiments, field sampling on these areas should be conducted. Wakabayashi et al. (2006) and Tsunakawa et al. (2009) revealed

that the magnetic properties of granitic rocks can vary within single granitic bodies over the space of just a few meters in distance. Hence, we recommend sampling on multiple sites at a locality, and selecting the best sites by rock-magnetic measurements on the pilot samples, we note that the magnetic mineral constitution of the plagioclase samples can be much simpler than those of the host whole-rock samples, which would make paleomagnetic investigations easier. Additionally, a number of single crystal samples can be obtained from a small fragment of a granitic rock, and therefore, a reliable result can be achieved by averaging multiple samples. These merits of single crystals would be particularly significant for paleointensity experiments on granitic rocks that suffer from interference of pyrrhotite, and have small-scale heterogeneity in their magnetic properties, thus making it difficult to obtain sufficient quantities for whole-rock experimentation.

§4. Conclusion

We have evaluated the utility of using single silicate crystals separated from granitic rocks in the exploration the long-term evolution of the intensity of the geomagnetic field. We studied the rock-magnetic properties of zircon, quartz and plagioclase separated from the Iritono granite whose paleointensity was already well constrained by past studies. In the studied samples we found that plagioclase was the most suitable mineral phase to study, which was more reliably and stably magnetic than other minerals like zircon or quartz. We conducted paleointensity measurements on 17 plagioclase samples using the Tsunakawa-Shaw method. Nine samples were

successful and gave mean paleointensity values before and after cooling time correction of 57.4±11.8 μT and 38.2 ± 7.9 μT, respectively. This value is consistent with the previously reported whole-rock paleointensity, suggesting relatively strong field intensity during the CNS. Therefore, we concluded that an assembly of single plagioclase crystals separated from a granitic rock has the ability to yield the same paleointensity information as the host whole-rock. By applying the present paleointensity method to various granitic rocks from different ages, advanced understanding of the long-term behavior of the geomagnetic field is expected without the complications of large MD magnetites that often compromise such work.

Reference

Aubert, J., Tarduno, J. A., Johnson, C. L. (2010). Observations and models of the long-term evolution of Earth's magnetic field. Space science reviews, 155(1-4), 337-370. doi: 10.1007/s11214-010-9684-5

Biggin, A. J., Piispa, E. J., Pesonen, L. J., Holme, R., Paterson, G. A., Veikkolainen, T., Tauxe, L. (2015). Palaeomagnetic field intensity variations suggest Mesoproterozoic inner-core nucleation. Nature, 526(7572), 245-248. doi: 10.1038/nature15523

Biggin, A. J., Strik, G. H., Langereis, C. G. (2009). The intensity of the geomagnetic field in the late-Archaean: new measurements and an analysis of the updated IAGA palaeointensity database. Earth, planets and space, 61(1), 9-22. doi: 10.1186/BF03352881

Channell, J. E. T., McCabe, C. (1994). Comparison of magnetic hysteresis parameters of unremagnetized and remagnetized limestones. Journal of Geophysical Research: Solid Earth, 99(B3), 4613-4623. doi: 10.1029/93JB02578

Cottrell, R. D., Tarduno, J. A. (1999). Geomagnetic paleointensity derived from single plagioclase crystals. Earth and Planetary Science Letters, 169(1), 1-5. doi: 10.1016/S0012-821X(99)00068-0

Cottrell, R. D., Tarduno, J. A. (2000). In search of high - fidelity geomagnetic paleointensities: A comparison of single plagioclase crystal and whole rock Thellier - Thellier analyses. Journal of Geophysical Research: Solid Earth, 105(B10), 23579-23594. doi: 10.1029/2000JB900219

Cottrell, R. D., Tarduno, J. A., Roberts, J. (2008). The Kiaman Reversed Polarity Superchron at Kiama: Toward a field strength estimate based on single silicate crystals. Physics of the Earth and Planetary Interiors, 169(1), 49-58. doi: 10.1016/j.pepi.2008.07.041

Courtillot, V., Olson, P. (2007). Mantle plumes link magnetic superchrons to

Phanerozoic mass depletion events. Earth and Planetary Science Letters, 260(3), 495-504. doi: 10.1016/j.epsl.2007.06.003

Day, R., Fuller, M., Schmidt, V. A. (1977). Hysteresis properties of titanomagnetites: grain-size and compositional dependence. Physics of the Earth and planetary interiors, 13(4), 260-267. doi: 10.1016/0031-9201(77)90108-X

Dunlop, D. J., Özdemir, Ö. (1997). Rock Magnetism - Fundamentals and frontiers, Cambridge University Press, Cambridge.

Feinberg, J. M., Scott, G. R., Renne, P. R., Wenk, H. R. (2005). Exsolved magnetite inclusions in silicates: Features determining their remanence behavior. Geology, 33(6), 513-516. doi: 10.1130/G21290.1

Fu, R. R., Weiss, B. P., Lima, E. A., Harrison, R. J., Bai, X. N., Desch, S. J., Ebel, D. S., Suavet, C., Wang, H., Glenn, D., Le Sage, D., Kasama, T., Walsworth, R. L., Kuan, A. T. (2014). Solar nebula magnetic fields recorded in the Semarkona meteorite. Science, 346(6213), 1089-1092. doi: 10.1126/science.1258022

Fu, R. R., Weiss, B. P., Lima, E. A., Kehayias, P., Araujo, J.F.D.F., Glenn, D.R., Gelb, J., Einsle, J.F. Bauer, A.M., Harrison, R.J., Ali, G.A.H., Walsworth, R.L., (2017). Evaluating the paleomagnetic potential of single zircon crystals using the Bishop Tuff. Earth and Planetary Science Letters, 458, 1-13. doi: 10.1016/j.epsl.2016.09.038

Fuller, M., T. Kidane, J. Ali. (2002). AF demagnetization characteristics of NRM, compared with anhysteretic and saturation isothermal remanence: an aid in the interpretation of NRM. Physics and Chemistry of the Earth 27, 1169–1177.

Gee, J. S., Kent, D. V. (2007). Source of oceanic magnetic anomalies and the geomagnetic polarity time scale. in Treatise on Geophysics, Vol. 5: Geomagnetism, 455-507.

Glatzmaier, G. A., Coe, R. S., Hongre, L., Roberts, P. H. (1999). The role of the Earth's mantle in controlling the frequency of geomagnetic reversals. Nature, 401(6756), 885-890. doi: 10.1038/44776

Granot, R., Tauxe, L., Gee, J. S., & Ron, H. (2007). A view into the Cretaceous geomagnetic field from analysis of gabbros and submarine glasses. Earth and Planetary Science Letters, 256(1), 1-11. doi: 10.1016/j.epsl.2006.12.028

Halgedahl, S. L., Day, R., Fuller, M. (1980). The effect of cooling rate on the intensity of weak - field TRM in single - domain magnetite. Journal of Geophysical Research: Solid Earth, 85(B7), 3690-3698. doi: 10.1029/JB085iB07p03690

Huston, D. L., Sun, S. S., Blewett, R., Hickman, A. H., Kranendonk, M. V., Phillips, D., Baker, D., Brauhart, C. (2002). The timing of mineralization in the Archean North Pilbara terrain, Western Australia. Economic Geology, 97(4), 733-755. doi: 10.2113/gsecongeo.97.4.733

Ishihara, S. (1977). The magnetite-series and ilmenite-series granitic rocks. Mining Geology, 27(145), 293-305. doi: 10.11456/shigenchishitsu1951.27.293

Ishihara, S., Hayasaka, Y., (2007). EPMA and SHRIMP dating of monazite and zircon from gneissose granites in the Daito area, Shimane Prefecture, Southwest Japan. Geological Society of Japan Abstract 2007, 319-319.

Jayananda, M., Chardon, D., Peucat, J.J., Capdevila, R., (2006). 2.61Ga potassic granites and crustal reworking in the western Dharwar craton, southern India: Tectonic, geochronologic and geochemical constraints. Precambrian Research 150, 1-26. doi: 10.1016/j.precamres.2006.05.004

Jelinek, V. (1981). Characterization of the magnetic fabric of rocks.

Tectonophysics, 79(3-4), T63-T67. doi: 10.1016/0040-1951(81)90110-4

Larson, R. L., Olson, P. (1991). Mantle plumes control magnetic reversal frequency. Earth and Planetary Science Letters, 107(3-4), 437-447. doi: 10.1016/0012-821X(91)90091-U

Mochizuki, N., Tsunakawa, H., Oishi, Y., Wakai, S., Wakabayashi, K. I., Yamamoto, Y. (2004). Palaeointensity study of the Oshima 1986 lava in Japan: implications for the reliability of the Thellier and LTD-DHT Shaw methods. Physics of the Earth and Planetary Interiors, 146(3), 395-416. doi: 10.1016/j.pepi.2004.02.007

Moskowitz, B. M., R. B. Frankel, and D. A. Bazylinski (1993), Rock magnetic criteria for the detection of biogenic magnetite, Earth Planet. Sci. Lett., 120, 283–300.

Muxworthy, A. R., Evans, M. E. (2012). Micromagnetics and magnetomineralogy of ultrafine magnetite inclusions in the Modipe Gabbro. Geochemistry, Geophysics, Geosystems, 14(4), 921-928. doi: 10.1029/2012GC004445

Nagata, T., (1961). Rock Magnetism, Maruzen, Tokyo.

O'Connor, P. J. (1989). Chemistry and Rb–Sr age of the Corvock granite, western Ireland. Geological Survey of Ireland Bulletin, 4, 99-105.

Parry, L. G. (1982). Magnetization of immobilized particle dispersions with two distinct particle sizes. Physics of the Earth and Planetary interiors, 28(3), 230-241. doi: 10.1016/0031-9201(82)90004-8

Paterson, G.A., Biggin, A.J., Yamamoto, Y. & Pan, Y., (2012). Towards the robust selection of Thellier-type paleointensity data: the influence of experimental noise, Geochem. Geophys. Geosyst., 13, Q05Z43, doi:10.1029/2012GC004046

Paterson, G. A. (2013). The effects of anisotropic and non-linear

thermoremanent magnetizations on Thellier-type paleointensity data. Geophysical Journal International, 193(2), 694-710. doi: 10.1093/gji/ggt033

Sasaki, A., Ishihara, S. (1979). Sulfur isotopic composition of the magnetite-series and ilmenite-series granitoids in Japan. Contributions to Mineralogy and Petrology, 68(2), 107-115. doi: 10.1007/BF00371893

Sato, M., Yamamoto, S., Yamamoto, Y., Okada, Y., Ohno, M., Tsunakawa, H., & Maruyama, S. (2015). Rock-magnetic properties of single zircon crystals sampled from the Tanzawa tonalitic pluton, central Japan. Earth, Planets and Space, 67(1), 150. doi: 10.1186/s40623-015-0317-9

Selkin, P. A., Gee, J. S., Tauxe, L., Meurer, W. P., Newell, A. J. (2000). The effect of remanence anisotropy on paleointensity estimates: a case study from the Archean Stillwater Complex. Earth and Planetary Science Letters, 183(3), 403-416. doi: 10.1016/S0012-821X(00)00292-2

Selkin, P.A., Gee, J.S. Tauxe, L., (2007). Nonlinear thermoremanence acquisition and implications for paleointensity data, Earth planet. Sci. Lett., 256, 81–89. doi: 10.1016/j.epsl.2007.01.017

Shaar, R., Ron, H., Tauxe, L., Kessel, R., Agnon, A., Ben-Yosef, E. Feinberg, J.M., (2010). Testing the accuracy of absolute intensity estimates of the ancient geomagnetic field using copper slag material, Earth planet. Sci. Lett., 290, 201–213. doi: 10.1016/j.epsl.2009.12.022

Shaw, J. (1974). A new method of determining the magnitude of the paleomagnetic field, Application to five historic lavas and five archaeological samples. Geophys. JR astr. Soc., 76, 637-651.

Shibata, K., Ishihara, S., (1974). K-Ar age of the biotites across the central part of Hiroshima granites. Geological Survey of Japan, Kawasaki, Kanagawa.

Takahashi, F., Tsunakawa, H., Matsushima, M., Mochizuki, N., Honkura, Y.

(2008). Effects of thermally heterogeneous structure in the lowermost mantle on the geomagnetic field strength. Earth and Planetary Science Letters, 272(3), 738-746. doi: 10.1016/j.epsl.2008.06.017

Tani, K., Dunkley, D. J., Kimura, J. I., Wysoczanski, R. J., Yamada, K., Tatsumi, Y. (2010). Syncollisional rapid granitic magma formation in an arc-arc collision zone: Evidence from the Tanzawa plutonic complex, Japan. Geology, 38(3), 215-218. doi: 10.1130/G30526.1

Tani, K., Horie, K., Dunkley, D., Ishihara, S. (2014). Pulsed granitic crust formation revealed by comprehensive SHRIMP zircon dating of the SW Japan granitoids. Geological Society of Japan Abstract 2014.

Tarduno, J. A., Blackman, E. G., Mamajek, E. E. (2014). Detecting the oldest geodynamo and attendant shielding from the solar wind: Implications for habitability. Physics of the Earth and Planetary Interiors, 233, 68-87. doi: 10.1016/j.pepi.2014.05.007

Tarduno, J. A., Cottrell, R. D., Smirnov, A. V. (2001). High geomagnetic intensity during the mid-Cretaceous from Thellier analyses of single plagioclase crystals. Science, 291(5509), 1779-1783. doi: 10.1126/science.1057519

Tarduno, J. A., Cottrell, R. D., Smirnov, A. V. (2002). The Cretaceous superchron geodynamo: observations near the tangent cylinder. Proceedings of the National Academy of Sciences, 99(22), 14020-14025. doi: 10.1073/pnas.222373499

Tarduno, J. A., Cottrell, R. D. (2005). Dipole strength and variation of the time - averaged reversing and nonreversing geodynamo based on Thellier analyses of single plagioclase crystals. Journal of Geophysical Research: Solid Earth, 110(B11). doi: 10.1029/2005JB003970

Tarduno, J. A., Cottrell, R. D., Smirnov, A. V. (2006). The paleomagnetism of single silicate crystals: Recording geomagnetic field strength during mixed polarity intervals, superchrons, and inner core growth. Reviews

of Geophysics, 44(1). doi: 10.1029/2005RG000189

Tarduno, J. A., Cottrell, R. D., Watkeys, M. K., Bauch, D. (2007). Geomagnetic field strength 3.2 billion years ago recorded by single silicate crystals. Nature, 446(7136), 657-660. doi: 10.1038/nature05667

Tarduno, J. A., Cottrell, R. D., Watkeys, M. K., Hofmann, A., Doubrovine, P. V., Mamajek, E. E., Liu, D., Sibeck, D. G., Neukirch, L. P., Usui, Y. (2010). Geodynamo, solar wind, and magnetopause 3.4 to 3.45 billion years ago. science, 327(5970), 1238-1240. doi: 10.1126/science.1183445

Tarduno, J. A., Cottrell, R. D., Nimmo, F., Hopkins, J., Voronov, J., Erickson, A., Blackman, E., Scott, E. R. D., McKinley, R. (2012). Evidence for a dynamo in the main group pallasite parent body. Science, 338(6109), 939-942. doi: 10.1126/science.1223932

Tarduno, J. A., Cottrell, R. D., Davis, W. J., Nimmo, F., Bono, R. K. (2015). A Hadean to Paleoarchean geodynamo recorded by single zircon crystals. Science, 349(6247), 521-524. doi: 10.1126/science.aaa9114

Thellier, E. Thellier, O. (1959). Sur l'intensite du champ magnetique terrestre dans le passe historique et geologique, Ann. Geophys., 15, 285-376.

Tsunakawa, H., Shaw, J. (1994). The Shaw method of palaeointensity determinations and its application to recent volcanic rocks. Geophysical Journal International, 118(3), 781-787. doi: 10.1111/j.1365-246X.1994.tb03999.x

Tsunakawa, H., Wakabayashi, K. I., Mochizuki, N., Yamamoto, Y., Ishizaka, K., Hirata, T., Takahashi, F., Seita, K. (2009). Paleointensity study of the middle Cretaceous Iritono granite in northeast Japan: Implication for high field intensity of the Cretaceous normal superchron. Physics of the Earth and Planetary Interiors 176(3), 235-242. doi: 10.1016/j.pepi.2009.07.001

Usui, Y., Nakamura, N. (2009). Nonlinear thermoremanence corrections for

Thellier paleointensity experiments on single plagioclase crystals with exsolved magnetites: a case study for the Cretaceous Normal Superchron. Earth, planets and space, 61(12), 1327-1337. doi: 10.1186/BF03352985

Usui, Y., Shibuya, T., Sawaki, Y., Komiya, T. (2015). Rock magnetism of tiny exsolved magnetite in plagioclase from a Paleoarchean granitoid in the Pilbara craton. Geochemistry, Geophysics, Geosystems, 16(1), 112-125. doi: 10.1002/2014GC005508

Veitch, R.J., Hedley, I.G. Wagner, J.J., (1984). An investigation of the intensity of the geomagnetic-field during Roman times using magnetically anisotropic bricks and tiles, Arch. Sci., 37, 359–373.

Yamamoto, Y., Tsunakawa, H., Shibuya, H. (2003). Palaeointensity study of the Hawaiian 1960 lava: implications for possible causes of erroneously high intensities. Geophysical Journal International, 153(1), 263-276. doi: 10.1046/j.1365-246X.2003.01909.x

Yamamoto, Y., Tsunakawa, H. (2005). Geomagnetic field intensity during the last 5 Myr: LTD - DHT Shaw palaeointensities from volcanic rocks of the Society Islands, French Polynesia. Geophysical Journal International, 162(1), 79-114. doi: 10.1111/j.1365-246X.2005.02651.x

Yamamoto, Y., Torii, M., Natsuhara, N. (2015). Archeointensity study on baked clay samples taken from the reconstructed ancient kiln: implication for validity of the Tsunakawa-Shaw paleointensity method. Earth, Planets and Space, 67(1), 63. doi: 10.1186/s40623-015-0229-8

Yu, Y. (2010). Paleointensity determination using anhysteretic remanence and saturation isothermal remanence. Geochemistry, Geophysics, Geosystems, 11(2). doi: 10.1029/2009GC002804

Yu, Y. (2011). Importance of cooling rate dependence of thermoremanence in paleointensity determination. Journal of Geophysical Research: Solid Earth, 116(B9). doi: 10.1029/2011JB008388

Wakabayashi, K. I., Tsunakawa, H., Mochizuki, N., Yamamoto, Y., Takigami, Y. (2006). Paleomagnetism of the middle Cretaceous Iritono granite in the Abukuma region, northeast Japan. Tectonophysics 421(1), 161-171. doi: 10.1016/j.tecto.2006.04.013

Wenk, H. R., Chen, K., Smith, R. (2011). Morphology and microstructure of magnetite and ilmenite inclusions in plagioclase from Adirondack anorthositic gneiss. American Mineralogist, 96(8-9), 1316-1324. doi: 10.2138/am.2011.3760

Figures and Tables

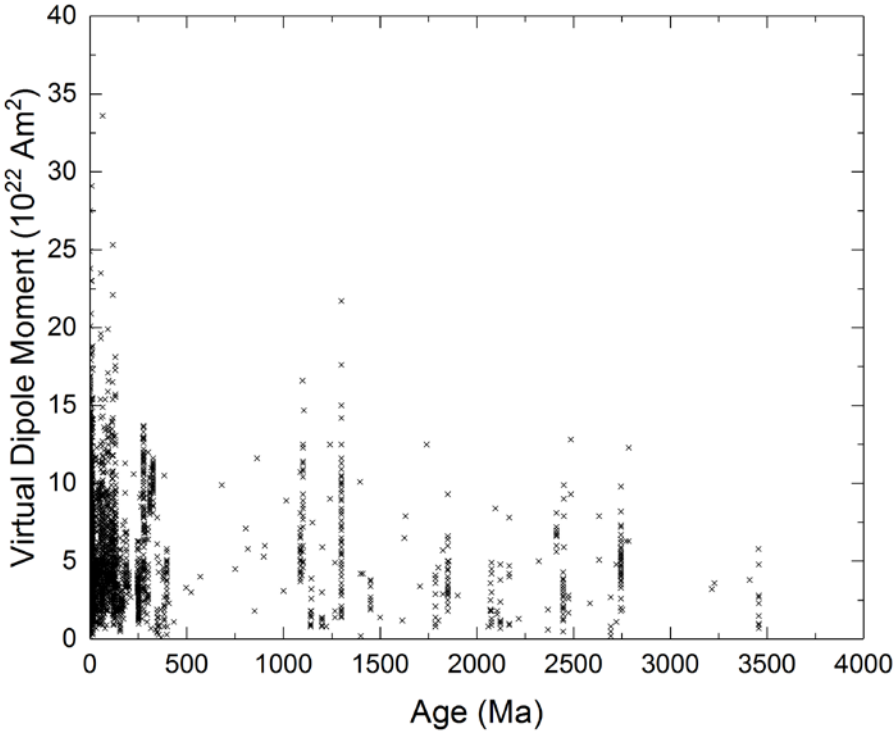

Fig. 1 All paleointensity results compiled in the PINT database.

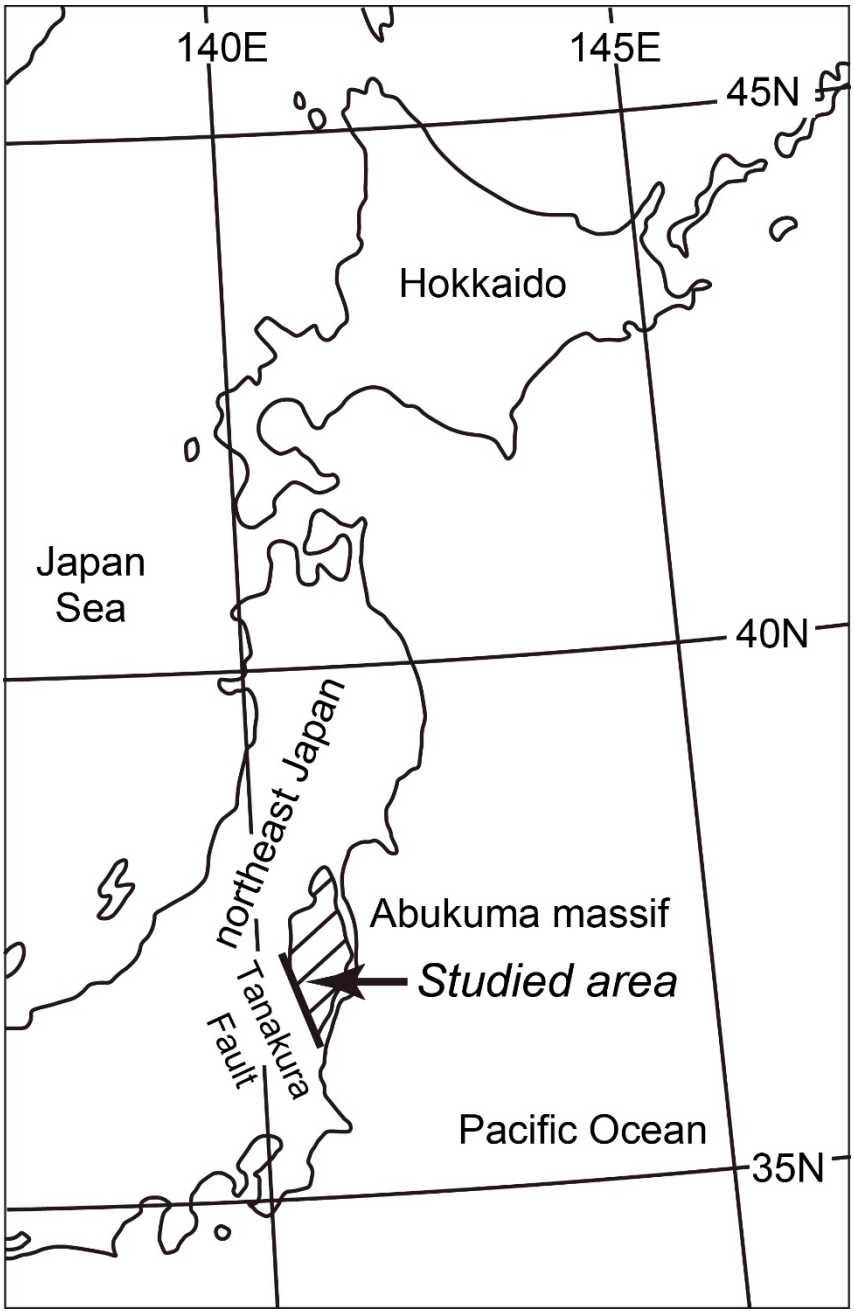

Fig. 2 Map of the Iritono granite in the Abukuma massif, northeast Japan (reproduced from Wakabayashi et al., 2006).

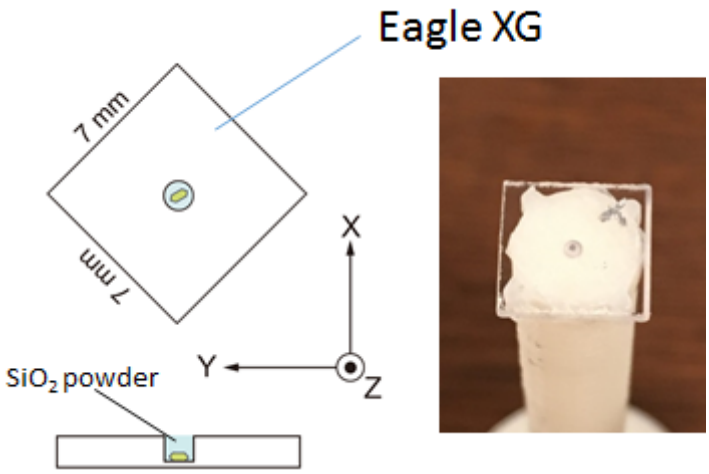

Fig. 3 Schematic illustration and photograph of the grass holder for oriented high temperature treatment of single crystal samples. The photograph shows the glass holder mounted on the ABS holder by double sticking tape.

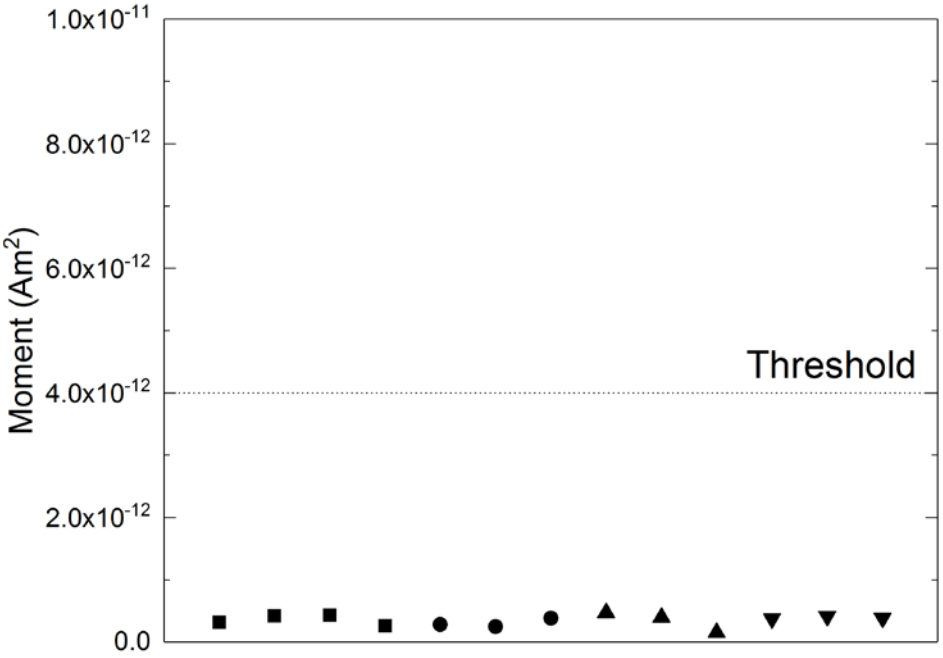

Fig. 4 Magnetic moment (NRM) of the glass holders. Different symbols indicate each holder.

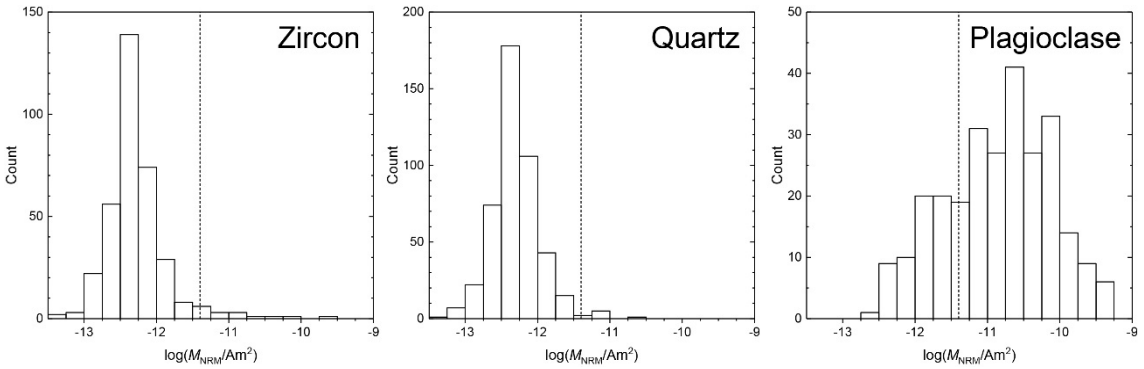

Fig. 5 Histogram of NRM intensity of zircon, quartz and plagioclase. Dotted lines indicate the threshold for significant remanence.

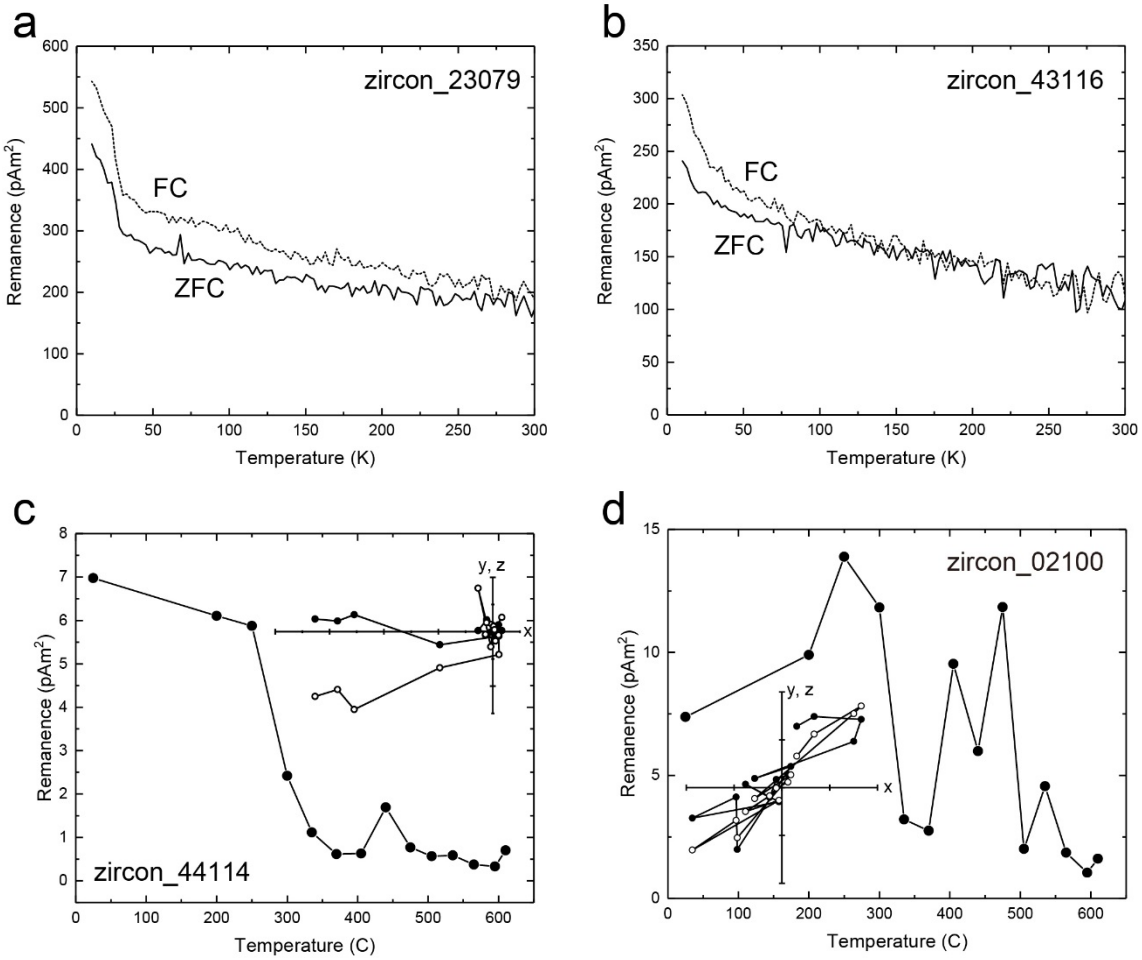

Fig. 6 Results of experiments on selected zircon. a,b Low-temperature remanence measurements. Solid lines for ZFC measurements and dotted lines for FC measurements. c,d Stepwise ThD of NRM.

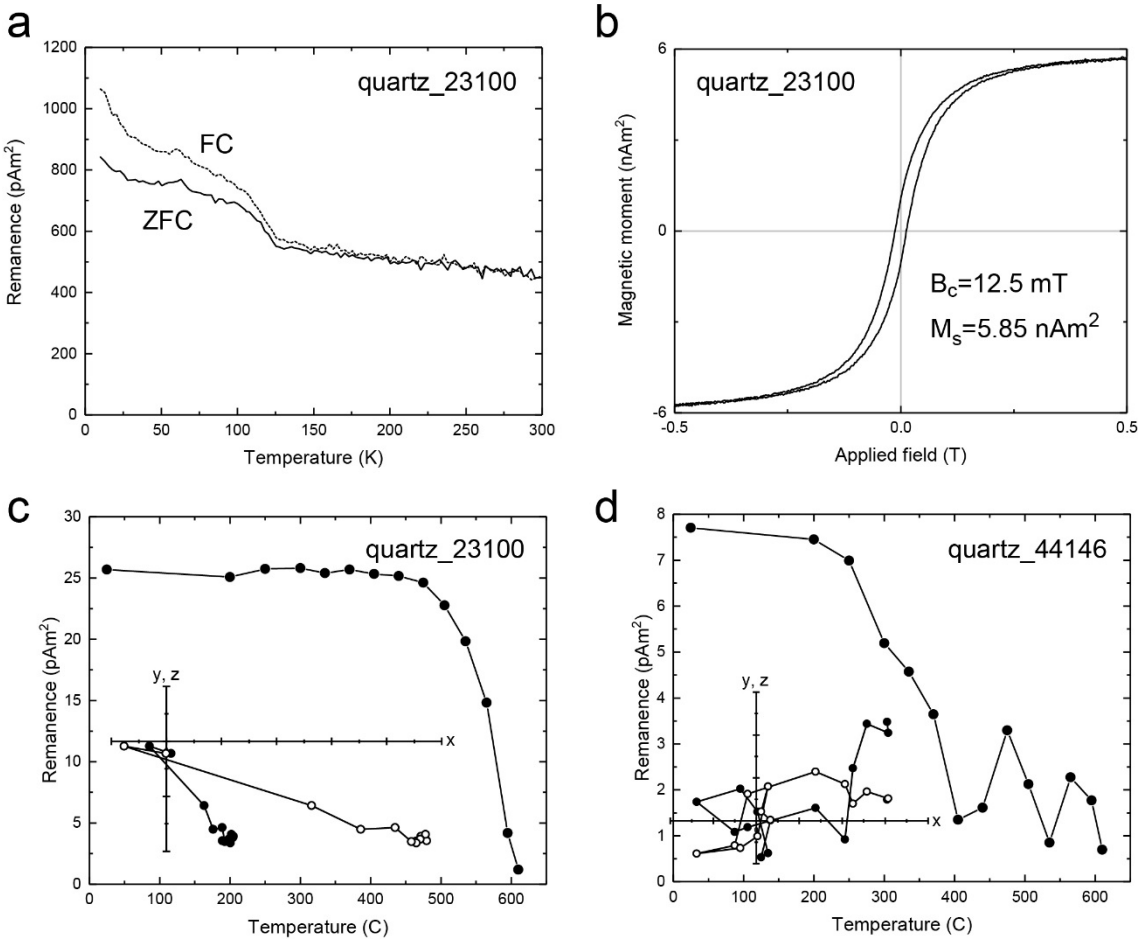

Fig. 7 Results of experiments on selected quartz. a Low-temperature remanence measurements. Solid lines for ZFC measurements and dotted lines for FC measurements.

b Hysteresis loop measurement. c,d Stepwise ThD of NRM.

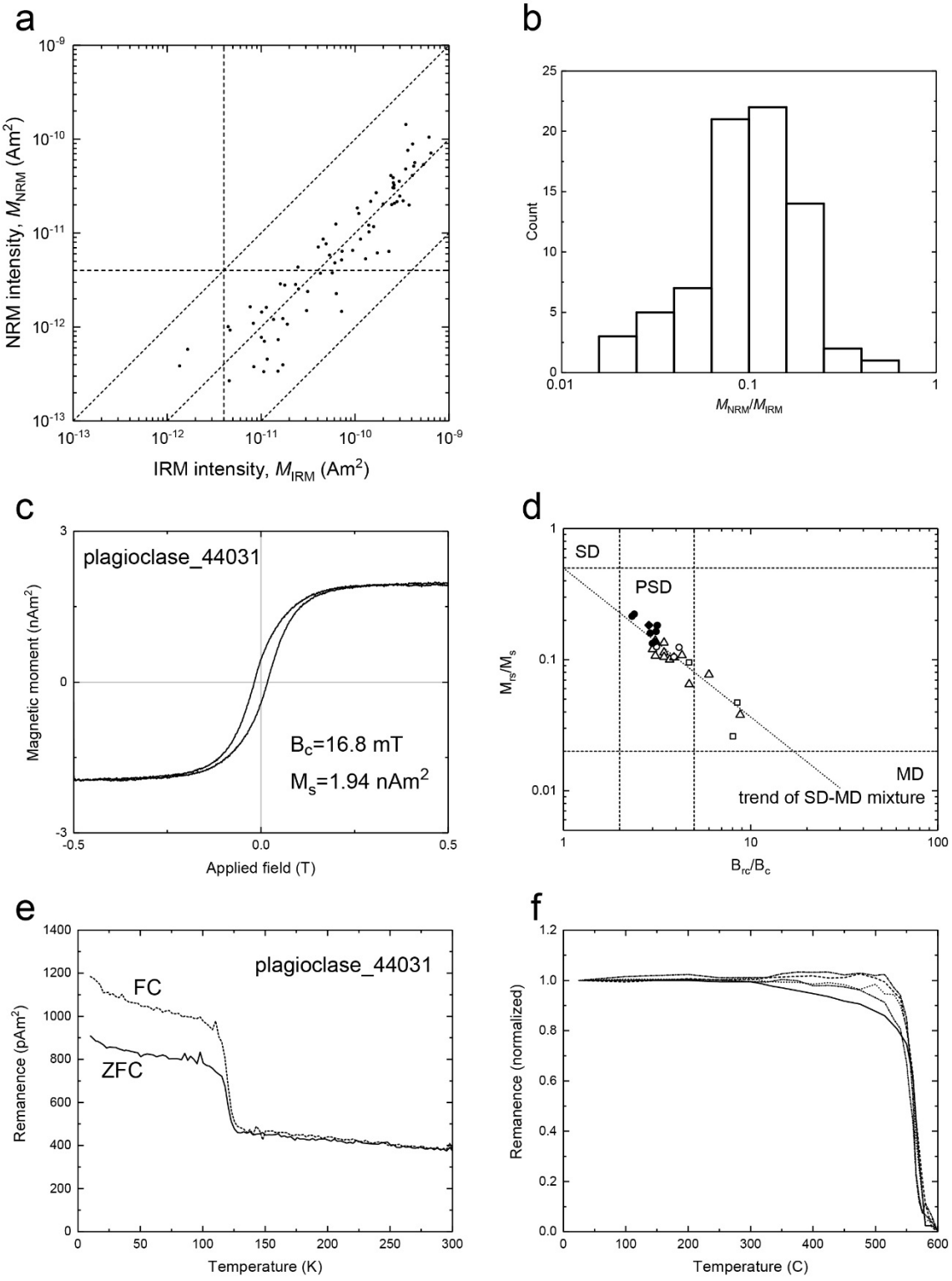

Fig. 8 Results of experiments on plagioclase. **a.** NRM intensity plotted as a function of IRM intensity. Horizontal and vertical dashed lines indicate the threshold for significant remanence. **b.** Histogram of NRM intensity divided by IRM intensity. **c.** Hysteresis loop measurement. **d.** Day plot of quartz and

plagioclase grains shown with previous reports by Wakabayashi et al. (2006). Closed symbols represent results of this study. Diamond indicate quartz and circle indicate plagioclase. Opened symbols represent results of Wakabayashi et al. (2006). Triangle, circle and square indicate non-separated chips, feldspar fraction and biotite fraction, respectively. Dotted lines show the SD-MD magnetite mixture trend after Channell and McCabe (1994) and Parry (1982). **e.** Low-temperature remanence measurements. Solid lines for ZFC measurements and dotted lines for FC measurements. **f.** Stepwise ThD of TRM given at 50 μT compared to NRM of the whole-rock (Wakabayashi et al., 2006). Dashed lines for plagioclase grains and solid line for whole-rock. **g.** The Jelinek diagram of single plagioclase crystals. Closed and circles for this study and Usui et al. (2015).

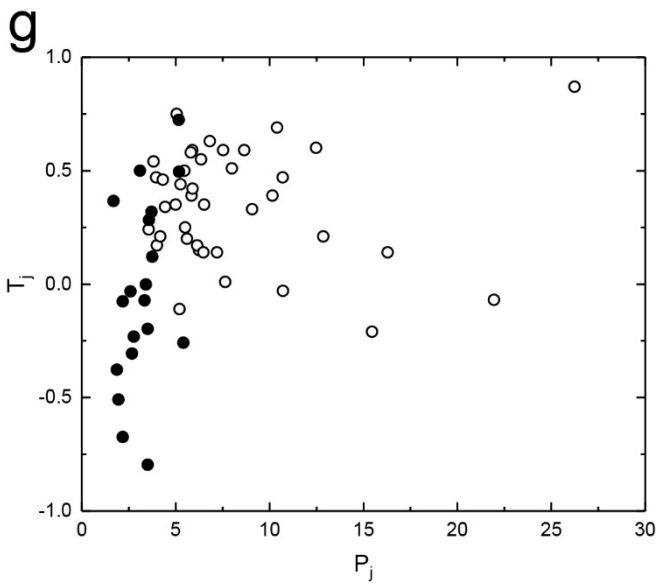

Fig. 8 (continued) g. The Jelinek diagram of single plagioclase crystals. Closed and circles for this study and Usui et al. (2015).

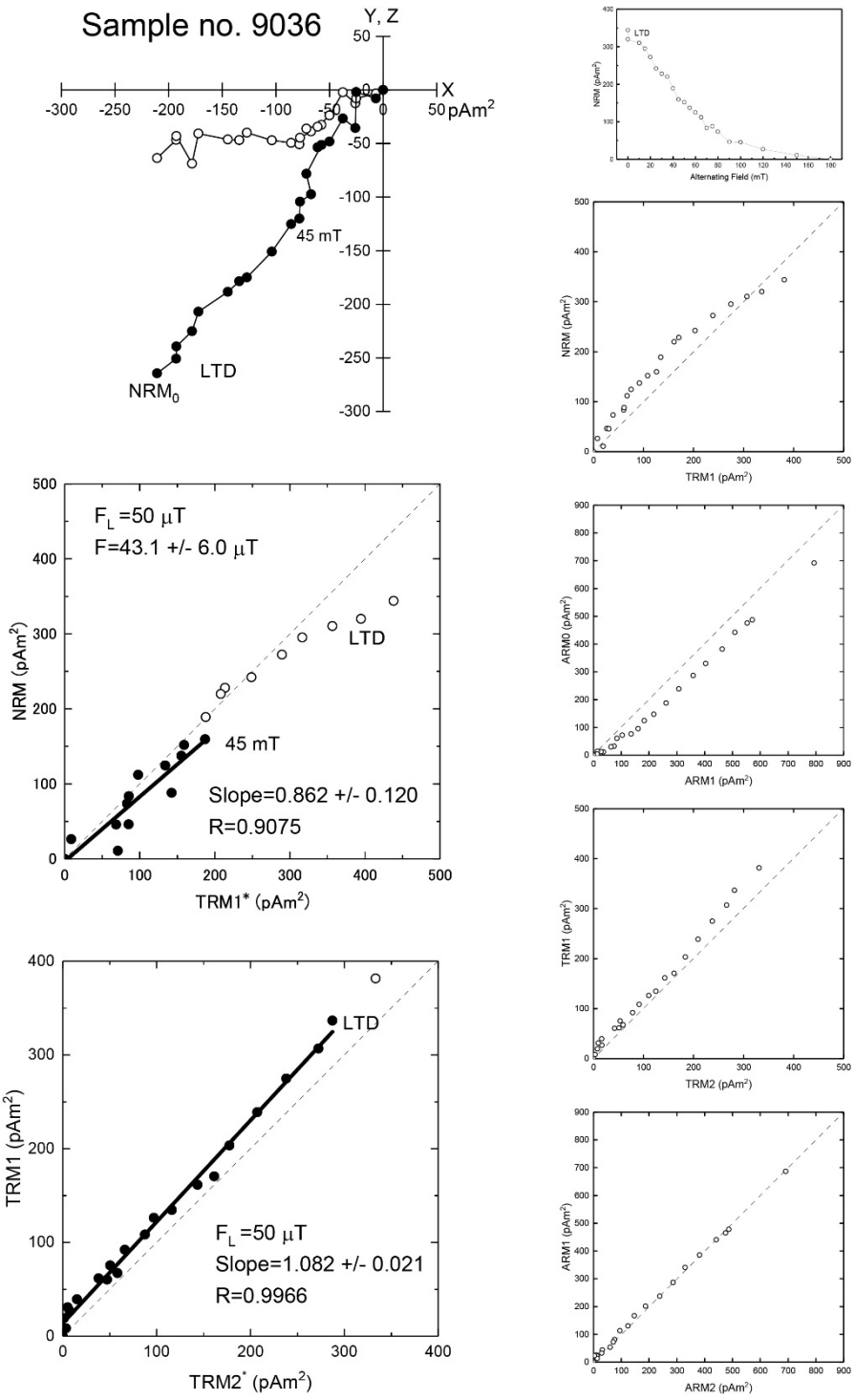

Fig. 9 A representative result of successful paleointensity measurements by the Tsunakawa-Shaw method on single plagioclase grain. The dotted line indicates where the horizontal and vertical axes are equal. In the orthogonal plot, open and closed circles indicate X-Y and X-Z planes, respectively.

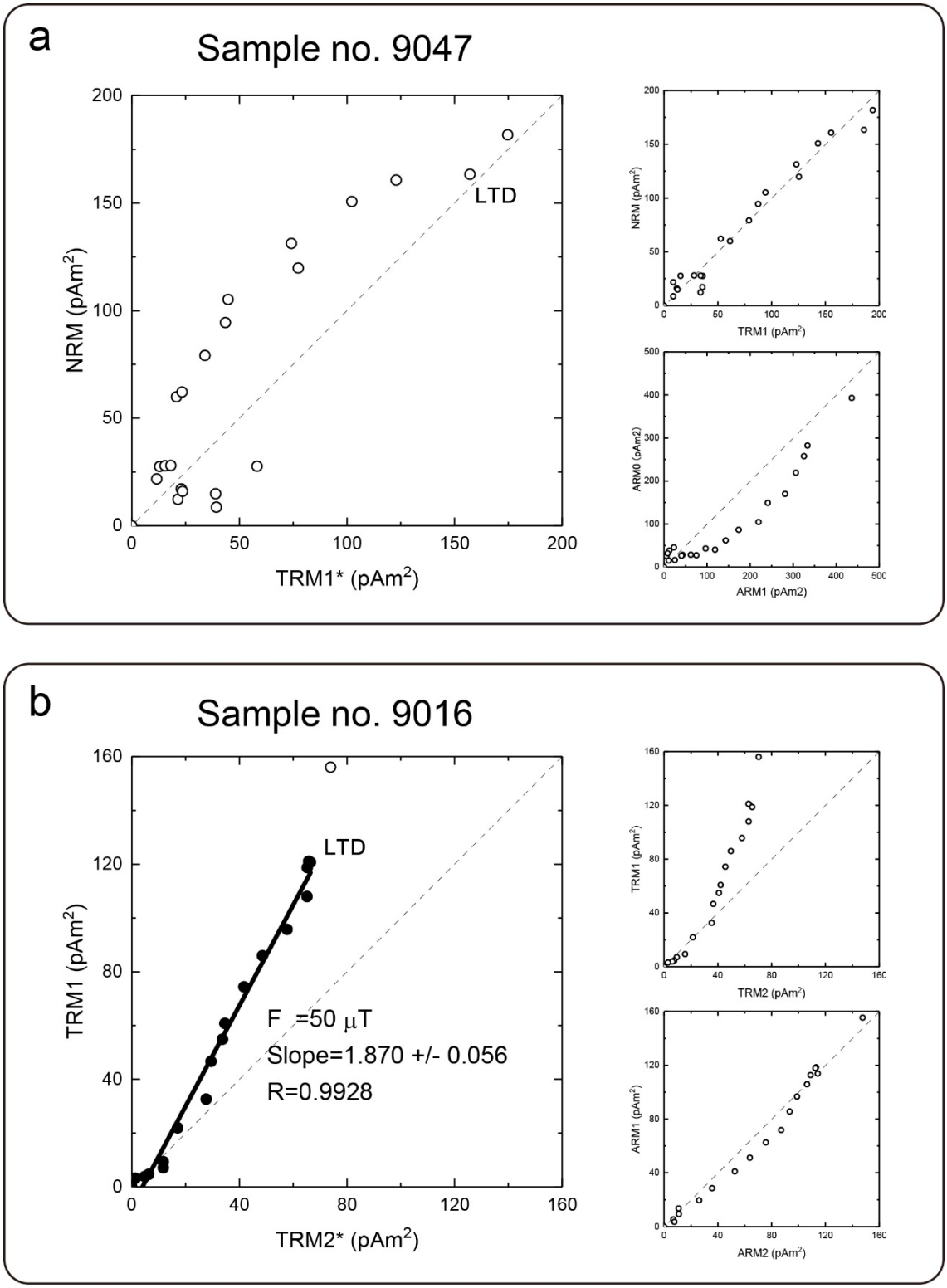

Fig. 10 Examples of failed paleointensity measurements by the Tsunakawa-Shaw method on single plagioclase grain. a No linear portion in the NRM/TRM1* plot. b TRM1/TRM2* slope severely exceeds 1.

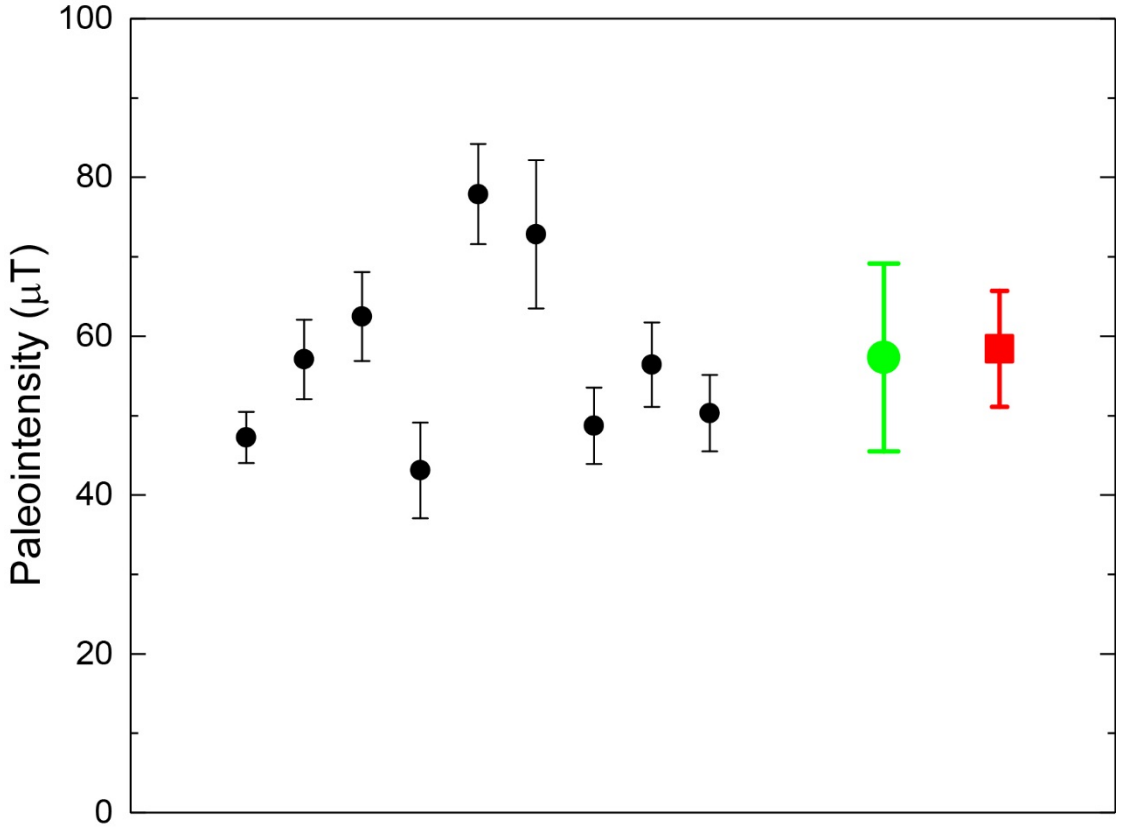

Fig. 11 Summary of paleointensity and error (1□) of plagioclase compared with the whole-rock. Black circles indicate results of each plagioclase grain. Green circle denotes the mean of nine plagioclase grains. Red square marks the mean of whole-rock measurements (Tsunakawa et al., 2009).

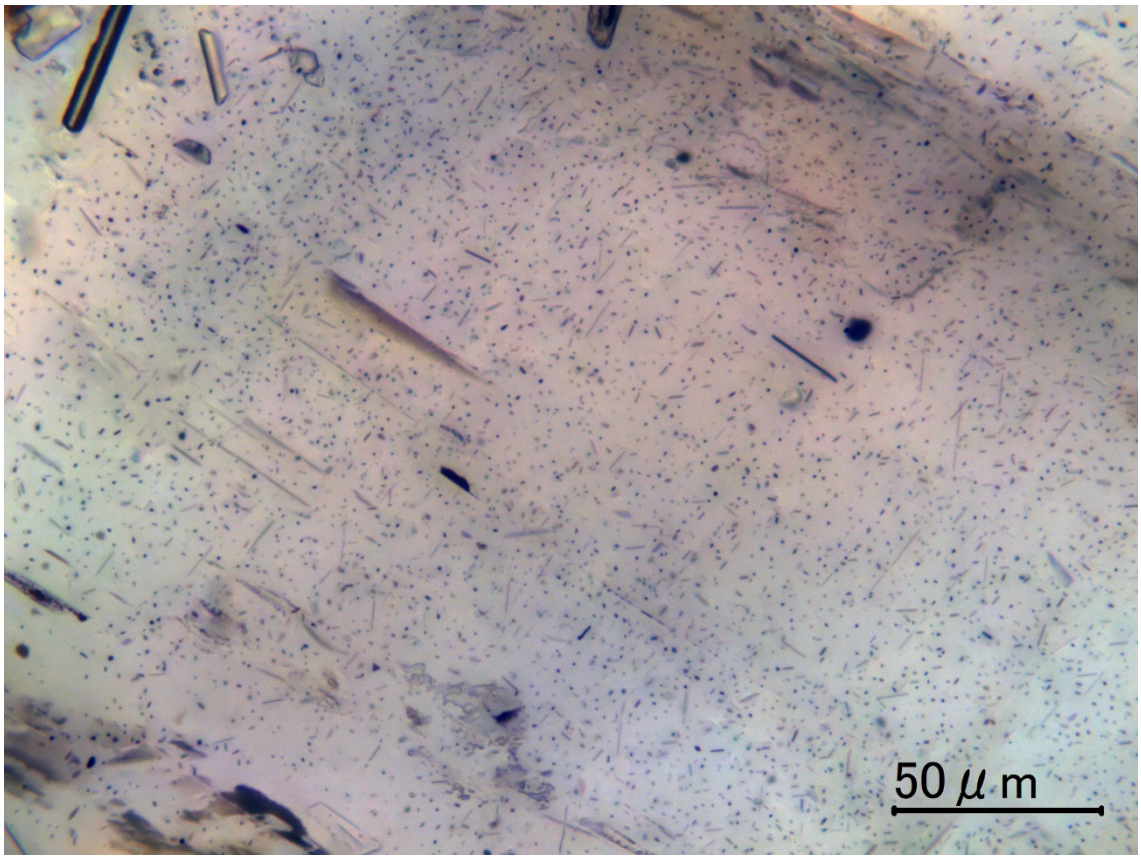

Fig. 12 Microscopic image of a polished single plagioclase crystal. Stacking of snaps of different focal depths.

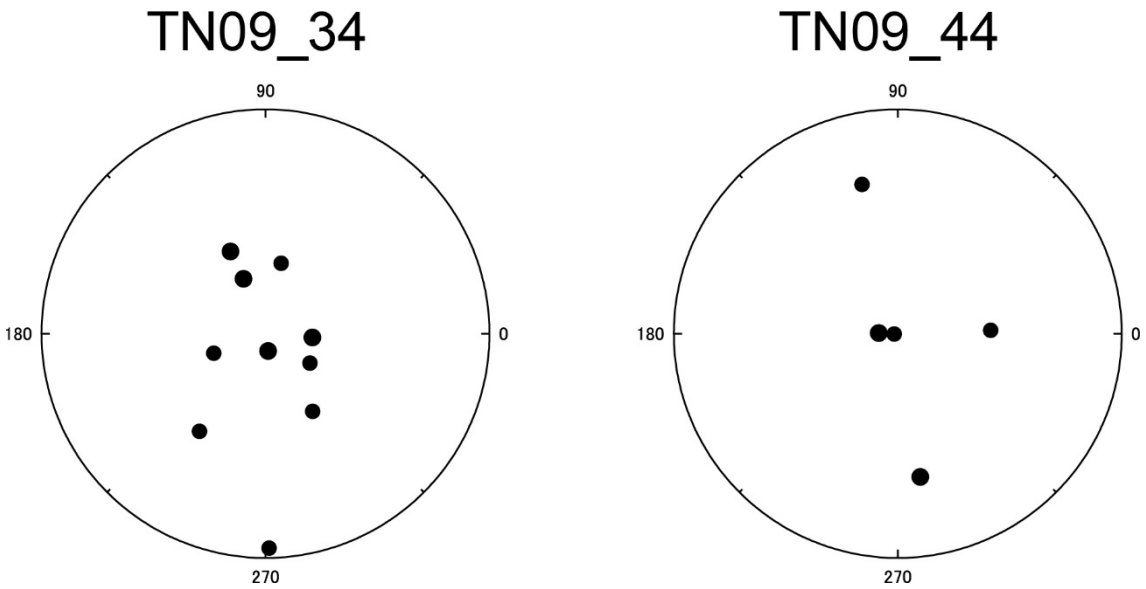

Fig. 13 NRM directions of plagioclase samples are plotted in equal-area projection where the x, y, and z axes are transformed to the directions of the maximum, medium and minimum eigenvectors. Center of the plot area indicates the magnetic easy axis.

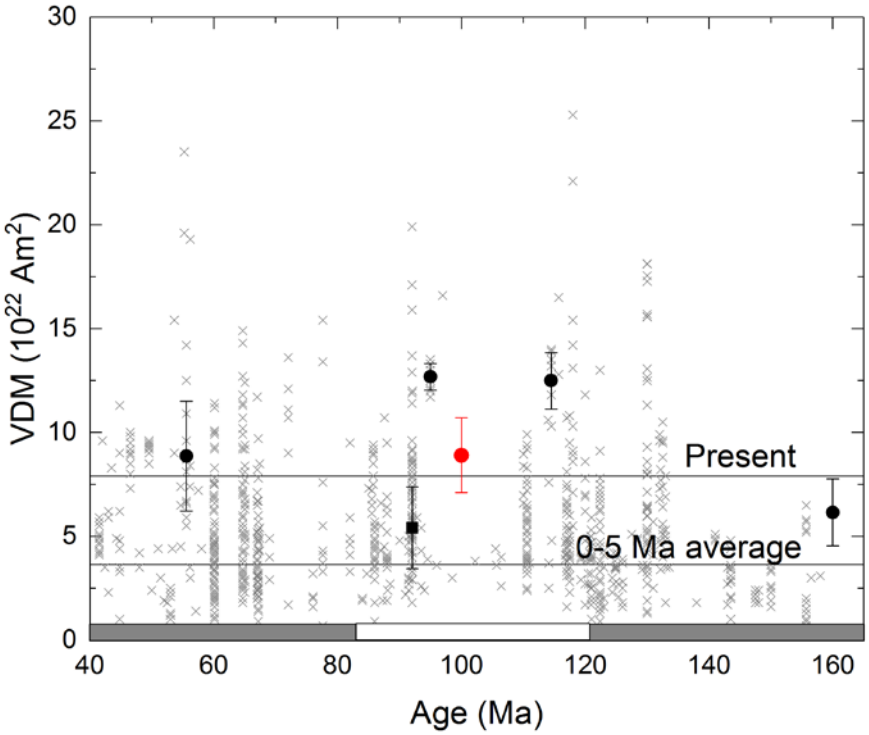

Fig. 14 VDM for 40 Ma to 165 Ma. White and gray bars indicate the time range of the Cretaceous normal superchron and reversing periods, respectively (Gee and Kent, 2007). The red circle shows our present result. Black circles are results on single plagioclase crystals separated from lava (Tarduno et al., 2001; 2002; 2005). Squares indicate results on an ophiolite gabbro (Granot et al., 2007). Crosses are data from PINT.

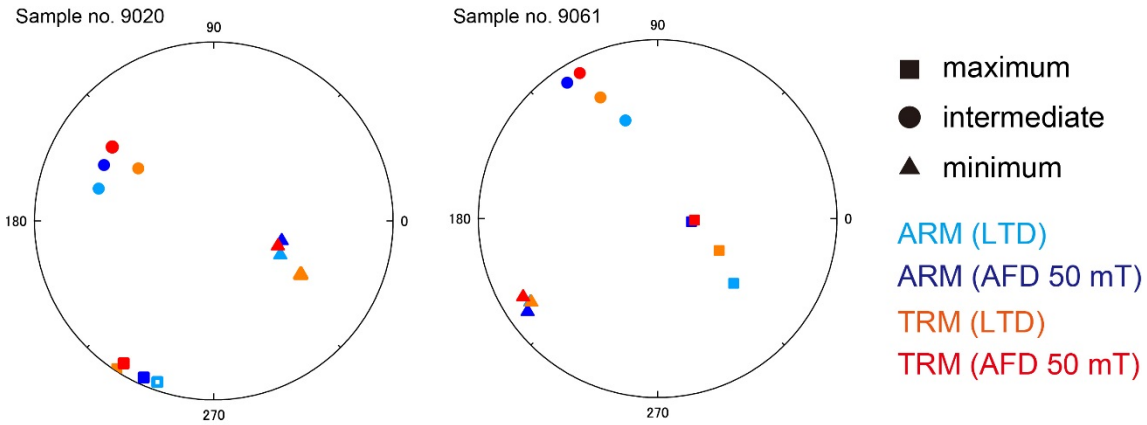

	P_j	T_j
ARM (LTD)	3.23	0.20
ARM (AFD 50 mT)	5.28	0.23
TRM (LTD)	3.65	0.08
TRM (AFD 50 mT)	7.64	0.12

	P_j	T_j
ARM (LTD)	2.98	0.41
ARM (AFD 50 mT)	3.74	0.47
TRM (LTD)	2.76	0.13
TRM (AFD 50 mT)	5.88	0.37

Fig. 15 Representative results on the anisotropy axes measurement on single plagioclase crystals.

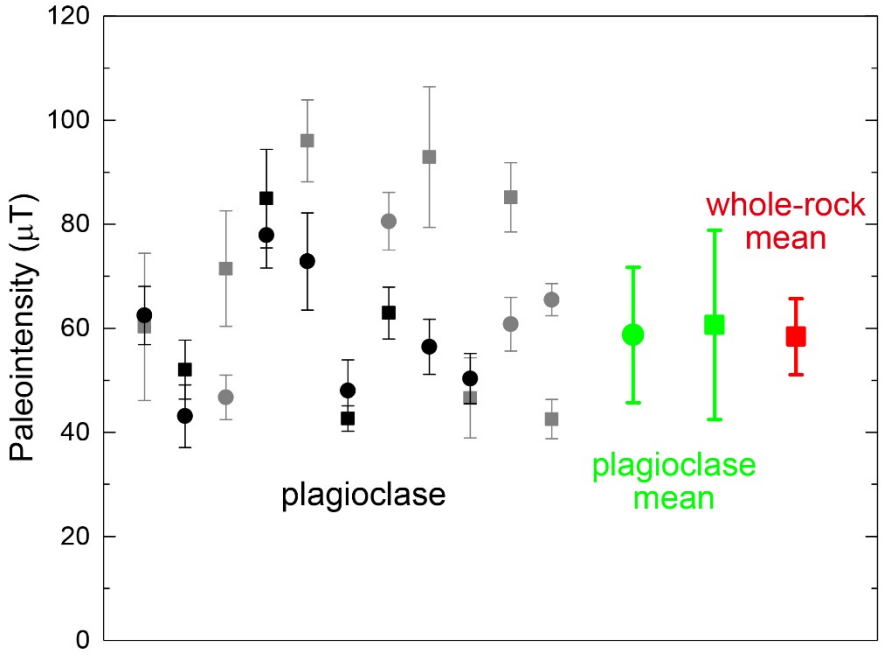

Fig. 16 Summary of anisotropy-corrected paleointensity for plagioclase crystals. Circles and rectangles are for results before and after correction. Grey color indicates samples that failed the paleointensity criteria.

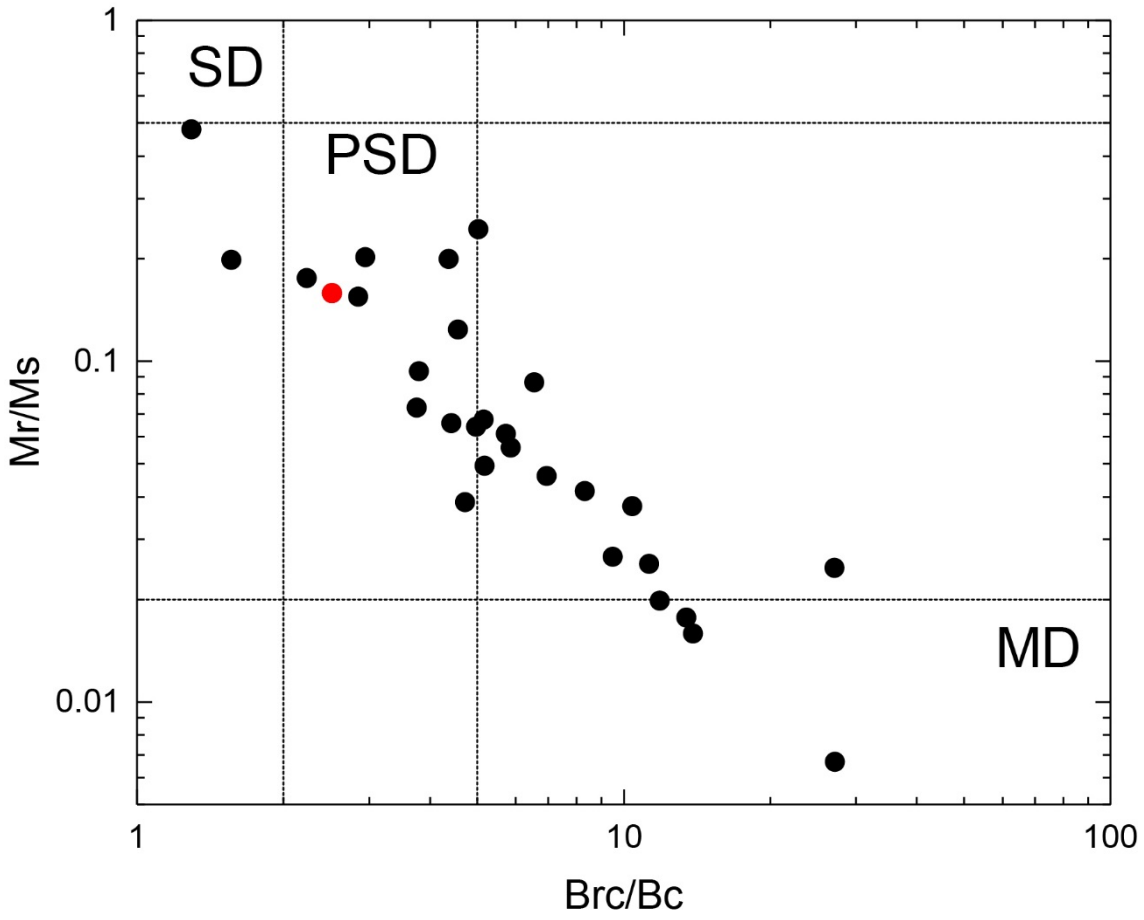

Fig. 17 Day plot of plagioclase samples. Iritono granite is indicated by the red circle.

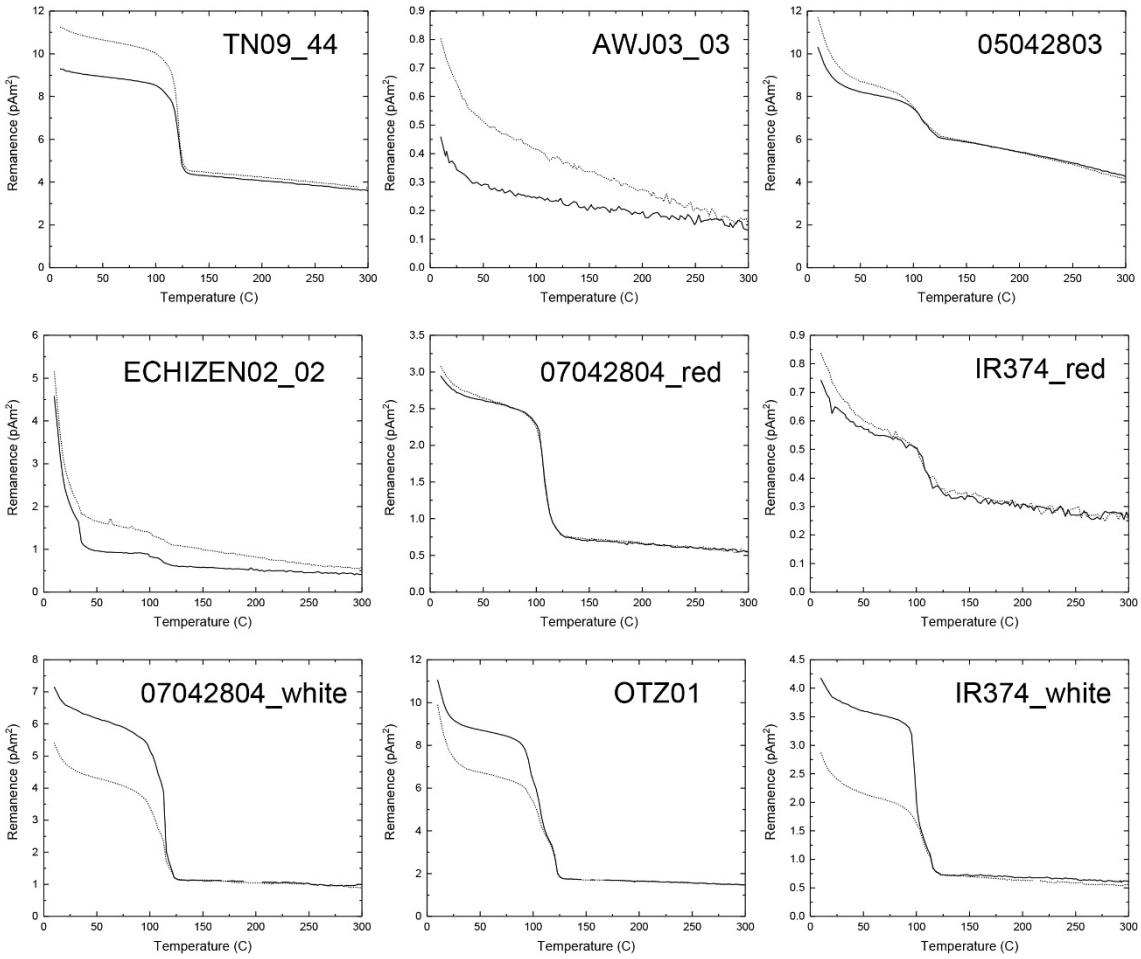

Fig. 18 Results of low-temperature remanence measurements on plagioclase samples. Solid lines for ZFC measurements and dotted lines for FC measurements.

Table 1 Summary of previous studies on single crystal paleomagnetism

	Sample description				
Authors	locallity	age	rock type	single crystal	measurements and distinct instrument
Cottrell and Tarduno (1999)	1955 Kilauea eruption	A.D. 1955	lava	plagioclase	paleointensity, hysteresis
Cottrell and Tarduno (2000)	Rajmahal Traps, eastern India	113-116 Ma	basalt	plagioclase	paleointensity
Tarduno et al. (2001)	Rajmahal Traps, eastern India	113-116 Ma	basalt	plagioclase	paleointensity
Tarduno et al. (2002)	Strand Fiord Formation, Canada	95 Ma	basalt	plagioclase	paleointensity, hysteresis
Tarduno and Cottrell (2005)	ODP	56, 160 Ma	lava	plagioclase	paleointensity, hysteresis, FORC
Feinberg et al. (2005)	various		mafic intrusive rocks	plagioclase, clinopyroxene	MDF, inclusion diameter
Tarduno et al. (2006)	1955 Kilauea eruption	A.D. 1955	lava	plagioclase	paleointensity, hysteresis, FORC
Tarduno et al. (2007)	Dalmein and Kaap Valley Plutons, Barberton	3.2 Ga	granodioritic and tonalitic	microcline, quartz, hornblende	paleointensity
Cottrell et al. (2008)	Kiama, Australia	262-318 Ma	lava	plagioclase	paleointensity, hysteresis, anisotropy
Tarduno et al. (2010)	Kaapvaal	3.4-3.45 Ga	dacite	quartz	paleointensity
Tarduno et al. (2012)	meteorite			olivine	paleointensity, hysteresis, FORC
Muxworthy and Evans (2012)	Modipe Gabbro, Botswana	2784 Ma	gabbro	pyroxene	paleointensity (synthetic), hysteresis, FORC, IRM acquisition
Tarduno et al. (2014)	Barberton	3.4-3.45 Ga	metaconglomerate	zircon, quartz	paleointensity
Fu et al. (2014)	Semarkona meteorite			dusty olivine	paleointensity
Sato et al. (2015)	Tanzawa	4-5 Ma	river sand	zircon	hysteresis, stepwise AFD, low-T, IRM
Usui et al. (2015)	Mt. Edgar, Pilbara	3.2-3.3 Ga	granitoid	plagioclase	hysteresis, FORC, TRM acquisition, ARM acquisition, anisotropy
Tarduno et al. (2015)	Jack Hills	3.3-4.2 Ga	conglomerate	zircon	paleointensity
Fu et al. (2017)	Bishop Tuff	767.1 ka	ignimbrite	zircon	paleointensity, SQUID microscope, QDM

Table 2 Anisotropy parameters of plagioclase samples. Mean ARM: average of the eigenvalues of ARM anisotropy tensor; w1, w2 and w3: maximum, medium and minimum eigenvalue of ARM anisotropy tensor normalized by the mean ARM.

Sample Name	Mean ARM (10^{-10} Am^2)	w_1	w_2	w_3	P	P_j	T_j
9020	3.22	1.70	0.81	0.49	3.48	3.51	-0.20
9036	4.49	1.56	1.01	0.43	3.64	3.72	0.32
9099	1.77	1.50	0.92	0.58	2.60	2.60	-0.03
9054	2.14	1.42	0.93	0.65	2.19	2.19	-0.08
9070	2.14	1.36	0.90	0.74	1.84	1.87	-0.38
34019	1.64	1.60	1.07	0.33	4.87	5.18	0.49
44092	0.95	1.43	1.09	0.48	2.96	3.10	0.50
9035	3.06	1.40	0.86	0.74	1.91	1.96	-0.51
9047	2.54	1.23	1.04	0.73	1.68	1.70	0.37
9061	1.58	1.64	0.88	0.48	3.41	3.41	0.00
9113	3.08	1.57	0.83	0.60	2.64	2.68	-0.31
44106	0.85	1.58	0.85	0.57	2.75	2.78	-0.23
44108	0.71	1.48	0.80	0.71	2.07	2.19	-0.67
11	1.16	1.65	0.86	0.49	3.34	3.35	-0.07
12	2.22	1.95	0.68	0.37	5.31	5.41	-0.26
16	1.81	1.56	0.99	0.44	3.52	3.58	0.28
36	2.14	1.64	0.92	0.44	3.75	3.76	0.12
55	1.91	1.48	1.20	0.32	4.55	5.17	0.72
68	1.35	1.79	0.64	0.57	3.14	3.52	-0.80

Table 3 Results on Paleointensity measurements of plagioclase samples. NRM0: NRM intensity before LTD; HL: the lowest AFD step used in paleointensity estimate; f: NRM fraction of the primary magnetization used in paleointensity estimate; R: correlation coefficient; F: estimated paleointensity; r: ratio of ARM0 and ARMy.

					first heating				second heating							
sample ID	NRM_0 (pAm^2)	H_L (mT)	f	MAD (°)	Slope			R	Slope			R	F (μT)			r
successful samples																
9004	134.65	0	1.000	9.2	0.945	±	0.064	0.9647	1.054	±	0.050	0.9827	47.2	±	3.2	1.40
9009	93.02	40	0.700	9.8	1.142	±	0.100	0.9706	1.094	±	0.021	0.9972	57.1	±	5.0	1.14
9020	483.98	45	0.486	9.2	1.253	±	0.083	0.9658	1.048	±	0.026	0.9944	62.6	±	4.2	1.18
9036	343.98	45	0.499	10.2	0.862	±	0.120	0.9075	1.082	±	0.021	0.9966	43.1	±	6.0	1.33
9099	193.13	0	1.000	11.0	1.558	±	0.126	0.9456	1.051	±	0.056	0.9744	77.9	±	6.3	0.91
9054	264.76	35	0.570	15.9	1.457	±	0.187	0.9075	1.078	±	0.061	0.9710	72.8	±	9.4	1.23
9070	126.67	15	0.942	12.9	0.974	±	0.096	0.9259	0.968	±	0.032	0.9900	48.7	±	4.8	1.03
34019	103.97	20	0.868	11.0	1.129	±	0.106	0.9394	0.960	±	0.031	0.9908	56.4	±	5.3	0.83
44092	64.66	10	0.992	10.6	1.007	±	0.096	0.9301	1.008	±	0.041	0.9851	50.3	±	4.8	0.98
												mean	57.4	±	11.8	1.11
failed samples																
9013	90.83	35	0.677	7.9	1.424	±	0.095	0.9785	0.887	±	0.051	0.9728	71.2	±	4.7	
9016	79.46	35	0.600	11.1	0.678	±	0.045	0.9806	1.686	±	0.140	0.9703	33.9	±	2.3	
9035	269.58	no primary magnetization							0.961	±	0.035	0.9872				
9047	181.62	low linearity in NRM/TRM1* plot							0.971	±	0.029	0.9909				
9061	174.38	20	0.860	8.9	0.935	±	0.086	0.9420	1.232	±	0.070	0.9705	46.7	±	4.3	
9113	495.66	25	0.855	8.9	1.611	±	0.111	0.9662	1.173	±	0.065	0.9722	80.6	±	5.6	
44106	88.54	20	0.923	5.9	1.216	±	0.104	0.9465	0.849	±	0.078	0.9276	60.8	±	5.2	
44108	76.16	0	1.000	5.3	1.310	±	0.062	0.9847	0.627	±	0.119	0.7706	65.5	±	3.1	

Table 4 Anisotropy parameters of whole-rock samples. w_1, w_2 and w_3: maximum, medium and minimum eigenvalue of ARM anisotropy tensor normalized by the mean ARM.

Sample Name	w_1	w_2	w_3	P	P_j	T_j
TN09_06	1.14	0.98	0.88	1.30	1.30	-0.12
TN09_21	1.12	0.96	0.93	1.21	1.22	-0.61
TN09_24	1.13	0.97	0.91	1.25	1.26	-0.42
TN09_26	1.09	0.99	0.92	1.19	1.19	-0.14
TN09_31	1.10	1.00	0.90	1.21	1.21	0.03
TN09_33	1.12	0.97	0.91	1.22	1.23	-0.38
TN09_34	1.04	1.03	0.93	1.12	1.13	0.79
TN09_44	1.14	0.96	0.90	1.28	1.29	-0.46
TN09_45	1.16	0.94	0.91	1.28	1.30	-0.72

Table 5. Summary of granite samples used for magnetic hysteresis measurements of plagioclase. Granite type: classification of granitic rocks based on magnetic susceptibility by Ishihara (1977); size: based on H_{rc}/H_c ratio.

Sample name	Location	Age (Ma)	susceptibiluty (10^3 SI unit)	Granite type	Mr (nAm^2)	Mr/Ms	Hrc/Hc	Domain state	Age reference
TN09_44	ITG09, Iritono	116	2.9	magnetite	1.84	0.16	2.52	PSD	Wakabayashi et al. (2006)
TN10_06	ITG10, Iritono	116		magnetite	2.82	0.09	6.56	MD	
YKS06_02_pl_181 (single crystal)	Tanzawa	4.5	293.7	magnetite	3.74	0.02	13.90	MD	Tani et al. (2010)
YKS06_02_pl_183 (single crystal)	Tanzawa	4.5	293.7	magnetite	2.44	0.03	9.50	MD	
YKS07_03_pl_008 (single crystal)	Tanzawa	4.5	332.9	magnetite	0.80	0.07	5.16	MD	
YKS07_03_pl_009 (single crystal)	Tanzawa	4.5	332.9	magnetite	1.30	0.06	5.87	MD	
OTZ01	Tanzawa	4.5	315.9	magnetite	0.45	0.02	13.46	MD	
07042804_white	Daito, San-in	53-82	56.5	magnetite	1.87	0.03	11.28	MD	Ishihara and Hayasaka (2007)
07042804_red	Daito, San-in	53-82	56.5	magnetite	0.44	0.05	6.95	MD	
07042804_017 (single crystal)	Daito, San-in	53-82	56.5	magnetite	1.29	0.02	11.86	MD	
07042804-016 (single crystal)	Daito, San-in	53-82	56.5	magnetite	0.72	0.06	4.98	PSD	
2014101803C_red	Hiroshima, Sanyo	83	0.7	ilmenite	0.14	0.24	5.03	MD	Shibata and Ishihara (1974)
2014101803C_white	Hiroshima, Sanyo	83	0.7	ilmenite	0.22	0.48	1.29	SD	
05042803	Nunobe, San-in	56	22.6	magnetite	1.38	0.09	3.79	MD	
IR374_white	Ireland	387	7.3	magnetite	0.90	0.01	27.15	MD	O'Connor (1989)
IR374_red	Ireland	387	7.3	magnetite	0.45	0.04	10.43	MD	
A4_black	Chitragurga Granite, India	2610	9.8	magnetite	0.17	0.02	27.11	MD	Jayananda et al. (2006)
A4_white	Chitragurga Granite, India	2610	9.8	magnetite	0.18	0.20	4.37	PSD	
95NP207	North Pole, Arstralia	3460	5.1	magnetite	0.12	0.20	1.56	SD	Huston et al. (2002)
110716_2	Tottori	32.9			0.84	0.06	5.73	MD	Tani et al. (2014)
73H64	Shimane	39.8			0.52	0.04	8.32	MD	
HANASE02_01	Shiga	105.4			0.49	0.05	5.18	MD	
KUM_36	Yamaguchi	32.4			0.21	0.04	4.73	PSD	
KUM_36	Yamaguchi	32.4			0.17	0.07	3.76	PSD	
70T0135	Tottori	63.4			0.29	0.07	4.43	PSD	
73M15	Kyoto	62.2			0.76	0.17	2.23	PSD	
ECHIZEN02_02	Fukui	66.0	0.8	ilmenite	0.33	0.12	4.57	PSD	
AWJ03_03	Awajishima	97.9	0.3	ilmenite	0.44	0.20	2.95	PSD	
75M13	Ehime	97.8			0.18	0.15	2.85	PSD	

Chapter 5

Exploring the thermal evolution of the deep Earth by the long-term trend of the geomagnetic field

§1 Major influencing factors on the long-term trend of the geomagnetic field

In Chapter 1, I discussed that tracking the long-term changes of the geomagnetic field provides important clues for revealing the thermal evolution of the Earth's deep interior. To interpret the paleomagnetic signals as evidence of thermal evolution, it is necessary to understand what causes changes in the paleomagnetic parameters such as the field intensity, reversal rate and geomagnetic morphology. In general, the stability of a dynamo is affected by three major factors, including: (1) strength of the convection, (2) heterogeneity of the heat flow at the CMB, and (3) effect of the solid inner core.

Planetary dynamos are driven by thermal and compositional convection. Dynamo action is maintained when the total CMB heat flow is larger than a critical value. Numerical dynamo models show that with increasing total CMB heat flow, the reversal frequency increases and the dipole component of the total magnetic energy decreases (e.g. Kutzner and Christensen, 2002; Christensen and Aubert, 2006; Olson and Christensen, 2006). Fig. 1 shows the schematic illustration of the dependence of reversal frequency and dipole moment on the total CMB heat flow. This indicates that non-reversing stable dynamos with strong dipole moments will occur under conditions of relatively low CMB heat flow, whereas a reversing dynamo with multipolar nature are expected under conditions with high CMB heat flow.

Dynamo simulations have long shown that the thermal structure of the lowermost mantle should affect convection and the geomagnetic field. Spatial heterogeneity at the CMB could influence the field strength and reversal

frequency (e.g. Larson and Olson, 1991; Glatzmaier et al., 1991; Courtillot and Olson, 2007; Takahashi et al., 2008; Olson et al. 2010; Olson, 2016). Numerical simulations by Takahashi et al. (2008) revealed that the dipole field is strengthened when the heat flow anomaly is distributed largely on the equator (spherical surface harmonics Y_m^m). The dipole strength increases with increasing degree of heterogeneity, and decreases with order m. On the other hand, a tesseral heat flow pattern (Y_2^1) has insignificant effects on the field intensity. Olson et al. (2010) demonstrated that the reversal frequency tends to increase with increasing heterogeneity, and does not have a simple relationship with the dipole moment.

The onset of the crystallization of the inner core has a large influence on the energy source of the dynamo by excluding the light element at the inner core boundary (ICB) and releasing the latent heat of crystallization. In addition, the presence of a solid inner core itself has two separate effects on the stability of the dynamo. First, a conducting solid inner core in the middle of the liquid outer core may have a stabilizing influence on the dynamo by damping out rapid flux motions (Hollerbach and Jones, 1995). Second, the growth of the inner core changes the shape and distribution of the convection in the outer core. In turn, this would decrease the axial octupole components (Heimpel and Evans, 2013; Landeau et al., 2017).

Three major factors that have been influencing the evolution of the geomagnetic field via geodynamical events include the crystallization of the inner core, mantle processes such as subduction of crustal material to the lowermost mantle, and plume activities. Linkage between these

geodynamical events and the geomagnetic field gives us an approach to investigate the history of the Earth by using the paleomagnetic record as a key, and vice versa. High-pressure studies in this thesis provided some basic information to understand the chemical composition of the core (Chapter 2) and a possible cause of the CMB heterogeneity (Chapter 3). The paleomagnetic study in Chapter 4 provides a time-averaged geomagnetic paleointensity during a period of extraordinary stable polarity, which could provide a clue to understand the change of the heat flow pattern at the CMB, by considering the suggestions from the numerical dynamo simulations. In the following paragraphs, I review the current understanding of the inner core crystallization and lowermost mantle heterogeneity, and introduce the contributions of the present three studies in this context.

Crystallization of the inner core

Chemical compositions of planetary cores can have a large effect on their thermal evolution and dynamo activity by influencing the melting temperature, phase relations, and both thermal and electrical conductivities. In Chapter 2 I focused on hydrogen, which is supposed to have the largest effect on melting temperature (e.g. Boehler, 1996; Sakamaki et al., 2009; Nomura et al., 2014) and chemical buoyancy at the ICB among all of the candidate light elements that might be in the core. As investigations on unsaturated FeH_x are required for understanding the role of hydrogen in the evolution of the Earth's core, we obtained the high-pressure phase relations for nearly stoichiometric FeH_x, and the elastic parameters of fcc FeH_x.

One of the largest impacts of the composition of the core on exploring the thermal evolution and long-term geomagnetic trend is the thermal conductivity; this affects the estimate on age of the inner core. In the present core, the geodynamo is powered by both thermal and compositional convection, and the activity of the geodynamo controls the surface magnetic field strength. The dominant energy (~90 %) comes from the buoyancy of liquid alloy enriched in light element(s) released at the front of the inner core growth and latent heat due to crystallization (Stacy and Davis, 2008). It has been proposed that, before the beginning of the inner core formation, the dynamo motion was weaker and the surface geomagnetic field intensity was lower. Different amplitudes of intensity increase associated with the inner core birth have been proposed by calculations on the thermal evolution (e.g. Aubert et al., 2009; Labrosse, 2015; Landeau et al., 2017).

Timing of the inner core nucleation depends on the temperature history of the core, which is back-calculated from the present temperature using the CMB heat flow and thermal conductivity of the core. However, at present there is no consensus in the literature concerning the thermal conductivity of iron at the pressure and temperature conditions of Earth's core, and so estimates for the inner core nucleation age are widely scattered over Earth history. Previous studies based on various methods such as plume flux, core energetics, mantle circulation, seismic structure and mineral physics compiled by Olson (2016) exhibit present day CMB heat flow ranging from 2 to 15 TW, and an inner core age range of 0.6 to 4.3 Ga.

In high-pressure experiments, the thermal conductivity of metal can

be obtained by measurements of electrical resistivity through the Wiedemann–Franz law, which is expressed as:

$$k = \frac{1}{\rho} \times L \times T \quad (1)$$

where k is the thermal conductivity, ρ is the electrical resistivity, L is the Lorentz number ($L = 2.44*10^{-8}$ $W\Omega/K^2$), and T is the absolute temperature (Anderson, 1998; Poirier, 2000). Studies of electrical resistivity measurements suggest high conductivity due to saturation resistivity at high temperature, and thus high CMB heat flow exceeding 10 TW (Gomi et al., 2013; Gomi and Hirose, 2015; Ohta et al., 2016; Gomi et al., 2016). On the other hand, direct measurements of thermal conductivity (Konôpková et al., 2016) exhibited low conductivity, implying an inner core as old as the oldest paleointensity reported (the controversial 4.2 Ga by Tarduno et al., 2015). This discrepancy might imply the collapse of Wiedemann–Franz law at high pressures and temperatures, which should be examined experimentally.

In addition to the uncertainties of the thermal conductivity of pure iron, the composition of light elements will also affect the conductivity of the core. Incorporation of light elements and nickel decreases the conductivity of iron due to impurity effects. Gomi et al. (2013) and Gomi and Hirose (2015) measured the electrical conductivity of pure iron, iron-silicon alloy and iron-nickel alloys with silicon, carbon, oxygen and sulfur. They were able to estimate the condicutivies of these alloys using the Norbury-Linde rule, which suggests that the impurity resistivity is proportional to the square of the difference in valence between iron and the impurity element (Linde, 1932; Mott, 1936). However, their measured electrical resistivities implies only a

small impurity effect on iron-sulfur alloys, raising doubts on the Norbury-Linde rule (Suehiro et al., 2017). Ohta et al. (in prep.) measured the electrical conductivity of fcc FeH_x synthesized in the method using paraffin which is identical to that we used in Chapter 4. They found that hydrogen has only a minor effect on changing the conductivity of iron.

Recently, O'Rourke and Stevenson (2016) proposed that compositional convection predating the inner core was due to precipitation of light components such as magnesium bearing minerals, whereas Hirose et al. (2017) suggested that SiO_2 exsolution from the cooling liquid was responsible. Numerical simulations on the moon-forming giant impact suggest enormously high temperatures were present at the early stage of the Earth's history (Canup, 2008, 2012; Cuk and Stewart, 2012), which would promote large quantities of light elements to go into solution. As the core cooled, the solubility of these light elements would decrease, and precipitation should occur. These scenarios give a clue for understanding the energy source of the geodynamo before inner core formation. If compositional convection predated the inner core, the increase of the geomagnetic field strength associated with the inner core formation might not be as large as proposed.

Selected paleointensity data from a compilation of published works indicate an increase in both mean value and variation in the virtual dipole moment (VDM), which could be interpreted as an inner core age of around 1.3 Ga (Biggin et al., 2015). However, sparseness of reliable Precambrian paleointensity data are making it difficult to constrain the precise curve of the geomagnetic field strength. Paleointensity experiments on Precambrian

samples by the new single crystal method proposed in Chapter 4 is expected to enhance the information of the ancient geomagnetic field, and help our understanding of the long-term trend of the field intensity.

CMB heat flow controlled by the mantle

The amount of CMB heat flow and its spatial heterogeneity is controlled by the activity of the mantle. For instance, Takahashi et al. (2008) demonstrated that lateral heat flux variations of the present CMB inferred from shear velocity structure in the D" region could be responsible for about a 25 % increase in the mean field strength at the CMB compared to a thermally homogeneous CMB. Heterogeneity of the CMB heat flow could be caused by heterogenic compositional and/or temperature distribution. In Chapter 3, we determined the melting temperature and phase relation of the FeO-SiO_2 system, which is one of the most fundamental binary systems in the Earth's mantle. Based on our results, we argued that partial melting of subducted banded iron formations (BIFs) at the lowermost mantle could have contributed to the formation of FeO-rich portion in the D" layer, detected as the ultralow velocity zones (ULVZs). Ballmer et al. (2017) suggested that iron-enriched dense patches could remain at the lowermost mantle for several billions of years, resistant to mantle convection. If the subduction and melting of BIFs had major contribution on the CMB thermal heterogeneity, the amplitude of heterogeneity could be enhanced after the maximum deposition era of BIFs at 2.5 to 2.0 Ga. This might be detectable by accumulating paleointensity measurements in the Archean to Paleoproterozoic period.

Crystallization of the basal magma ocean is another possible scenario that might have given raise to FeO-rich patches in the D" region (Labrosse et al., 2007; Nomura et al., 2011; Ballmer et al., 2017). Studies on thermal conductivity of lower mantle minerals suggest that iron-rich (Mg, Fe)O ferropericlase is lower than that of MgO periclase, bridgmanite and post perovskite (Ohta et al., 2017), while extremely iron-rich (Mg, Fe)O magnesiowüstite (>80 atom % iron) shows enormously high thermal conductivity (Ohta et al., 2014). Therefore, the amplitude of iron enrichment is important on the CMB thermal heterogeneity pattern related to FeO concentration.

Other subducted materials such as the mid-oceanic ridge basalts (MORBs; e.g. Hirose et al., 1999; 2005), continental crust (e.g. Komabayashi et al., 2009) and depleted peridotite (e.g. Kudo et al., 2012) have been proposed for the cause of the seismic heterogeneity of the lowermost mantle. These materials could have been contributed to temperature, rather than compositional, heterogeneity in the means of effect on the dynamo. Recently, Borgeaud et al. (2017) reported evidence of two cold paleoslabs reaching the lowermost mantle that were detected via their high seismic velocity anomalies.

In Chapter 4, we studied the paleointensity of the Iritono granite, which cooled during the middle age of the Cretaceous normal superchron (CNS). The obtained VDM was well above the average value of the past 5 million years (Fig. 14 in Chapter 4), suggesting that the dipole moment anticorrelates with the reversal frequency. This indicates that the superchron

was caused by a low total CMB heat flow at the period of CNS rather than enhanced heterogeneity (Olson et al. 2010).

Three periods of superchrons are known in the Phanerozoic time. The latest superchron is the CNS which lasted from 118 to 83 Ma. The Kiaman reverse superchron (KRS) and the Moyero reversed superchron (MRS) lasted from 310 to 260 Ma (Opdyke and Channell, 1996), and 490 to 460 Ma (Gallet and Pavlov, 1996; Pavlov and Gallet, 2005; Grappone et al., 2017), respectively. Many studies have argued for a linkage between superchrons and whole-mantle convection process (such as the activity of mantle plumes) which are in turn related to surface phenomena such as flood basalt eruptions and continental drift (e.g. Courtillot and Olson, 2007; Zhang and Zhong, 2011; Biggin et al., 2012). Courtillot and Olson (2007) pointed out the association of superchrons and major flood basalts with mass extinction events, and proposed that the ~200 Myr pattern of mantle convection induces the amount and spatial variations of the CMB heat flow. Biggin et al. (2012) argued that a superchron could be triggered by a global or equatorial decrease of CMB heat flow, linked to reduced plume-head production, or true polar wander events (Gold, 1955). For further understanding of the controlling role, high quality paleointensity data of the KRS and MRS as well as the CNS, combined with realistic numerical dynamo models, are required.

§2 Effectiveness of paleointensity measurements on plagioclase

In Chapter 4, we introduced a prospective tool to investigate the time-averaged geomagnetic field strength, which is the Tsunakawa-Shaw

paleointensity approach, but on single plagioclase crystals separated from a granitic rock. Here we discuss the effectiveness of the present method in detecting the change in field strength.

We take the intensity transition associated with inner core nucleation as an example. Fig. 2 shows three different estimates of evolution of the true dipole moment (TDM) proposed by Aubert et al. (2009) and Labrosse (2015). Aubert et al. (2009) produced two models referred as "high power" and "low power" scenarios in which the inner core ages are around 750 Myr and 1800 Myr, by assuming the present day CMB heat flux as 3 and 11 TW, respectively. Estimation by Labrosse (2015) employed 13.25 TW for the present day CMB heat flux and considered the minimum scenario before the inner core. Therefore, the increase in TDM around the inner core nucleation could be taken as the maximum. The estimated inner core age by Labrosse (2015) is around 600 Myr.

We obtained a paleointensity value with ±20 % error from averaging results of nine plagioclase samples. Considering this error percentage, VDM changes larger than 40 % could be detected easily by comparing results from two different ages. Therefore, if the scenario proposed by Labrosse (2015) is the case, the timing of inner core nucleation could be clearly constrained. The "low power" scenario of Aubert et al. (2009) is characterized by decrease in the field strength in the period before the inner core and rapid recovery, which could also detected possibly by measuring samples in the proper age range. On the other hand, more accuracy might be required to detect moderate changes in the "high power" scenario. Needless to say, averaging higher

numbers of samples per studied rock unit, which is also required to average out the anisotropy effect (Usui et al., 2015), would help to increase the sensitivity for VDM changes by a factor of sqrt(N).

§3 Summary

Thermal evolution models of the deep earth inferred from high pressure petrographic constraints need to be verified by geological data. Long-term trends of the geomagnetic field obtained by paleomagnetic studies need to be integreated into an evolutionary model for the Core. These are related with each other through numerical dynamo models. It is important to combine knowledge from different research fields to explore the history of the deep Earth. From this idea, I have been working on both high-pressure and paleomagnetic experiments.

High pressure studies on iron hydride provide fundamental information for exploring the chemical composition of the core, and may contribute to a more realistic modelling of of its history over geological time. From the high pressure melting phase relations in the FeO-SiO_2 system, we deduced the possible role of subducted BIFs on the heterogeneous distribution of Fe-enriched material at the CMB, which may influence the behavior of the geodynamo. Paleointensity measurements on single crystals separated from granitic rocks that are tuned to the long-term trend of geomagnetic field variation could be of wide application for advanced insights of the history of the deep Earth. The high field strength during the CNS gives a clue to constrain the amount and heterogeneity of the CMB heat flow.

I hope that further efforts on these investigations will enable us to answer long existing questions such as the age of the inner core and the nature of the geomagnetic superchrons, and help humanity in our effort to 'reach for the core'.

Reference

Anderson, O. L., (1998). The Grüneisen parameter for iron at outer core conditions and the resulting conductive heat and power in the core. Phys. Earth. Planet. Int. 109, 179–197.

Aubert, J., Labrosse, S., Poitou, C. (2009) Modelling the palaeo-evolution of the geodynamo, Geophysical Journal International, 179, 1414-1428.

Ballmer, M. D., Lourenço, D. L., Hirose, K., Caracas, R., Nomura, R. (2017). Reconciling magma - ocean crystallization models with the present - day structure of the earth's mantle. Geochemistry, Geophysics, Geosystems. 18(7), 2785-2806.

Biggin, A. J., Piispa, E. J., Pesonen, L. J., Holme, R., Paterson, G. A., Veikkolainen, T., Tauxe, L. (2015). Palaeomagnetic field intensity variations suggest Mesoproterozoic inner-core nucleation.

Biggin, A. J., Steinberger, B., Aubert, J., Suttie, N., Holme, R., Torsvik, T. H., van der Merr, D. G., Van Hinsbergen, D. J. J. (2012). Possible links between long-term geomagnetic variations and whole-mantle convection processes. Nature Geoscience, 5(8), 526-533.

Boehler, R., (1996). Melting temperature of the Earth's mantle and core: Earth's thermal structure. Annual Review of Earth and Planetary Sciences, 24, 15–40.

Borgeaud, A. F., Kawai, K., Konishi, K., Geller, R. J. (2017). Imaging paleoslabs in the D" layer beneath Central America and the Caribbean using seismic waveform inversion. Science advances, 3(11), e1602700.

Canup, R.M. (2008). Accretion of the Earth. Philos. Trans. R. Soc. A 366, 4061-4075.

Canup, R.M. (2012). Forming a moon with an Earth-like composition via a giant impact. Science 338, 1052-1055.

Christensen, U.R., Aubert, J. (2006). Scaling properties of convection driven dynamos in rotating spherical shells and application to planetary magnetic fields. Geophys. J. Int. 166, 97–114.

Courtillot, V., Olson, P. (2007) Mantle plumes link magnetic superchrons to Phanerozoic mass depletion events. Earth and Planetary Science Letters, 260(3), 495-504.

Cuk, M., Stewart, S.T. (2012) Making the Moon from a fast-spinning Earth: a giant impact followed by resonant despinning. Science 338, 1047-1051.

Gallet, Y., Pavlov, V. (1996). Magnetostratigraphy of the Moyero river section (north-western Siberia): constraints on geomagnetic reversal frequency during the early Paleozoic. Geophys. J. Int. 125, 95–105.

Glatzmaier, G. A., Coe, R. S., Hongre, L., Roberts, P. H. (1999). The role of the Earth's mantle in controlling the frequency of geomagnetic reversals. Nature, 401(6756), 885-890.

Gomi, H., Hirose, K. (2015). Electrical resistivity and thermal conductivity of hcp Fe–Ni alloys under high pressure: Implications for thermal convection in the Earth's core. Physics of the Earth and Planetary Interiors, 247, 2-10.

Gomi, H., Hirose, K., Akai, H., Fei, Y. (2016). Electrical resistivity of substitutionally disordered hcp Fe–Si and Fe–Ni alloys: Chemically-induced resistivity saturation in the Earth's core. Earth and Planetary Science Letters, 451, 51-61.

Gomi, H., Ohta, K., Hirose, K., Labrosse, S., Caracas, R., Verstraete, M. J., Hernlund, J. W. (2013). The high conductivity of iron and thermal evolution of the Earth's core. Physics of the Earth and Planetary Interiors, 224, 88-103.

Gold, T. (1955). Instability of the Earth's axis of rotation. Nature, 175(4456),

526.

Grappone, M., T Chaffee, Y Isozaki, H Bauert, JL Kirschvink, Investigating the duration and termination of the Early Paleozoic Moyero reversed polarity Superchron: Middle Ordovician paleomagnetism from Estonia. Palaeogeography, Palaeoclimatology, Palaeoecology 485, 673-686.

Heimpel, M., Evans, M., (2013). Testing the geomagnetic dipole and reversing dynamo models over Earth's cooling history. Phys. Earth Planet. Inter., 224, 124–131.

Hirose, K., Fei, Y., Ma, Y., Mao, H., (1999). The fate of subducted basaltic crust in the Earth's lower mantle. Nature397, 53–56.

Hirose, K., Morard, G., Sinmyo, R., Umemoto, K., Hernlund, J., Helffrich, G., Labrosse, S. (2017). Crystallization of silicon dioxide and compositional evolution of the Earth's core. Nature, 543(7643), 99-102.

Hirose, K., Takafuji, N., Sata, N., Ohishi, Y., (2005). Phase transition and density of subducted MORB crust in the lower mantle. Earth Planet. Sci. Lett.237, 239–251.

Hollerbach, R., Jones, C. A. (1995). On the magnetically stabilizing role of the Earth's inner core. Physics of the Earth and Planetary Interiors, 87(3-4), 171-181.

Komabayashi, T., Maruyama, S., Rino, S. (2009). A speculation on the structure of the D ″ layer: The growth of anti-crust at the core-mantle boundary through the subduction history of the Earth. Gondwana Research, 15(3), 342-353.

Konôpková, Z., McWilliams, R. S., Gómez-Pérez, N., Goncharov, A. F. (2016). Direct measurement of thermal conductivity in solid iron at planetary core conditions. Nature, 534(7605), 99-101.

Kudo, Y., Hirose, K., Murakami, M., Asahara, Y., Ozawa, H., Ohishi, Y., Hirao, N. (2012). Sound velocity measurements of $CaSiO_3$ perovskite to 133GPa and implications for lowermost mantle seismic anomalies.

Earth and Planetary Science Letters, 349, 1-7.

Kutzner, C., Christensen, U. (2002). From stable dipolar to reversing numerical dynamos. Phys. Earth Planet. Inter. 121, 29–45.

Labrosse, S. (2015). Thermal evolution of the core with a high 302 thermal conductivity, Phys. Earth Planet. Inter., 247, 36–55.

Labrosse, S., J. W. Hernlund, N. Coltice (2007). A crystallizing dense magma ocean at the base of the Earth's mantle, Nature, 450, 866–869.

Landeau, M., Aubert, J., Olson, P. (2017). The signature of inner-core nucleation on the geodynamo. Earth and Planetary Science Letters, 465, 193-204.

Larson, R. L., Olson, P. (1991). Mantle plumes control magnetic reversal frequency. Earth and Planetary Science Letters, 107(3-4), 437-447.

Linde, J. O., (1932). Elektrische Eigenschaften verdünnter Mischkristallegierungen III. Widerstand von Kupfer-und Goldlegierungen. Gesetzmäßigkeiten der Widerstandserhöhungen. Ann. Physik 15, 219–248.

Mott, N.F., (1936). The electrical resistance of dilute solid solutions. Proc. Cambridge Philos. Soc. 32, 281.

Nomura, R., Hirose, K., Uesugi, K., Ohishi, Y., Tsuchiyama, A., Miyake, A., Ueno, Y., (2014). Low Core-Mantle Boundary Temperature Inferred from the Solidus of Pyrolite. Science 343, 522-525.

Nomura, R., H. Ozawa, S. Tateno, K. Hirose, J. Hernlund, S. Muto, H. Ishii, N. Hiraoka (2011), Spin crossover and iron-rich silicate melt in the Earth's deep mantle, Nature, 473(7346), 199–202.

Ohta, K., Fujino, K., Kuwayama, Y., Kondo, T., Shimizu, K., Ohishi, Y. (2014). Highly conductive iron‐rich (Mg, Fe) O magnesiowüstite and its

stability in the Earth's lower mantle. Journal of Geophysical Research: Solid Earth, 119(6), 4656-4665.

Ohta, K., Kuwayama, Y., Hirose, K., Shimizu, K., Ohishi, Y. (2016). Experimental determination of the electrical resistivity of iron at Earth's core conditions. Nature, 534(7605), 95-98.

Ohta, K., Suehiro, S., Hirose, K., Ohishi, Y. (in prep.). Electrical resistivity of *fcc* phase iron hydrides at high pressures and temperatures.

Ohta, K., Yagi, T., Hirose, K., Ohishi, Y. (2017). Thermal conductivity of ferropericlase in the Earth's lower mantle. Earth and Planetary Science Letters, 465, 29-37.

Olson, P. (2016), Mantle control of the geodynamo: Consequences of topdown regulation, Geochem. Geophys. Geosyst., 17, 1935–1956.

Olson, P., Christensen, U.R. (2006). Dipole moment scaling for convection-driven planetary dynamos. Earth Planet. Sci. Lett. 250, 561–571.

Olson, P. L., Coe, R. S., Driscoll, P. E., Glatzmaier, G. A., Roberts, P. H. (2010). Geodynamo reversal frequency and heterogeneous core–mantle boundary heat flow. Physics of the Earth and Planetary Interiors, 180(1-2), 66-79.

Opdyke, N., Channell, J.E.T. (1996). Magnetic stratigraphy. Int. Geophys. Ser., vol. 64. Academic Press, San Diego. 346 pp.

O'Rourke, J. G., Stevenson, D. J. (2016). Powering Earth's dynamo with magnesium precipitation from the core. Nature, 529(7586), 387-389.

Pavlov, V., Gallet, Y. (2005). A third superchron during the Early Paleozoic. Episodes 28, 1–7.

Poirier, J.P., (2000). Introduction to the Physics of the Earth's Interior, 2nd ed. Cambridge University Press.

Sakamaki, K., Takahashi, E., Nakajima, Y., Nishihara, Y., Funakoshi, K., Suzuki, T., Fukai, Y. (2009). Melting phase relation of FeH x up to 20GPa: Implication for the temperature of the Earth's core. Physics of the Earth and Planetary Interiors, 174(1), 192-201.

Stacey, F. D., Davis, P. M. (2008). Physics of the Earth, Fourth Edition. New York: Wiley.

Suehiro, S., Ohta, K., Hirose, K., Morard, G., Ohishi, Y. (2017). The influence of sulfur on the electrical resistivity of hcp iron: Implications for the core conductivity of Mars and Earth. Geophysical Research Letters, 44(16), 8254-8259.

Takahashi, F., Tsunakawa, H., Matsushima, M., Mochizuki, N., Honkura, Y. (2008). Effects of thermally heterogeneous structure in the lowermost mantle on the geomagnetic field strength. Earth and Planetary Science Letters, 272(3), 738-746.

Tarduno, J. A., Cottrell, R. D., Davis, W. J., Nimmo, F., Bono, R. K. (2015) A Hadean to Paleoarchean geodynamo recorded by single zircon crystals. Science, 349(6247), 521-524.

Usui, Y., Shibuya, T., Sawaki, Y., Komiya, T. (2015). Rock magnetism of tiny exsolved magnetite in plagioclase from a Paleoarchean granitoid in the Pilbara craton. Geochemistry, Geophysics, Geosystems, 16(1), 112-125.

Zhang, N., Zhong, S. (2011). Heat fluxes at the Earth's surface and core–mantle boundary since Pangea formation and their implications for the geomagnetic superchrons. Earth and Planetary Science Letters, 306(3), 205-216.

Figures

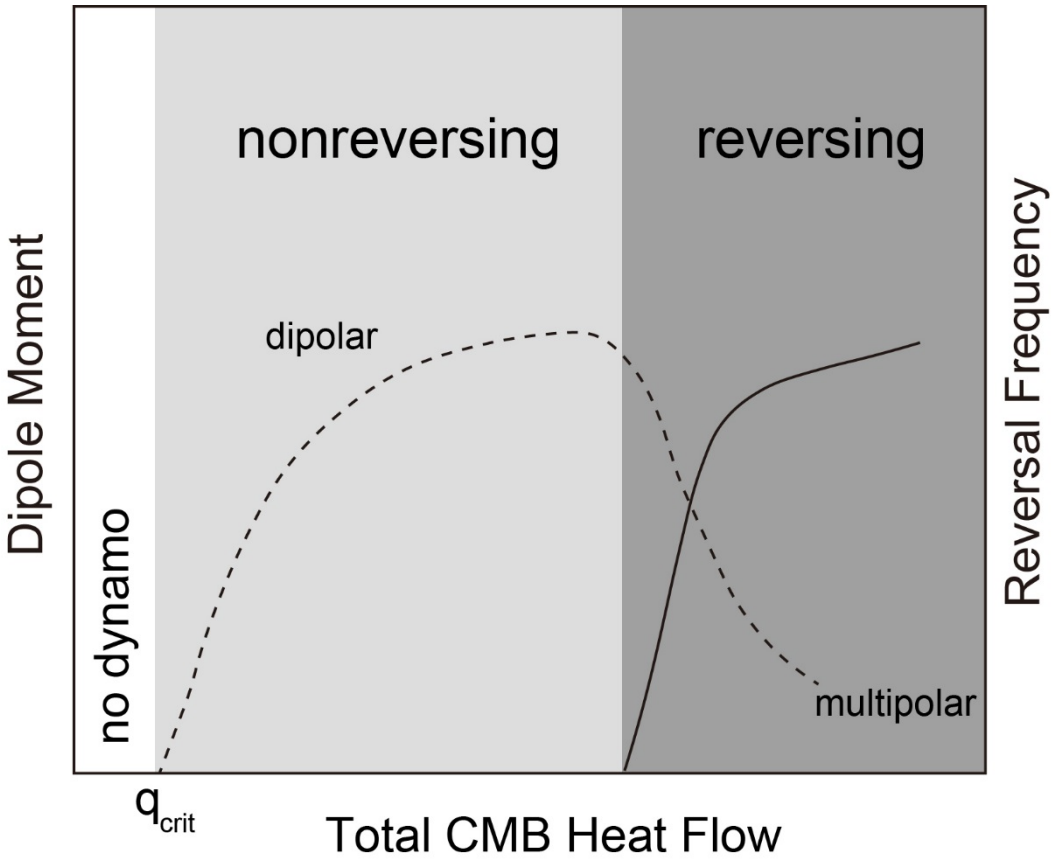

Fig. 1 Schematic diagram of the dependence of reversal frequency and dipole moment on the total CMB heat flow. Solid and dashed lines indicate reversal frequency and dipole moment, respectively. Modified after Courtillot and Olson, (2007).

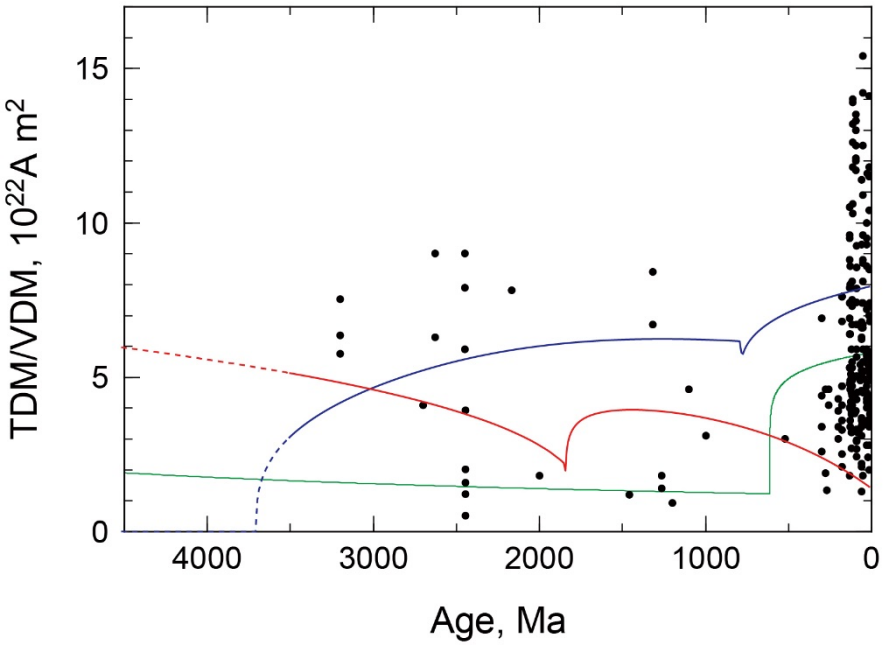

Fig. 2 Modelled true dipole moment (TDM) and selected VDM data from the PINT database. Modified after Aubert et al. (2009) and Labrosse (2015). Blue and red curves: high and low power scenario from Aubert et al. (2009). Green curve from Labrosse (2015). Black dots are for selected VDM data from the PINT database.

Appendix

NAL phase in K-rich portions of the lower mantle

Chie Kato, Kei Hirose, Tetsuya Komabayashi, Haruka Ozawa, and Yasuo Ohishi (2013) NAL phase in K-rich portions of the lower mantle, Geophysical Research Letters, 40, 5085–5088, doi:10.1002/grl.50966.

Abstract

The stability of the K-rich new aluminous (NAL) phase was examined on the join $Na_{1.00}Mg_{2.00}Al_{4.80}Si_{1.15}O_{12}$-$K_{1.00}Mg_{2.00}Al_{4.80}Si_{1.15}O_{12}$ (Na100-K100) up to 144 GPa by X-ray diffraction in a laser-heated diamond anvil cell. Single-phase K100 and Na50K50 NAL were formed up to the lower mantle conditions, and the NAL phase coexisted with the calcium ferrite–type (CF) phase at 120 GPa and 2300 K for the Na75K25 bulk composition. This is a striking contrast to the K-free (Na100) NAL that becomes unstable above 27 GPa at 1850 K, which suggests that potassium stabilizes NAL at significantly higher pressures. K-rich NAL may host potassium in the lower mantle that contains K_2O more than 0.09 wt %. In addition, the NAL phase likely formed owing to partial melting in the ultralow-velocity zone or because of a basal magma ocean. Future seismological observations may clarify whether NAL is a radiogenic heat source above the core-mantle boundary.

§1. Introduction

Potassium is an important heat-producing element, but its host phases under deep lower mantle conditions remain poorly known (Wang and Takahashi, 2000; Miyajima et al., 2001; Lee et al., 2009). The K_2O content of pyrolytic mantle is considered very low (~0.03 wt %) (McDonough and Sun, 1995), but the occurrence of K-rich magmatism suggests that the mantle is locally enriched in potassium (McCulloch et al., 1983) and includes a discrete phase as a host of potassium in such K-rich portions. Previous experimental studies demonstrated that K phase III appears in K-doped pyrolitic lower mantle material (0.64 wt % K_2O) at 25.5 GPa, coexisting with $MgSiO_3$-rich perovskite, ferropericlase, and $CaSiO_3$-rich perovskite (Wang and Takahashi, 2000). Because the solubility of potassium in typical lower mantle phases is quite limited, Wang and Takahashi (2000) argued that the K phase III is present even in normal lower mantle.

K phase III should be identical to the NAL phase (Miyajima et al., 1999; Gasparik et al., 2000; Miura et al., 2000). NAL is known to form in subducted basaltic crust under uppermost lower mantle conditions (Miyajima et al., 2001; Hirose and Fei, 2002; Ricolleau et al., 2010). More recent experiments by Imada et al. (2011) have shown that the NAL phase only forms below 45 GPa and undergoes transformation into CF at higher pressures on the join $NaAlSiO_4$-$MgAl_2O_4$ (Ono et al., 2009). This is consistent with the disappearance of NAL above ~50 GPa in deeply subducted oceanic crust with mid-oceanic ridge basalt (MORB) composition (Perrillat et al., 2006; Ricolleau et al., 2008). Nevertheless, potassium prefers NAL more than CF as

demonstrated by high-pressure experiments (Miyajima et al., 2001) and by the study of inclusions in superdeep diamonds (Walter et al., 2011), indicating that potassium stabilizes NAL relative to CF.

The general formula for NAL is $(M3)(M2)_2(M1)_6O_{12}$, where M1, M2, and M3 represent small-, middle-, and largesized cations, respectively (Miura et al., 2000; Gasparik et al., 2000). The structure of NAL has hexagonal symmetry and consists of a double-chain framework of $M1O_6$ octahedra that are connected to each other by sharing the edges. Two differently sized tunnel-like spaces along the c axis surrounded by three and six double chains of $M1O_6$ provide the sites for the middle-sized (M2) and relatively large-sized (M3) cations, respectively. Because of the large cation site, NAL can incorporate potassium. Kojitani et al. (2011) reported that NAL with $K_{1.00}Mg_{2.00}Al_{4.80}Si_{1.15}O_{12}$ composition contains the maximum amount of potassium (including cation vacancy in the M1 site) and that the M3 site is only occupied by potassium. In this study, we determined the phase relations on the join $Na_{1.00}Mg_{2.00}Al_{4.80}Si_{1.15}O_{12}$-$K_{1.00}Mg_{2.00}Al_{4.80}Si_{1.15}O_{12}$ at 33–144 GPa and 1800–2700 K by combining laser-heated diamond anvil cell techniques and synchrotron X-ray diffraction (XRD). Pressure-volume data of $K_{1.00}Mg_{2.00}Al_{4.80}Si_{1.15}O_{12}$ NAL were also obtained up to 127 GPa and room temperature. The results show that K-rich NAL has a very wide stability *P-T* field that covers the entire lower mantle.

§2. Experimental Procedure

We prepared four starting materials from gels with chemical

compositions of $Na_{0.75}K_{0.25}Mg_{2.00}Al_{4.80}Si_{1.15}O_{12}$ (Na75K25), $Na_{0.50}K_{0.50}Mg_{2.00}Al_{4.80}Si_{1.15}O_{12}$ (Na50K50), $Na_{0.25}K_{0.75}Mg_{2.00}Al_{4.80}Si_{1.15}O_{12}$ (Na25K75), and $K_{1.00}Mg_{2.00}$ $Al_{4.80}Si_{1.15}O_{12}$ (K100). The composition of the K end-member is taken from Kojitani et al. (2011). The gel was dehydrated by heating to 1273 K for 15 min, and the compositions were confirmed by electron microprobe analysis. The powder sample was pressed into a disc and coated with Au in runs #1–4 and #6–8. In runs #5 and #9–12, the sample was mixed with Au powder at a mass ratio of 10:1. Au was used as a laser absorber and an internal pressure standard. The sample was loaded into the hole of the rhenium gasket together with a pressure medium of Ar, KCl, or a pure starting material unmixed with gold (see Table S1 in the supporting information). The samples were compressed by diamond anvils with a culet size of 300 μm for pressures less than 70 GPa and a culet size of 120–150 μm for higher pressures.

The samples were heated to 1800–2700 K by a multimode yttrium/aluminum/garnet laser or a couple of single-mode Yb fiber lasers at BL10XU, SPring-8. The beam-shaping optics that converts a Gaussian beam to one with a flatter energy distribution was used to reduce the radial temperature gradient. Temperature was measured from both sides by fitting the thermal radiation spectrum to the Planck radiation function using the spectroscopic method. The heating duration was 5–135 min for each run (Table S1). Temperature variations in the 15 μm area from which XRD data were collected were within ±10 % (e.g., Ozawa et al., 2010).

The angle-dispersive spectra were collected on an imaging plate

(Rigaku R-AXIS IV) and a charge-coupled device (Bruker APEX). The wavelength of the monochromatic incident X-ray beam was 0.412–0.415 Å. Sample pressure was calculated from the volume of Au on the basis of the thermal equation of state of Fei et al. (2007). The pressure uncertainty is ±1.4–3.2 GPa and is mainly attributed to the temperature uncertainties.

§3. Results

We conducted 12 separate runs and obtained 14 data sets to examine the phase relations on the join $Na_{1.00}Mg_{2.00}Al_{4.80}Si_{1.15}O_{12}$-$K_{1.00}Mg_{2.00}Al_{4.80}Si_{1.15}O_{12}$ (Table S1). While sharp diffraction peaks appeared in less than 5 min at the low-pressure range (Figure 1), crystallization was found to be rather sluggish at greater than 120 GPa. The peaks were weak even after heating to 2700 K at 141 GPa (Figure 2). The XRD patterns of NAL and CF phases are similar to each other, but their characteristic peaks, including those at 10–11° of 2-theta angle, were used for phase identification. In addition, the misfit of peak assignment was much larger when assuming the CF phase instead of the NAL phase in all experiments.

The experiments on the K end-member (K100) demonstrated that NAL was the single phase from 39 GPa and 1900 K to 141 GPa and 2700 K (Figure 3). Earlier multianvil experiments synthesized K100 NAL at 20–25 GPa (Kojitani et al., 2011). These results indicate that K100 NAL is stable in lower mantle *P-T* conditions, although it might melt at the high temperatures of the core-mantle boundary (CMB) region. This strongly contrasts with the fact that K-free (Na100) NAL is stable only below 27 GPa at 1850 K (Imada et al.,

2011).

Similarly, we observed only NAL in both Na25K75 and Na50K50 compositions at the entire *P-T* range explored in this study. Na50K50 NAL was formed at 144 GPa, with the pressure exceeding that of the CMB. On the other hand, both NAL and CF coexisted at 120 GPa and 2300 K for the Na75K25 bulk composition (see Figure S1 in the supporting information).

In addition, we have obtained pressure-volume (P-V) data for the K end-member (K100) NAL at 300 K between 27 and 127 GPa (Table S2). The volume data were measured right after the synthesis of single-phase NAL in runs #1–5. The lattice constants and the unit-cell volumes were calculated from 14 to 34 diffraction peaks.

§4. Stability and Incompressibility of K-rich NAL

The phase relations on the join $Na_{1.00}Mg_{2.00}Al_{4.80}Si_{1.15}O_{12}$ - $K_{1.00}Mg_{2.00}Al_{4.80}Si_{1.15}O_{12}$ (Na100-K100) are drawn in Figure 3 considering the earlier experimental results on the join $NaAlSiO_4$-$MgAl_2O_4$ (Imada et al., 2011). Imada et al. (2011) reported that Na100 NAL is stable up to 27 GPa, NAL and CF coexist between 27 and 44 GPa, and Na100 and CF form above 44 GPa at 1850 K. In order to draw the composition-pressure phase diagram at 2400 K (Figure 3), the experimental temperatures were corrected by adjusting the pressure on the basis of the P-T slope (+0.008 GPa/K) of the NALout reaction in MORB (Perrillat et al., 2006).

The phase diagram in Figure 3 indicates that NAL forms a continuous solid solution on the join $Na_{1.00}Mg_{2.00}Al_{4.80}Si_{1.15}O_{12}$-$K_{1.00}Mg_{2.00}Al_{4.80}Si_{1.15}O_{12}$

below 32 GPa. More importantly, potassium drastically expands the stability field of NAL. This suggests that the K+ ion has a strong affinity for the M3 site in the NAL structure not only at 25 GPa (Kojitani et al., 2011) but also at deep lower mantle pressures.

We fitted the third-order Birch-Murnaghan equation of state to the P-V data of K100 NAL, i.e.,

$$\mathrm{P} = \frac{3}{2}K_0\left[\left(\frac{V}{V_0}\right)^{-\frac{7}{3}} - \left(\frac{V}{V_0}\right)^{-\frac{5}{3}}\right]\cdot\left\{1 + \frac{3}{4}(K' - 4)\left[\left(\frac{V}{V_0}\right)^{-\frac{2}{3}} - 1\right]\right\} \quad (1)$$

where V_0, K_0, and K' are unit-cell volume, isothermal bulk modulus, and its pressure derivative, respectively, at ambient conditions. In the fitting procedure, V_0 was fixed at 186.37(1) Å^3, as reported by Kojitani et al. (2011). The fitting yielded K_0 = 207(2) GPa and K' = 4.1(0). The results are shown in Figure S2 and Table S3 in the supporting information and are compared with the results of previous studies on different chemical compositions. We did not observe anomalous compression behavior over the pressure range studied, implying that the 3s-4d electronic transition of potassium did not take place (Bukowinski, 1976).

Imada et al. (2012), on the basis of compression experiments, reported that $K0$ = 199(6) GPa and K' = 5.0(6) for $Na_{1.2}Mg_{1.8}Al_{4.8}Si_{1.2}O_{12}$ NAL, which is similar in composition to Na100. K' was, however, not well constrained in Imada et al. (2012) because the experimental pressure range was limited to 31 GPa. We therefore fitted their P-V data with K' fixed at 4.1, same as that obtained for K100 NAL. The results show $K0$ = 207(5) GPa for

$Na_{1.2}Mg_{1.8}Al_{4.8}Si_{1.2}O_{12}$ NAL, which is identical to that of the K end-member. Note that the refitted parameters reproduce the experimental data of Imada et al. (2012) as well as their original parameters. Both Imada et al. (2012) and the present study use the Au pressure scale proposed by Fei et al. (2007). Hence, the similar *K0* values imply that the bulk modulus of NAL is not affected by the exchange between Na and K. It may be dominantly controlled by the $(Al,Si)O_6$ double chains that make up the framework of the crystal structure.

§5. K-rich NAL in the Lower Mantle

These results indicate that K-rich NAL has a wide stability field, which covers the entire *P-T* conditions of the lower mantle when the molar ratio K:(Na + K) is greater than 0.35 on the join $Na_{1.00}Mg_{2.00}Al_{4.80}Si_{1.15}O_{12}$-$K_{1.00}Mg_{2.00}Al_{4.80}Si_{1.15}O_{12}$ (Figure 3). The multianvil experiments of Wang and Takahashi (2000) demonstrated that the NAL phase formed at 25.5 GPa in K-rich (0.64 wt % K_2O) pyrolitic mantle material with a molar ratio K:(Na + K) of ~0.85 (reported as K phase III). K-rich NAL in such natural multicomponent systems has a complex chemical formula, but the main compositional difference with the present study is the high Mg and Si at the expense of Al (see Figure S3 in the supporting information). The recent first-principles calculations by Mookherjee et al. (2012) have shown that higher Mg content stabilizes NAL relative to CF, supporting that the NAL phase can be present in the deep lower mantle.

It is known that $CaSiO_3$ perovskite incorporates minor amounts of

potassium. Previous experiments by Hirose et al. (2005) reported 0.4 wt % K_2O in $CaSiO_3$ perovskite at 60 GPa, whereas Kesson et al. (1998) found 1.6–1.8 wt % K_2O at 70–135 GPa. Considering that the lower mantle may include ~5% $CaSiO_3$ perovskite (e.g., Murakami et al., 2005), K-rich NAL may appear as a discrete phase when the K_2O content is greater than 0.09 (=1.8 × 0.05) wt %. Note that typical mantle is considered to contain ~0.03 wt % K_2O (McDonough and Sun, 1995).

On the other hand, NAL transforms to CF in the middle part of the lower mantle, when the K:(Na +K) value is low (Figure 3). The NAL phase in subducted MORB crust under uppermost lower mantle conditions has a molar ratio K:(Na +K) of 0.16–0.17 (Hirose and Fei, 2002). Such low K:(Na +K) ratio accounts for the disappearance of NAL above ~50 GPa in MORB (Perrillat et al., 2006; Ricolleau et al., 2010). In addition, $KAlSi_3O_8$ hollandite II (Sueda et al., 2004) can host potassium in subducted continental crust in the uppermost lower mantle (Ishii et al., 2012) and is known to be stable at least to 128 GPa (Hirao et al., 2008).

§6. Summary and Conclusion

Our experiments demonstrate that potassium dramatically stabilizes NAL relative to CF. K-rich NAL appears in the shallow-to-deep lower mantle having a K_2O content higher than 0.09 wt%. The melting phase relations in a K-rich pyrolite composition shows that K-rich NAL (K Phase III) is the last phase to crystallize during cooling and can host potassium at 25.5 GPa (Wang and Takahashi, 2000). If this is also the case at higher pressures, K-rich NAL

may crystallize from partial melts in the ultralow-velocity zone. In addition, a large amount of K-rich NALmay have formed in the final solidification stages of a basal magma ocean (Labrosse et al., 2007; Nomura et al., 2011). Future studies on the high-temperature elastic property of NAL will elucidate the presence of NAL as a radiogenic heat source above the CMB (Kawai and Tsuchiya, 2012; Dai et al., 2013).

References

Bukowinski, M. S. T. (1976), The effect of pressure on the physics and chemistry of potassium, Geophys. Res. Lett., 3, 491–494.

Dai, L., Y. Kudo, K. Hirose, M. Murakami, Y. Asahara, H. Ozawa, Y. Ohishi, and N. Hirao (2013), Sound velocities of $Na_{0.4}Mg_{0.6}Al_{1.6}Si_{0.4}O_4$ NAL and CF phases to 73 GPa determined by Brillouin scattering method, *Phys. Chem. Miner.*, *40*, 195-201.

Fei, Y., A. Ricolleau, M. Frank, K. Mibe, G. Shen, and V. Prakapenka (2007), Toward an internally consist pressure scale, *Proc. Natl. Acad. Sci. U. S. A.*, *104*, 9182-9186.

Gasparik, T., A. Tripathi, and J. B. Parise (2000), Structure of a new Al-rich phase, $(K,Na)_{0.9}(Mg,Fe)_2(Mg,Fe,Al,Si)_6O_{12}$, synthesized at 24 GPa, *Am. Mineral.*, *85*, 613-618.

Hirao, N., E. Ohtani, T. Kondo, T. Sakai, and T. Kikegawa (2008), Hollandite II phase in $KAlSi_3O_8$ as a potential host mineral of potassium in the Earth's lower mantle, *Phys. Earth Planet. Inter.*, *166*, 97-104.

Hirose, K., and Y. Fei (2002), Subsolidus and melting phase relations of basaltic composition in the uppermost lower mantle, *Geochim. Cosmochim. Acta*, *66*, 2099-2108.

Hirose, K., N. Takafuji, N. Sata, and Y. Ohishi (2005), Phase transition and density of subducted MORB crust in the lower mantle, *Earth Planet. Sci. Lett.*, *237*, 239-251.

Imada, S., K. Hirose, and Y. Ohishi (2011), Stabilities of NAL and Ca-ferrite-type phases on the join $NaAlSiO_4$-$MgAl_2O_4$ at high pressure, *Phys. Chem. Miner.*, *38*, 557-560.

Imada, S., K. Hirose, T. Komabayashi, T. Suzuki, and Y. Ohishi (2012), Compression of $Na_{0.4}Mg_{0.6}Al_{1.6}Si_{0.4}O_4$ NAL and Ca-ferrite-type phases,

Phys. Chem. Miner., *39*, 525-530.

Ishii, T., H. Kojitani, and M. Akaogi (2012), High-pressure phase transitions and subduction behavior of continental crust at pressure-temperature conditions up to the upperpart of the lower mantle, *Earth Planet. Sci. Lett.*, *357-358*, 31-41.

Kawai, K., and T. Tsuchiya (2012), Phase stability and elastic properties of the NAL and CF phases in the $NaMg_2Al_5SiO_{12}$ system from first principles, *Am. Mineral.*, *97*, 305-314.

Kesson, S. E., J. D. Fitz Gerald, and J. M. Shelley (1998), Mineralogy and dynamics of a pyrolite lower mantle, *Nature*, *393*, 252-255.

Kojitani, H., T. Iwabuchi, M. Kobayashi, H. Miura, and M. Akaogi (2011), Structure refinement of high-pressure hexagonal aluminous phases $K_{1.00}Mg_{2.00}Al_{4.80}Si_{1.15}O_{12}$ and $Na_{1.04}Mg_{1.88}Al_{4.64}Si_{1.32}O_{12}$, *Am. Mineral.*, *96*, 1248-1253.

Labrosse, S., J. W. Hernlund, and N. Coltice (2007), A crystallizing dense magma ocean at the base of the Earth's mantle, *Nature*, *450*, 866-869.

Lee K. K. M., G. Steinle-Neumann, and S. Akber-Knutson (2009), Ab initio predictions of potassium partitioning between Fe and Al-bearing $MgSiO_3$ perovskite and post-perovskite, *Phys. Earth Planet. Inter.*, *174*, 247-253.

McCulloch, M. T., A. L. Jaques, D. R. Nelson, and J. D. Lewis (1983), Nd and Sr isotopes in kimberlites and lamproites from Western Australia: an enriched mantle origin, Nature, 302, 400–403.

McDonough, W. F., and S. S. Sun (1995), The composition of the Earth, *Chem. Geol.*, *120*, 223-253.

Miura, H., Y. Hamada, T. Suzuki, M. Akaogi, N. Miyajima, and K. Fujino (2000), Crystal structure of $CaMg_2Al_6O_{12}$, a new Al-rich high pressure

form, *Am. Mineral.*, *85*, 1799-1803.

Miyajima, N., K. Fujino, N. Funamori, T. Kondo, and T, Yagi (1999), Garnet-perovskite transformation under conditions of the Earth's lower mantle: an analytical transmission electron microscopy study, *Phys. Earth Planet. Inter.*, *116*, 117-131.

Miyajima, N., T. Yagi, K. Hirose, T. Kondo, K. Fujino, and H. Miura (2001), Potential host phase of aluminum and potassium in the Earth's lower mantle, *Am. Mineral.*, *86*, 740-746.

Mookherjee, M., B. B. Karki, L. Stixrude, C. Lithgow-Bertelloni (2012), Energetics, equation of state, and elasticity of NAL phase: Potential host for alkali and aluminum in the lower mantle, Geophys. Res. Lett., 39, L19306, doi:10.1029/2012GL053682.

Murakami, M., K. Hirose, N. Sata, and Y. Ohishi (2005), Post-perovskite phase transition and mineral chemistry in the pyrolitic lowermost mantle, *Geophys. Res. Lett.*, *32*, L03304, doi: 10.1029/2004GL021956.

Nomura, R., H. Ozawa, S. Tateno, K. Hirose, J. Hernlund, S. Muto, H. Ishii, and N. Hiraoka (2011), Spin crossover and iron-rich silicate melt in the Earth's deep mantle, *Nature*, *473*, 199-202.

Oguri, K., N. Funamori, T. Uchida, N. Miyajima, T. Yagi, and K. Fujino (2000), Post-garnet transition in a natural pyrope: a multi-anvil study based on in situ X-ray diffraction and transmission electron microscopy, *Phys. Earth Planet. Inter.*, *122*, 175-186.

Ono, A., M. Akaogi, H. Kojitani, K. Yamashita, and M. Kobayashi (2009), High-pressure phase relations and thermodynamic properties of hexagonal aluminous phase and calcium-ferrite phase in the systems $NaAlSiO_4$-$MgAl_2O_4$ and $CaAl_2O_4$-$MgAl_2O_4$, *Phys. Earth Planet. Inter.*, *174*, 39-49.

Ozawa, H., K. Hirose, S. Tateno, N. Sata, and Y. Ohishi (2010), Phase

transition boundary between B1 and B8 structures of FeO up to 210 GPa, *Phys. Earth Planet. Inter.*, *179*, 157-163.

Perrillat, J. P., A. Ricolleau, I. Daniel, G. Fiquet, M. Mezouar, N. Guignot, and H. Cardon (2006), Phase transformations of subducted basaltic crust in the upmost lower mantle, *Phys. Earth Planet. Inter.*, *157*, 139-149.

Ricolleau, A., G. Fiquet, A. Addad, N. Menguy, C. Vanni, J. P. Perrillat, I. Daniel, H. Cardon, and N. Guignot (2008), Analytical transmission electron microscopy study of a natural MORB sample assemblage transformed at high pressure and high temperature, *Am. Mineral.*, *93*, 144-153.

Ricolleau, A., J. P. Perrillat, G. Fiquet, I. Daniel, J. Matas, A. Addad, N. Menguy, H. Cardon, M. Mezouar, and N. Guignot (2010), Phase relations and equation of state of a natural MORB: implications for the density profile of subducted oceanic crust in the Earth's lower mantle, *J. Geophys. Res.*, *115*, B08202, doi: 10.1029/2009JB006709.

Shinmei, T., T. Sanehira, D. Yamazaki, T. Inoue, T. Irifune, K. Funakoshi, and A. Nozawa (2005), High-temperature and high-pressure equation of state for the hexagonal phase in the system $NaAlSiO_4$-$MgAl_2O_4$, *Phys. Chem. Miner.*, *32*, 594-602.

Sueda, Y., T. Irifune, N. Nishiyama, R. P. Rapp, T. Ferroir, T. Onozawa, T. Yagi, S. Merkel, N. Miyajima, and K. Funakoshi (2004), A new high-pressure form of $KAlSi_3O_8$ under lower mantle conditions, *Geophys. Res. Lett.*, *31*, L23612, doi: 10.1029/2004GL021156.

Walter, M. J., S. C. Kohn, D. Araujo, G. P. Bulanova, C. B. Smith, E. Gaillou, J. Wang, A. Steele, and S. B. Shirey (2011), Deep mantle cycling of oceanic crust: evidence from diamonds and their mineral inclusions, *Science*, *333*, 54-57.

Wang, W., and E. Takahashi (2000), Subsolidus and melting experiments of K-doped peridotite KLB-1 to 27 GPa: its geophysical and geochemical

implications, *J. Geophys. Res.*, *105*, 2855-2868, doi: 10.1029/1999JB900366.

Figures

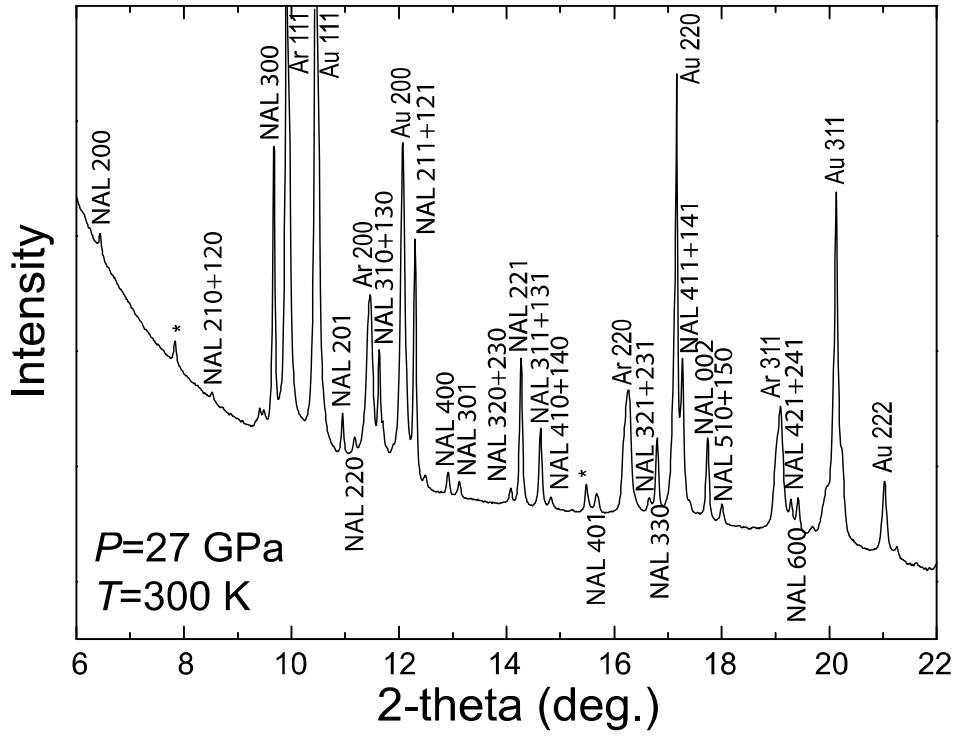

Figure 1. Typical XRD pattern of $K_{1.00}Mg_{2.00}Al_{4.80}Si_{1.15}O_{12}$ (K100) NAL collected after heating at 1900 K and 39 GPa. Asterisks indicate unknown peaks; the same unidentified peaks were previously reported for NAL by Oguri et al. (2000), Shinmei et al. (2005), and Imada et al. (2011). They possibly indicate the distortion of the crystal structure.

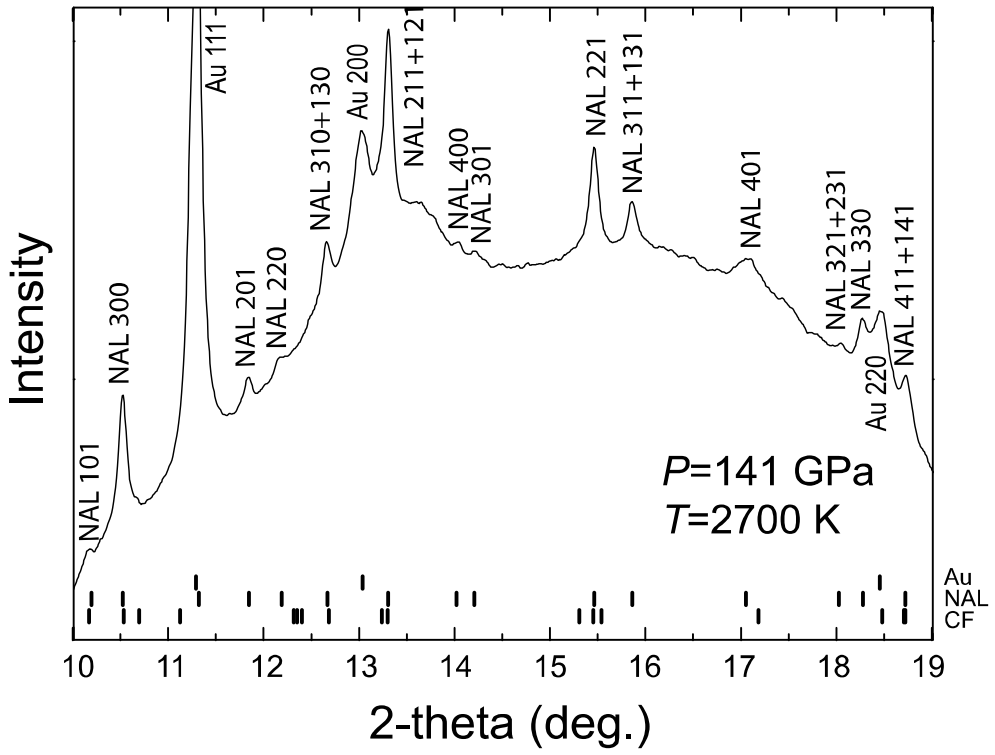

Figure 2. Typical XRD pattern of K100 NAL obtained during heating at 2700 K and 141 GPa. Tick marks represent the calculated major diffraction peaks of Au, NAL, and CF.

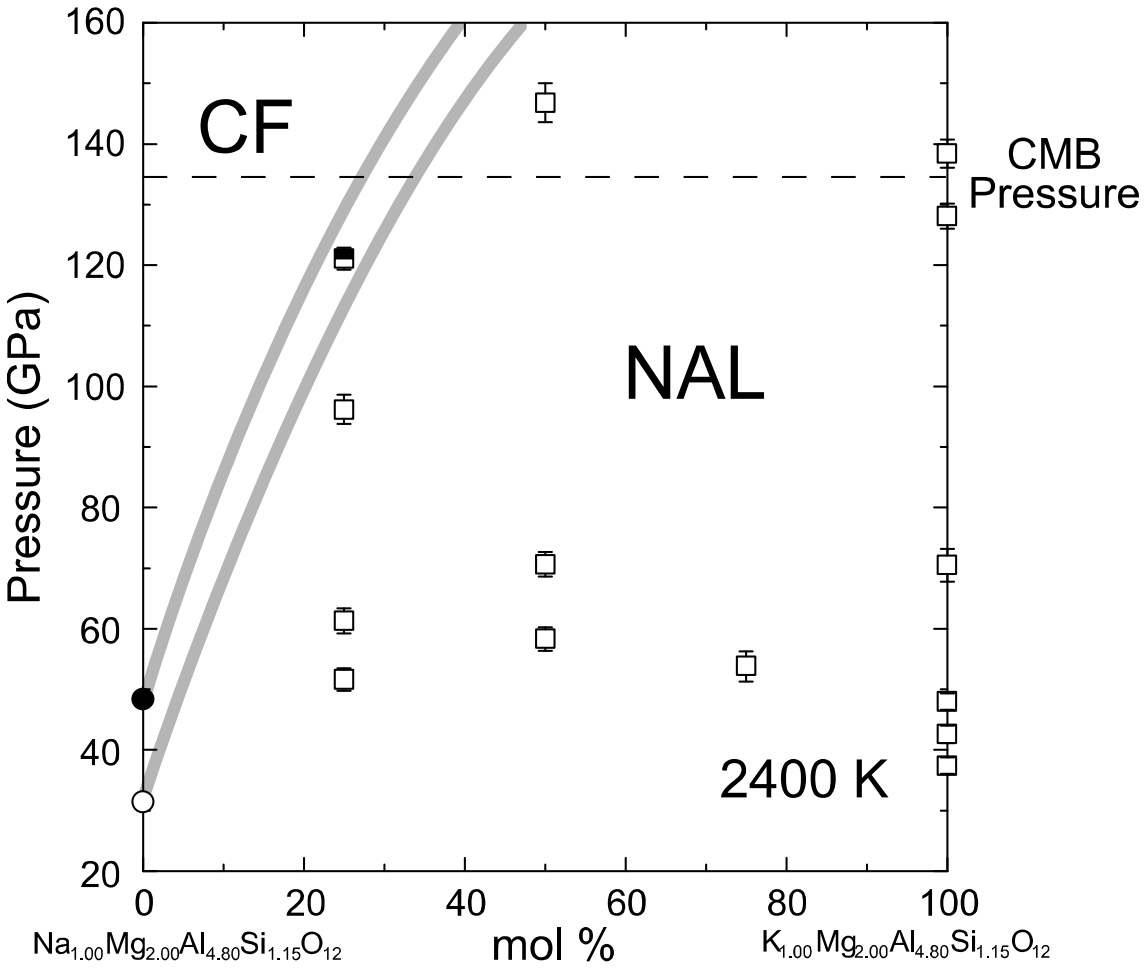

Figure 3. Phase relations on the join $Na_{1.00}Mg_{2.00}Al_{4.80}Si_{1.15}O_{12}$ - $K_{1.00}Mg_{2.00}Al_{4.80}Si_{1.15}O_{12}$ at 2400 K. Open squares indicate the formation of single-phase NAL, and the half-filled square demonstrates the coexistence of NAL and CF. Open and closed circles show the CF-in and NAL-out boundaries, respectively, for the Na end-member composition (Imada et al., 2011).

Auxiliary Materials for NAL phase in K-rich portions of the lower mantle

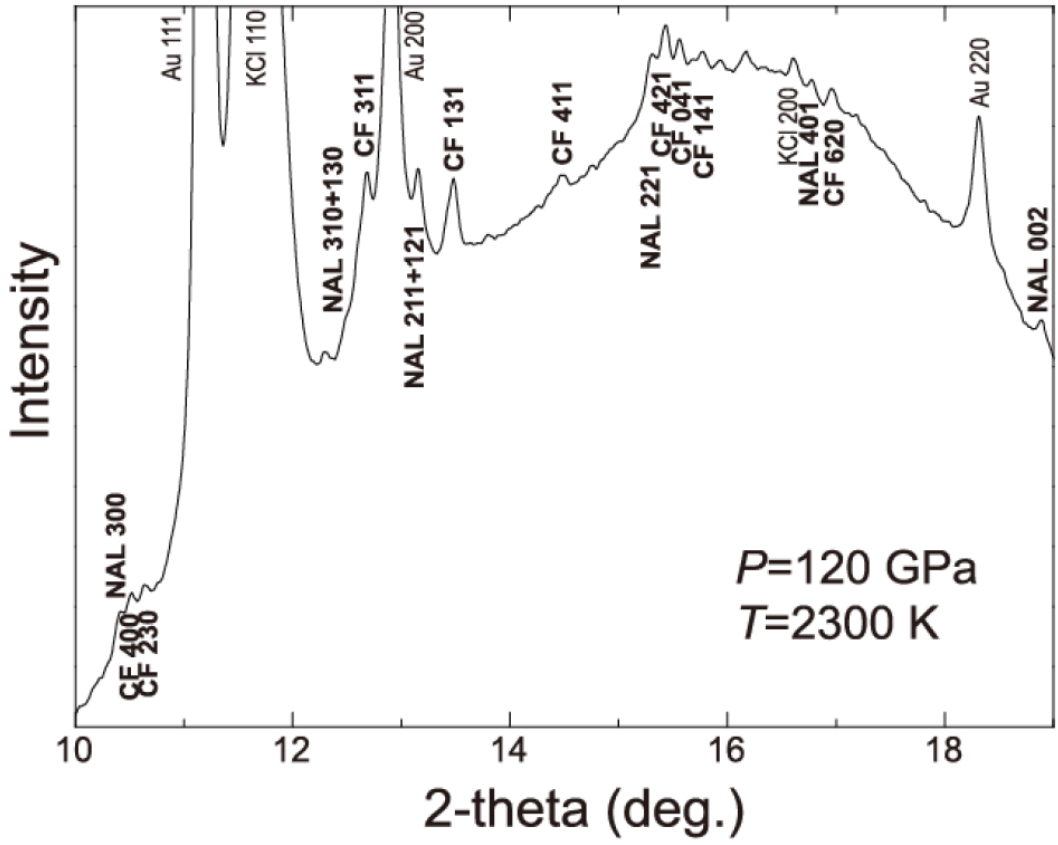

Figure S1. XRD pettern of $Na_{0.75}K_{0.25}Mg_{2.00}Al_{4.80}Si_{1.15}O_{12}$ (Na75K25) bulk composition obtained during heating at 2300 K and 120 GPa.

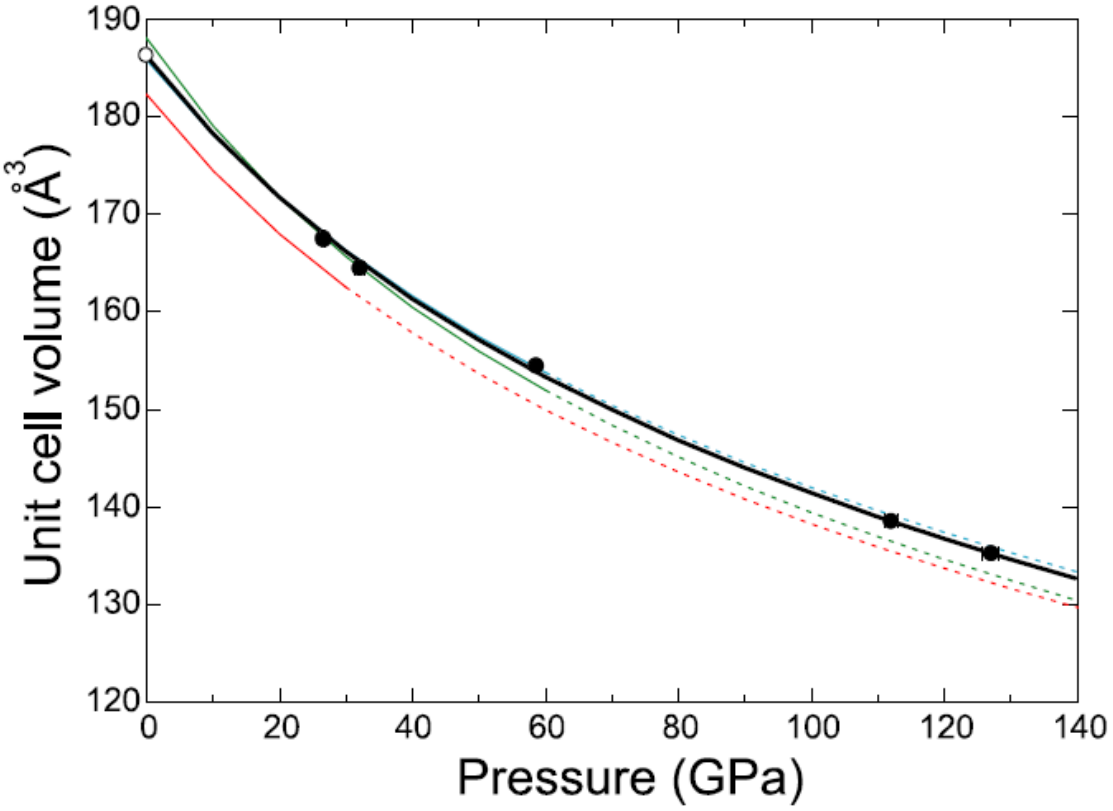

Figure S2. Compression behavior of $K_{1.00}Mg_{2.00}Al_{4.80}Si_{1.15}O_{12}$ NAL at room temperature compared with previous experimental results. Black circles and curve are obtained in this study. Open circle represents zero-pressure volume reported by Kojitani et al. (2011). Red curve, $Na_{0.4}Mg_{0.6}Al_{1.6}Si_{0.4}O_4$ NAL (Imada et al., 2012); green curve, NAL on the join $NaAlSiO_4$-$MgAl_2O_4$ (Guignot and Andrault, 2004); light blue curve, K-rich NAL from Guignot and Andrault (2004). Solid lines indicate experimental pressure range and dashed lines extrapolation.

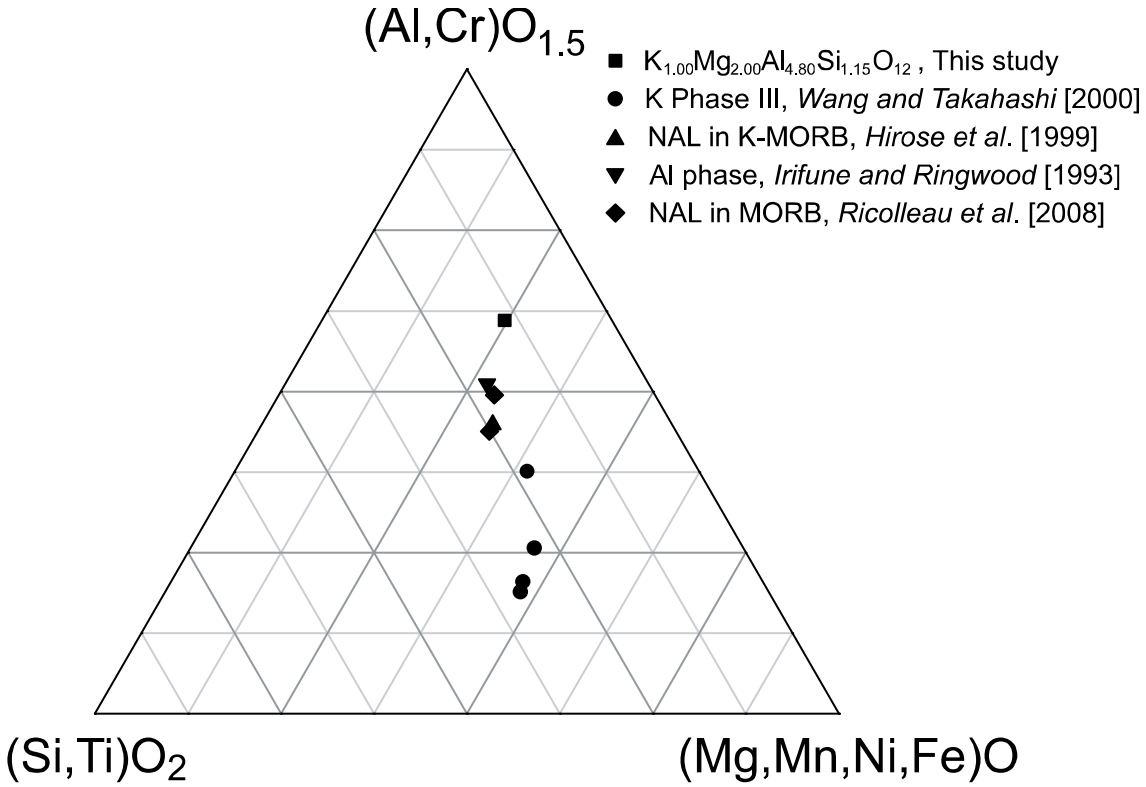

Figure S3. Chemical compositions of NAL projected onto the $(Al,Cr)O_{1.5}$ – $(Si,Ti)O_2$ – $(Mg,Mn,Ni,Fe)O$ plane from $(K, Na)_2O$. All Fe calculated as Fe^{2+}.

Table S1. Experimental conditions and run product phases

Run#	Composition	*P* (GPa)	*T* (K)	Hiating Time (min)	Phase	Pressure Medium
1	K100	39	1900	5	NAL	Ar
2	K100	33	1800	24	NAL	Ar
3	K100	43	1800	45	NAL	Ar
4	K100	69	2200	41	NAL	KCl
5_1	K100	129	2500	50	NAL	Pure sample
5_2	K100	141	2700	17	NAL	Pure sample
6_1	Na50K50	59	2500	33	NAL	KCl
6_2	Na50K50	66	1800	21	NAL	KCl
7	Na25K75	56	2700	33	NAL	KCl
8	Na75K25	52	2400	17	NAL	KCl
9	Na50K50	144	2000	95	NAL	KCl
10	Na75K25	120	2300	135	NAL+CF	KCl
11	Na75K25	63	2600	8	NAL	KCl
12	Na75K25	93	2000	16	NAL	KCl

Table S2. Lattice constant and unit-cell volumes of NAL and coexisting Au

Run	P (GPa)	a axis (A)	c axis (A)	V (A^3)	a of Au (A)
1	27	8.495(1)	2.683(6)	167.65(5)	3.925(1)
2	27	8.493(1)	2.681(7)	167.49(6)	3.925(1)
3	32	8.431(2)	2.673(2)	164.53(13)	3.903(3)
4	59	8.253(1)	2.620(1)	154.57(5)	3.817(0)
5_1	112	7.954(3)	2.530(3)	138.66(17)	3.701(2)
5_2	127	7.886(2)	2.513(1)	135.35(9)	3.676(2)

Table S3. Comparison of elastic parameters of NAL obtained in this study and previous experiments

Composition	K_0	K'_0	V_0 (Å^3)	P scale	Max P (GPa)	References
$K_{1.00}Mg_{2.00}Al_{4.80}Si_{1.15}O_{12}$	207(2)	4.1(0)	186.37(fixed)	Au (*Fei et al.*, 2007)	127.2	This study
	209(2)	4.0(fixed)				
$Na_{0.4}Mg_{0.6}Al_{1.6}Si_{0.4}O_4$	199(6)	5.0(6)	182.27(24)	Au (*Fei et al.*, 2007)	31.2	*Imada et al.* [2012]
	207(5)	4.1(fixed)				
K-rich	183(13)	5.8(8)	186.4(6)	Ar (*Guignot and*	49.8	*Guignot and*
	217(8)	4.0(fixed)	185.7(7)	*Andrault*, 2004)		*Andrault* [2004]
$NaAlSiO_4$-$MgAl_2O_4$ join	184(16)	4.0(fixed)	188(2)		59.4	

References

Guignot, N., and D. Andrault (2004), Equations of state of Na-K-Al host phases and implications for MORB density in the lower mantle, Phys. Earth Planet. Inter., 143-144, 107-128.

Hirose, K., Y. Fei, Y. Ma, and H. Mao (1999), The fate of subducted basaltic crust in the Earth's lower mantle, Nature, 397, 53-56.

Irifune, T., and A. E. Ringwood (1993), Phase transformations in subducted oceanic crust and buoyancy relationships at depths of 600-800 km in the mantle, Earth Planet. Sci. Lett., 117, 101-110.

Acknowledgements

I would like to appreciate my supervisors Prof. Joseph L. Kirschvink, Prof. Kei Hirose and Prof. Shigeru Ida. I am grateful to Prof. Yuhji Yamamoto and Prof. Hideo Tsunakawa for essential teaching and investigations in paleomagnetic studies. Discussions with Dr. Masahiko Sato, Prof. Shinji Yamamoto and Yujiro Tamura was helpful and encouraging. I thank Prof. Kenji Ohta, Dr. Shigehiko Tateno, Dr. Ryosuke Sinmyo, Dr. Haruka Tateno, Dr. Hitoshi Gomi, Dr. Ryuichi Nomura, Dr. Saori Kawaguchi, Shoh Tagawa and Dr. Yasuo Ohishi for technical help and discussions in high pressure works. Discussions with Dr. Yusuke Sawaki, Dr. Yoichi Usui, Dr. Kenichiro Tani and Dr. Masafumi Saitoh broadened by vision of research. I am also grateful to the members of Hirose and Ohta lab. Some of my studies were not completed without collaborations with Dr. Koichiro Umemoto and Dr. Maxim D. Ballmer. Seminars with Prof. Yuichiro Ueno and his lab members always provided me different research perspectives. I felt refreshed by daily conversations with members of Hirose and Ohta labs. I am supported by the Japan Society for the Promotion of Science (JSPS) Research Fellowship for Young Scientists (DC1).

Chapter 2

XRD measurements were performed at SPring-8 (proposal nos. 2014A0080, 2014B0080, 2015A0080, 2015B0080 and 2016B0080).

Chapter 3

We thank T. Imai for the preparation of Fe_2SiO_4 fayalite. Discussion with J. Hernlund was helpful. Comments from two anonymous referees helped improve the manuscript. XRD measurements were performed at SPring-8 (proposal no. 2014A0080).

Chapter 4

The microscopic photograph of plagioclase sample (Fig. 12) was taken by Y. Tamura. Some granite samples measured in §3 was provided by Prof. A. Kamei, Dr. K. Tani and Prof. S. Ishihara. Rock- and paleomagnetic measurements were performed under the cooperative research program of Center for Advanced Marine Core Research (CMCR), Kochi University (Accept nos. 16A009, 16B009, 17A028 and 17B028).

Appendix

We thank M. Mookherjee and an anonymous reviewer for their valuable suggestions. S. Tateno, E. Sugimura, and S. Imada are acknowledged for their help in synchrotron experiments and useful comments. The in situ XRD experiments were conducted at SPring-8 (proposals 2012A0087 and 2012B0087).

The Editor thanks Mainak Mookherjee and an anonymous reviewer for their assistance in evaluating this paper.